UNIVERSIDAD DE CONCEPCIÓN

Faculty of Engineering

Department of Chemical Engineering

Doctoral Thesis

BIFUNCTIONAL ACID-METAL CATALYSTS FOR PRODUCING CYMENE FROM WASTE TYRE PYROLYSIS

Tesis presentada a la Facultad de Ingeniería de la Universidad de Concepción para optar al grado de Doctor en Ciencias de la Ingeniería con mención en Ingeniería Química

Author

Jorge Eduardo Poblete Matthies

Supervisors

Supervisor: Dr. Luis E. Arteaga Pérez

Chemical Engineering Department. Universidad de Concepción

Co-Supervisor: Dr. Romel Jiménez Concepción

Chemical Engineering Department. Universidad de Concepción

Concepción, 2025

UNIVERSIDAD DE CONCEPCIÓN

Faculty of Engineering

Department of Chemical Engineering

Doctoral Thesis

BIFUNCTIONAL ACID-METAL CATALYSTS FOR PRODUCING CYMENE FROM WASTE TYRE PYROLYSIS

Tesis presentada a la Facultad de Ingeniería de la Universidad de Concepción para optar al grado de Doctor en Ciencias de la Ingeniería con mención en Ingeniería Química

Author

Jorge Eduardo Poblete Matthies

Supervisors

Dr. Luis E. Arteaga Pérez — *Universidad de Concepción*

Dr. Romel Jiménez Concepción — *Universidad de Concepción*

Examiners

Dra. Ximena García Carmona — *Universidad de Concepción*

Dr. Serguei Alejandro Martín — *Universidad del Bío-Bío*

Dra. Claudia Ulloa Tesser — *Universidad de Concepción*

Concepción, Chile 2025

Para mi *madre* Jennifer, mi *padre* Jorge y mi *hermano* Benjamín,
por su amor, comprensión y apoyo constante a lo largo de este camino.

Y para mis *perritos*, Toby y Chicoco,
por recordarme que la felicidad habita en las cosas más simples.

AGRADECIMIENTOS

Quiero agradecer a Dios por la vida y por la oportunidad de haber vivido esta experiencia.
A mi padre y mi madre, por su amor incondicional, apoyo constante y por enseñarme a perseverar incluso en los momentos más inciertos. A mi hermano Benjamín, por ser no solo un apoyo, sino también una distracción necesaria entre tanto caos científico y académico. Y a la nueva familia que gané en Concepción, por darme ese ambiente cálido y cercano que tantas veces se extraña cuando uno está lejos de casa.
Agradezco al profesor Luis Arteaga por la oportunidad de trabajar con él, por su paciencia, orientación y la formación que me ha brindado durante estos años. Admiro no solo su tremenda calidad profesional —a la cual intenté siempre estar a la altura— sino, sobre todo, su calidad humana, siempre atenta a los detalles. Espero haber incorporado parte de sus valiosos conocimientos, así como algo de su admirable eficiencia y de su estructurada forma de trabajar.
También agradezco al profesor Romel Jiménez, por el privilegio de haber iniciado mi camino en la catálisis heterogénea bajo su tutela. Cada uno de sus comentarios y observaciones, más de alguna vez, abrió un cuestionamiento existencial, pero sin duda enriqueció este proceso. Fue un placer compartir tanto en la universidad como en la cancha de fútbol. Extiendo mis agradecimientos a los miembros del Laboratorio Carbocat**,** por su disposición y apoyo de experimentos claves para este estudio. También agradecer al profesor Serguei, por su buena disposición y apoyo para hacer esos primeros experimentos de pirólisis —que siempre terminan siendo los más desafiantes—, así como por su compañía y consejos durante aquel largo viaje a China, donde más de una vez fuimos víctimas del célebre “One Dollar”.
A un nivel más cercano, agradezco a todos mis compañeros de doctorado tanto de la UdeC como de la UBB, quienes de una u otra forma aportaron en mi formación y, sobre todo, en las necesarias distracciones frente al estrés académico. Al Nanolab, con quienes, científicamente hablando, poco teníamos en común, pero a nivel personal coincidimos en muchas cosas, haciendo que este camino fuera mucho más humano y enriquecedor. Una mención especial al Dr. Elvis, mi extrovertido amigo venezolano, en quien encontré un gran apoyo no solo académico, sino también personal, lo cual valoro enormemente. También a Bastián (pronto Dr.), por tener siempre algún panorama disponible y por aportar ese toque de rareza, con sus películas en blanco y negro de idiomas improbables. Para terminar, agradezco al profesor Frederik de la Universidad de Gante, por la oportunidad de realizar mi pasantía en su grupo de investigación, y especialmente al Dr. Stef, por su orientación, paciencia y buena disposición durante los experimentos. Finalmente, a la Agencia Nacional de Investigación y Desarrollo de Chile (ANID), por el financiamiento a través de la beca de doctorado y el proyecto FONDECYT 1240054, que hicieron posible desarrollar esta tesis de manera integral.

RESUMEN

Los neumáticos fuera de uso provenientes de camiones mineros (MTWT por sus siglas en inglés) son residuos prioritarios para la Ley de Responsabilidad Extendida del Productor (Ley REP 20.920) en Chile. Su elevada tasa de generación anual (>40.000 ton), su lenta degradación y la ausencia de rutas consolidadas de valorización han impulsado el interés por integrarlos en esquemas circulares de producción. En este contexto, la pirólisis destaca como una alternativa eficaz para fraccionar los MTWT en sólidos, gases y líquidos con potencial valor comercial. En particular, el líquido pirolítico es una mezcla compleja de hidrocarburos con aplicaciones como combustible, solvente o aditivo para asfaltos y otras aplicaciones de ingeniería. Sin embargo, su naturaleza multicomponente requiere procesos de mejoramiento para dirigir la selectividad hacia compuestos de mayor valor, como *d,l*-limoneno, *p*-cimeno o monoaromáticos.

Esta investigación doctoral estudió el rol de catalizadores bifuncionales Pd/ZrO_2-TiO_2 en la generación de *p*-cimeno a partir del limoneno pirolítico derivado de MTWT. En una primera etapa, se estudió la pirólisis no catalítica de MTWT en un sistema de micro-pirólisis (CDS 5200 Pyroprobe), desarrollando un modelo cinético mecanístico formulado bajo un esquema de reactor batch. El modelo, validado fisicoquímicamente, describió la formación de limoneno mediante rupturas homolíticas C–C del caucho natural, seguida de ciclización intramolecular y reacciones tipo Diels–Alder entre unidades de isopreno, así como su conversión secundaria a mayores temperaturas. Este análisis permitió predecir la composición de limoneno en los vapores alimentados al reactor catalítico y controlar las condiciones de reacción.

Con la alimentación definida, se sintetizaron y caracterizaron soportes ácidos basados en TiO_2 modificados con distintas cargas de ZrO_2. La incorporación de circonia permitió modular la densidad y la fuerza de los sitios ácidos, manteniendo la predominancia de acidez Lewis en los soportes. Esta modulación se reflejó en una actividad intrínseca hacia la transformación del limoneno pirolítico a *p*-cimeno. Posteriormente, se impregnó Pd sobre TiO_2 y sobre el óxido mixto ZrO_2-TiO_2; este último mostró mayor rendimiento a *p*-cimeno. La adición de Pd permitió un efecto bifuncional en el cual la isomerización mediada por los sitios ácidos y la deshidrogenación promovida por el metal actuaron de manera sinérgica, para dirigir las rutas de reacción hacia mayor selectividad a *p*-cimeno. La conversión catalítica de vapores ricos en limoneno desde la pirólisis de caucho natural se evaluó en un sistema de micro-pirólisis en tándem (Rx-3050TR). Los resultados mostraron que los soportes con acidez Lewis débil maximizan la formación de *p*-cimeno, en coherencia con el principio de Sabatier, mientras que la presencia de Pd intensificó este comportamiento y favoreció rutas de deshidrogenación. El modelo cinético tipo Langmuir–Hinshelwood desarrollado reprodujo las tendencias experimentales y capturó tanto los efectos de competitividad adsorptiva, propia de mezclas pirolíticas, como la cooperación metal–ácido.

Esta tesis establece un marco mecanístico y cinético que vincula la formación no catalítica de limoneno pirolítico con su posterior valorización catalítica hacia *p*-cimeno, aportando fundamentos para el diseño y escalamiento de procesos de valorización termoquímica de neumáticos mineros fuera de uso en esquemas circulares y sostenibles.

ABSTRACT

Waste mining truck tires (MTWT) are a priority waste stream under Chile's Extended Producer Responsibility Law (REP 20.920). Their high annual generation (>40,000 ton), slow degradation, and the absence of consolidated valorization routes have intensified interest in integrating these materials into circular production schemes. In this context, pyrolysis emerges as an effective pathway to convert MTWT into solid, gaseous, and liquid fractions with potential commercial values. Among these products, the pyrolytic liquid (LPN) is a complex mixture of hydrocarbons with potential applications as a fuel, solvent, or asphalt additive. However, its multicomponent nature requires upgrading processes to steer selectivity toward higher-value compounds such as *d,l*-limonene, *p*-cymene, or monoaromatics (BTX).

This doctoral research investigated the role of Pd/ZrO_2–TiO_2 bifunctional catalysts in the generation of *p*-cymene from pyrolytic limonene derived from MTWT. First, the non-catalytic pyrolysis of MTWT was studied in a micro-pyrolysis system (CDS 5200 Pyroprobe), and a mechanistic kinetic model framed within a batch-reactor scheme was developed. The model, validated through physicochemical consistency, described limonene formation via homolytic C–C bond scission of natural rubber, followed by intramolecular cyclization and Diels–Alder reactions between isoprene units, as well as its secondary conversion at higher temperatures. This analysis enabled the accurate prediction of the vapor limonene composition fed to the catalytic reactor and ensured control over the reaction conditions.

With the feed composition defined, acid supports based on TiO_2 modified with different ZrO_2 loadings were synthesized and characterized. Zirconia incorporation allowed modulation of the density and strength of Lewis acidic sites while preserving the predominance of Lewis acidity in the supports, which was reflected in an intrinsic activity toward converting pyrolytic limonene into p-cymene. Pd was then impregnated onto TiO_2 and onto the ZrO_2 –TiO_2 mixed oxide, the latter exhibiting the highest intrinsic performance and generating a bifunctional effect in which acid-mediated isomerization and metal-mediated dehydrogenation acted synergistically to direct the reaction pathways toward higher *p*-cymene selectivity.

The catalytic upgrading of limonene-rich vapors produced from natural-rubber pyrolysis was evaluated in a tandem micro-pyrolysis system (Rx-3050TR). Results showed that Lewis-acid supports with weaker acidity maximize *p*-cymene formation, consistent with the Sabatier principle, while Pd further intensified this behavior and promoted dehydrogenation routes. The developed Langmuir–Hinshelwood kinetic model successfully reproduced experimental trends and captured the competitive adsorption effects inherent to pyrolytic mixtures, as well as the metal–acid cooperation.

This thesis establishes an integrated mechanistic and kinetic framework, linking the non-catalytic formation of pyrolytic limonene with its catalytic upgrading to *p*-cymene. These findings provide scientific bases for the design and scale-up of thermochemical valorization processes for mining truck waste tires within circular and sustainable schemes.

CONTENT

List of Figures

List of Tables

Outline of thesis

This doctoral thesis comprises four chapters, three of which address the specific objectives of the project related to the catalytic upgrading of pyrolytic limonene into cymene as a route to valorize waste tires from mining trucks, while the remaining chapter provides the motivation and scientific background supporting this study.

- Chapter 1 – Introduction: Presents the motivation, scientific background, and research objectives of the thesis, with emphasis on the formation of pyrolytic limonene from natural-rubber pyrolysis and its catalytic transformation into cymene as a viable route for chemical upgrading.

- Chapter 2 - Non-catalytic pyrolysis (Objective I): Develops and validates a mechanistic kinetic model that describes the formation and secondary conversion of pyrolytic limonene from natural-rubber pyrolysis. This chapter integrates TGA and Py-GC/MS experiments to elucidate the reaction pathways of natural rubber and establishes a predictive framework used to define feed composition and reaction conditions for the catalytic studies of Chapter 3.

- Chapter 3 – Catalytic upgrading (Objectives II–III): Examines the catalytic conversion of pyrolytic limonene into cymene over Lewis-acid supports and Pd/Lewis bifunctional catalysts using a two-stage microreactor configuration. The chapter investigates the influence of surface acidity, metal–acid synergy, and competitive adsorption on the upgrading pathways and integrates Langmuir–Hinshelwood kinetic modeling.

- Chapter 4 – Conclusions and outlook: Integrates the main findings of the kinetic and catalytic studies, establishes a mechanistic framework linking non-catalytic limonene formation with its catalytic upgrading to cymene, and outlines future research directions related to model validation, catalyst stability, operando characterization, and the potential scale-up of catalytic pyrolysis for tire-waste valorization.

Chapter 1. Introduction

1.1. Context and motivation

Around the world, the accumulation and management of waste tires (WT) have become a growing environmental concern. Each year, nearly 1.5 billion of tires — about 17 million tons — reach the end of their service life and accumulate in landfills or open spaces [1]. Due to their complex, non-biodegradable structure, these materials persist for decades, leading to land and water contamination, spontaneous fires, and the release of hazardous compounds that endanger both human and ecological health [2]. This situation has prompted governments and industries to adopt new policies aimed at promoting the reuse and valorization of WT from both environmental and economic perspectives.

In Chile, approximately 178,000 tons of WT are generated every year, and nearly 90% are either improperly disposed or have an unknown destination [3,4]. The mining sector is the country's main industrial activity and generates about 49,000 tons of mining truck waste tires (MTWTs). These tires, typically 2–4 m in diameter and weighing over 3 tons each, have short service lives and are difficult to transport or process because of their size. According to the Chilean Recycling Industry Association (ANIR), by 2022 only 13.1 % of these tires were treated through conventional methods such as shredding, retreading, or energy recovery, while the destination of the vast majority remained uncertain [4,5]. To address the growing accumulation of waste tires, the Chilean government enacted the Extended Producer Responsibility (EPR) Law 20,920 in 2016, which designated WT as a priority product within the national waste management framework. This regulation established ambitious collection and recycling targets –90 % for passenger-car tires and 100 % for mining tires by 2030- reflecting the critical role of the mining sector in the country's waste generation profile [6]. The legislation has driven mining companies and tire manufacturers to explore strategies for tire recovery and reuse within a circular-economy model.

Traditionally, WT are mechanically recycled to recover rubber, steel, and textile fibers from shredded or ground tires for use in construction materials, asphalt modification, and molded rubber products. Although these applications are widespread, they generally produce low-value materials with limited mechanical performance due to contamination and loss of elasticity [1,7]. In recent years, increasing attention has been directed to thermochemical processes, essentially pyrolysis,

which is considered the most efficient route for tire valorization because it enables the conversion of tire polymers into three values products -solid, liquid and gaseous fraction- with interesting chemical characteristics [8–10]. Several companies in Chile have adopted or are developing pyrolysis-based technologies for tire recycling. These include the Eco-Diesel Plastic and Tire Plant in Valparaíso, the Arrigoni Ambiental NFU plant in San Francisco de Mostazal, which has the capacity to process 10,000 tons of waste tires per year, and the Cratos plant in Penco, which processes approximately 7,5 tons per week. In northern Chile, the Kal Tire plant in Antofagasta specializes in recycling mining truck tires, with an installed capacity of 7,200 tons per year. Additionally, major mining companies such as Anglo American and Codelco have begun adopting pyrolysis-based valorization strategies for tire waste management [11–13].

Pyrolysis is a thermal degradation process that occurs in the absence of oxygen at temperatures between 350 °C and 500 °C. During tire pyrolysis, three fractions of products are obtained: a liquid (35–65 wt%), a solid (12–45 wt%) primarily composed of carbonaceous material (recovered carbon black), and a gas (10–35 wt%) known as tire pyrolytic gas (TPG) [14,15]. The relative proportions of these fractions depend on the operating conditions and on the composition of the tire. The pyrolytic gas, consisting mainly of light hydrocarbons (C_1–C_4) and hydrogen, is often used as an energy source to fulfill the energy requirements of the reactor due to its high calorific value (30–50 MJ m^{-3}) [16]. The solid product, rich in carbon (>90 %), is employed as fuel, as additive for concretes, as a substitute of carbon black for producing new tires or as a precursor for activated carbon [10,17]. Meanwhile, the liquid fraction contains a complex mixture of organic compounds such as limonene, isoprene, styrene, terpenes, and aromatic hydrocarbons including benzene, toluene, and xylene (BTX) [14,18,19]. Currently, this liquid is used as a low-grade fuel, often for replacing diesel grade 6 in boilers, while other applications remain in early stages (TRL<5) [12,20]. However, the presence of high-value compounds such as *d,l*-limonene, typically reported at concentrations of approximately 7-10 wt% in the pyrolytic oil from tires with high natural rubber content [21–23], has stimulated increasing research interest in strategies aimed at upgrading the pyrolytic liquid into more valuable chemicals [24–28]. Recent market quotations for industrial-scale purchases indicate that *d,l*-limonene can be obtained for as low as 1-10 USD·kg^{-1} depending on purity and supplier [29]. To further illustrate the potential economic relevance of limonene upgrading, a simple order-of-magnitude estimation can be considered. Assuming a representative pyrolysis facility producing on the order of 8,000 L·day^{-1} of pyrolytic oil [30], with a typical

density of approximately 0.87 kg·L^{-1} [31] , and a limonene content in the range of 7 - 10 wt%, the resulting limonene production would be approximately 490–700 kg·day^{-1}. Using the reported industrial-scale price range for *d,l*-limonene (1–10 USD·kg^{-1}), this corresponds to a gross revenue potential on the order of 0.5–7 kUSD·day^{-1}. Although this estimate neglects separation efficiency, purification costs, operating expenses, and market variability, it highlights the significant economic incentive associated with the selective upgrading of limonene into higher-value aromatics such as *p*-cymene. This upgrading can be performed either on the condensed liquid fraction or directly on the pyrolysis vapors before condensation, enabling the formation of an upgraded oil enriched in *p*-cymene and other aromatics.

Literature reports confirm that *p*-cymene can be obtained from *d,l*-limonene through isomerization into intermediates such as terpinolene and, terpinenes followed by dehydrogenation to *p*-cymene [32,33]. The isomerization reactions are typically catalyzed by Lewis's acid sites, whereas metallic sites facilitate dehydrogenation, posing the challenge of developing bifunctional catalysts or tandem reactor systems (Figure 1.1).

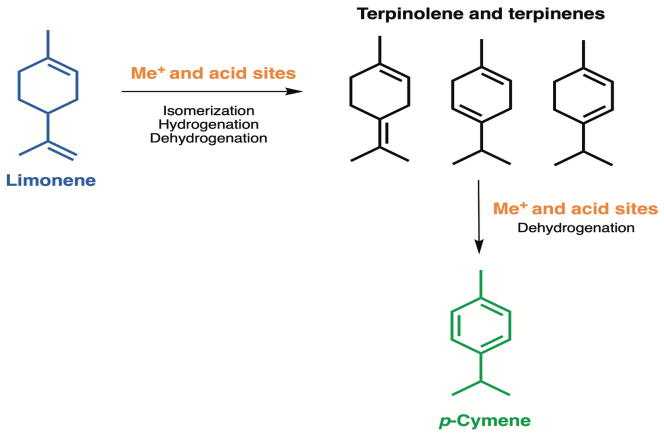

Figure 1.1. Simplified reaction mechanism for the transformation of limonene into *p*-cymene (adapted [32]).

p-Cymene represents a valuable intermediate in numerous chemical industries, notably in the manufacture of fragrances, perfumes, flavorings, and pharmaceutical products [33]. Beyond these applications, it is also considered a key platform molecule for the synthesis of high-added-value aromatics, with the conversion of *p*-cymene to terephthalic acid standing out as one of its most significant transformations [34]. Available market data indicate that *p*-cymene is currently listed on commercial trade platforms at approximately 20 - 30 USD·kg^{-1} (2025) corresponding to roughly

two to three times the market value of limonene [29,35]. These orders of magnitude underscore the economic incentive for upgrading *d,l*-limonene into *p*-cymene in a valorization process.

Conventionally, *p*-cymene is produced via Friedel–Crafts alkylation of benzene with methyl and isopropyl halides, or toluene with isopropyl alcohol, catalyzed by acidic solutions of $AlCl_3$, BF_3, or H_2SO_4. This synthesis route presents several drawbacks due to the use of toxic reagents (benzene, toluene, and strong acids). Logistically, it also involves issues of corrosion, acid disposal, phase separation, and the generation of unwanted o- and m-cymene isomers [36,37].

Under this context, producing *p*-cymene from waste mining tires through catalytic pyrolysis represents a valuable opportunity to generate high-added-value chemicals from industrial waste, supporting the development of a sustainable circular economy.

1.2. Current state and research gaps

The pyrolysis of waste tires has been widely studied as a thermochemical route for the recovery of hydrocarbons and chemical feedstocks. Extensive research has focused on understanding the factors that determine the composition of the pyrolytic liquid, which mainly depend on the type of tire, heating rate, and pyrolysis temperature [14,38,39]. Tires containing higher proportions of natural rubber (NR) generally yield greater amounts of limonene since this compound originates from the depolymerization of natural rubber [22,40,41]. In contrast, higher pyrolysis temperatures and longer vapor residence times favor cracking and cyclization reactions, leading to extensive chain fragmentation and higher formation of light unsaturated species—such as isoprene, cycloalkenes, and alkenes—while reducing limonene and promoting the generation of aromatics.

A widely accepted mechanistic scheme describing the formation of limonene from natural rubber has been established in the literature and it's summarized in Figure 1.2 [21,41–44]. In this scheme, thermal cleavage of the ß-bond generates allylic radicals (A – B), which may undergo intramolecular cyclization or depropagation to form limonene (L), 1,5-dimethyl-5-ethyl-cyclohexene (C), and isoprene (I). Some authors have noted that steric hindrance can limit the cyclization of radical A, favoring isoprene formation instead [41,43]. In addition, Diels–Alder reactions between limonene and isoprene—or the reverse cleavage of limonene into two isoprene units—have been proposed, although their relevance under pyrolysis conditions remains uncertain [45,46]. At higher temperatures, β-scission and ring-opening reactions undergoes to form alkatriene intermediates (D). These alkatrienes subsequently cyclize into cycloalkenes (E–F), which then evolve into BTX aromatics through dehydrogenation and dealkylation reactions.

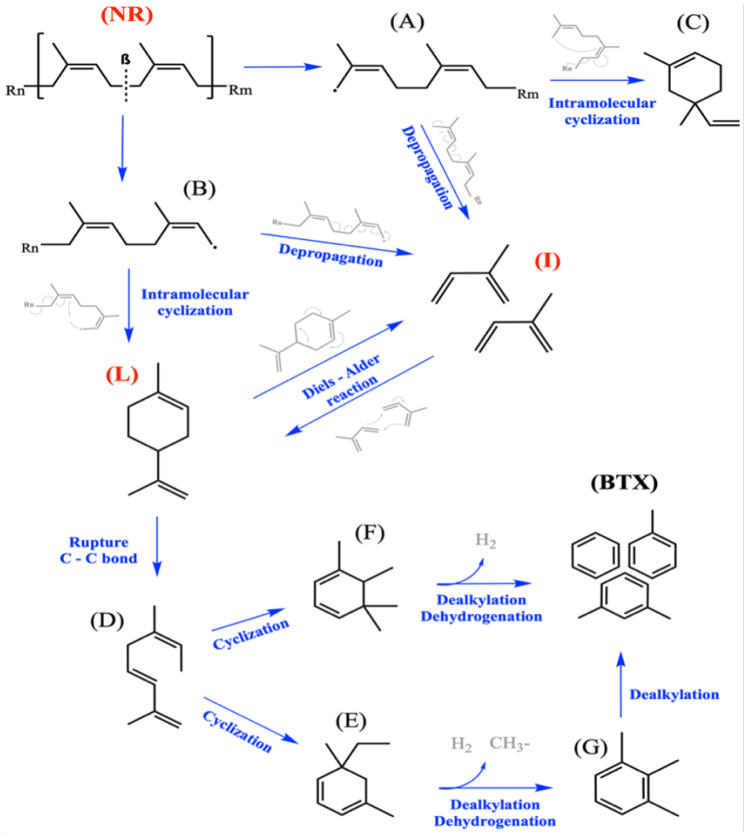

Figure 1.2. Reaction scheme proposed in literature for the formation of limonene from the degradation of natural rubber [21,41–44]. (NR) natural rubber, (A) and (B) radicals, (C) 1,5-dimethyl-5-ethyl-cyclohexene, (I) isoprene, (L) limonene, (D) alkatriene, (E) 5-ethyl-1,5-dimethyl-1,3-cyclohexadiene, (F) 1,5,5,6-tetramethyl-1,3-cyclohexadiene, (G) 1,2,3-trimethyl-benezene, (BTX) benzene, toluene, and xylenes.

Although this mechanistic reaction scheme has been proposed for the thermal decomposition of waste tires, most kinetic models reported in pyrolysis research are primarily associated with solid-phase decomposition, typically derived from thermogravimetric analysis [47,48]. These models largely rely on iso-conversional or lumped global approaches aimed at estimating apparent activation energies or overall yields [48], rather than resolving reaction rates of individual chemical species. While operating conditions can influence the yield of the solid, liquid and gas fractions from waste tire pyrolysis, the specific composition of these products can only be tailored by using catalysts. The catalytic upgrading of tire-derived vapors has been widely explored as a route to enhance the selectivity to valuable compounds such as monoaromatics [16,25,42,49], limonene

[21,26,50], and to reduce S, N heteroatoms [8,27,51]. Numerous catalytic systems and reactor configurations have been employed, including in-situ and ex-situ arrangements, the latter allowing direct contact of the pyrolysis vapors with a downstream catalytic bed [14,28,52]. This configuration facilitates the separate analysis of the thermal and catalytic stages, enabling better control of the reaction environment and a clearer interpretation of catalytic effects.

Given that the formation of *p*-cymene from limonene involves isomerization step promoted by Lewis's acid sites, the selection of appropriate acid catalysts or support is critical. Among them, zeolites (HZSM-5, HY, β, MOR, USY) have been the most extensively used, representing approximately 46 % of 71 studies analyzed in the literature (Figure 1.3).

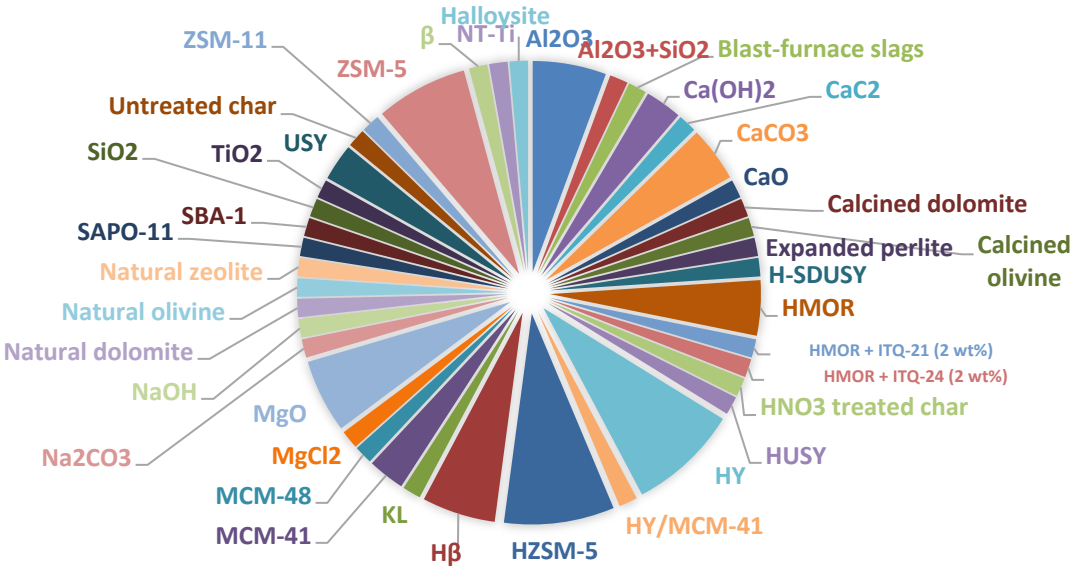

Figure 1.3. Distribution of supports used in studies on the catalytic pyrolysis of tire-derived materials. Zeolites account for approximately 46 % of 71 studies, highlighting their predominance as acidic support (Data source [14]).

However, controlling the presence and strength of Brønsted acid sites in zeolites is challenging, and excessive protonic strength often leads to over-cracking, poly-aromatization, and coke deposition, resulting in rapid catalyst deactivation [14,53]. These limitations have motivated the exploration of mixed-oxide catalysts, such as TiO_2–ZrO_2 which exhibit exclusively Lewis's acid sites. In addition, their acid site density and strength can be tuned by modifying their composition and metal-oxide ratio, offering a more controllable surface chemistry than zeolites [54–56].

Given that the transformation of limonene into *p*-cymene requires not only Lewis-acid-driven isomerization but also dehydrogenation steps commonly promoted by metallic sites. This motivated the evaluation of metal-loaded catalysts in ex-situ pyrolysis studies. Osorio-Vargas et al. [42] investigated the effect of Pd, Co, and Ni supported on inert SiO_2 and found that Co primarily promoted cracking, yielding cycloalkenes and alkenes, whereas Ni led to aromatic products. Importantly, Pd exhibited the highest selectivity toward *p*-cymene (15%) compared with only 3% for Ni. Similar trends were reported by Yilmazoglu et al. [57] using Al_2O_3-based supported metals, where Pd and Pt showed high *p*-cymene selectivity, with Pd outperforming Pt and reaching up to 80% yield. These results collectively indicate that Pd possesses a superior dehydrogenation capability that favors the formation of *p*-cymene from isomerized limonene intermediates.

The incorporation of Pd nanoparticles onto Lewis-acid supports provides metallic sites capable of catalyzing hydrogen-transfer and dehydrogenation reactions, enabling the selective conversion of isomerization intermediates into *p*-cymene. However, despite existing studies employing Pd-supported acidic catalysts [16,32], the literature offers incomplete conclusions regarding whether Pd modifies the intrinsic acidity or the nature of the acid sites in the support. Metal–support interactions may alter both the electronic environment and the distribution or strength of Lewis sites. Therefore, understanding how Pd dispersion influences Lewis's acidity—and how this bifunctional synergy governs limonene upgrading—remains an open question.

Despite the growing number of studies on catalytic pyrolysis of tire-vapor upgrading, most efforts have focused on optimizing operational variables and qualitatively assessing product selectivity, rather than elucidating the mechanistic basis of the transformation. To place this gap into a broader perspective, a bibliometric survey of 2,500 peer-reviewed articles published between 2018 and 2025 was performed using VOSviewer (Figure 1.4).

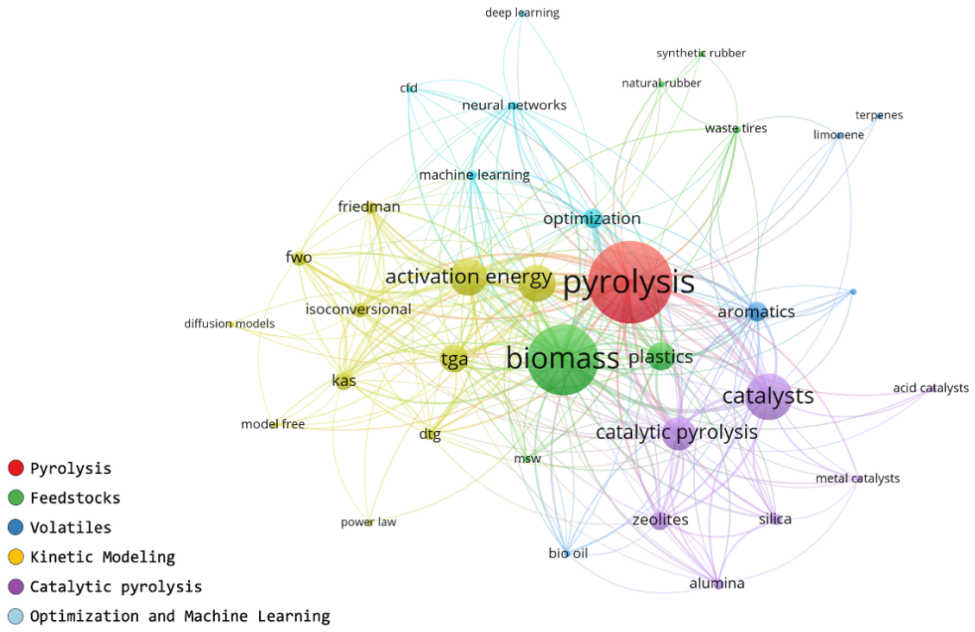

Figure 1.4. Bibliometric co-occurrence map of pyrolysis research, based on keyword analysis and Association Strength normalization, illustrating the main clusters and subdomains in 2,522 publications (2018–2025).

The co-occurrence network generated under the Association Strength normalization clearly illustrates this imbalance: keywords related to waste tires—and even more notably limonene and other terpenes intermediates—form distant and weakly connected clusters relative to terms such as kinetic modeling, activation energy, reaction mechanism, and iso-conversional.

Notably, *p*-cymene does not appear as a recurrent keyword within the dataset, reflecting the extremely limited number of studies that address its formation during pyrolysis and the absence of a consolidated research field around cymene selectivity, reaction pathways, or kinetic modeling.

This spatial separation indicates that catalytic tire-vapor upgrading remains largely disconnected from kinetic modeling. Moreover, the kinetic cluster itself is overwhelmingly dominated by solid-phase TGA studies and iso-conversional methods (model-free and model approaches), whose primary purpose is the estimation of apparent activation energies. While these approaches are valuable for characterizing thermal decomposition, they offer limited insight into elementary steps, competitive adsorption phenomena, or vapor-phase reaction pathways. Consequently, across pyrolysis research as a whole—regardless of feedstock—there is a noticeable absence of kinetic models grounded in reaction mechanisms. Within this broader context, research involving *d,l*-

limonene and *p*-cymene as model compounds is particularly scarce, reflecting both the incipient development of waste tires as a feedstock and the limited attention given to the reaction network governing cymene formation.

1.2.1. Kinetic modeling approaches in pyrolysis systems

As evidenced by the preceding bibliometric analysis, most kinetic studies in the field of pyrolysis are focused on tracking solid-phase degradation using thermogravimetric analysis (TGA). These studies predominantly rely on iso-conversional methods—such as Kissinger–Akahira–Sunose (KAS) and Flynn–Wall–Ozawa (FWO)—or on lumped solid-state reaction models, with the primary objective of estimating global apparent activation energies under different operating conditions and catalytic formulations.

Among the limited number of kinetic studies specifically addressing the catalytic pyrolysis of waste tires, the work of Qu et al.[58] stands out. In this study, ZSM-5 and MnO_2 catalysts were evaluated under different heating rates using a TG–MS system. Apparent activation energies were calculated using both model-free iso-conversional methods (KAS and FWO) and solid-state reaction models, including power-law, one-dimensional diffusion, and contracting geometry models. The authors compared the resulting activation energies as well as the product selectivity obtained for each catalyst. While this approach enables an energetic comparison between catalysts and provides useful information regarding their influence on the overall thermal degradation behavior, it remains intrinsically limited by its reliance on solid-phase kinetic models. As such, it does not directly describe the fluid-phase environment in which secondary reactions of higher-value chemical species are expected to occur. Along similar lines, Wang et al. [59] recently employed a TG–FTIR–GC–MS system to investigate the catalytic pyrolysis of waste tires using low-cost catalysts such as red mud and fly ash. In addition to calculating kinetic parameters using iso-conversional and model-fitting approaches, the authors attempted to validate the kinetic description through thermodynamic analysis and complemented their study by characterizing the composition of the evolved gases, proposing possible catalytic reaction pathways. Despite this more comprehensive experimental characterization, the kinetic framework adopted in this study remains fundamentally rooted in solid-phase degradation models. As a result, it neither captures the mechanistic nature of surface-mediated catalytic transformations nor enables the extraction of compound-specific activation energies that could quantitatively describe how a catalyst promotes the formation of targeted products in the vapor phase.

Within the field of catalytic waste tire pyrolysis, only a limited number of studies have explicitly addressed the reaction pathways of volatile compounds formed in the pyrolytic vapor phase. Among these, the works developed by the Osorio-Vargas and Tavera-Ruiz research groups stand out for their use of an ex-situ Py–GC/MS configuration combined with metal-based catalysts supported on acidic materials to investigate the formation of high-value aromatics, including BTX compounds and p-cymene [16,25,42,60]. Focusing on the work by Osorio-Vargas et al. [25], a power-law kinetic model was employed to quantitatively track the formation of individual volatile compounds, including BTX aromatics and *p*-cymene, and to estimate apparent activation energies under catalytic conditions using acidic catalysts with varying Lewis-to-Brønsted acidity ratios. However, the resulting kinetic description remains phenomenological, since it does not explicitly account for surface adsorption phenomena, competitive interactions among vapor-phase species.

Taken together, these studies reveal a clear methodological gap in the kinetic description of catalytic waste tire pyrolysis. Although solid-phase TGA-based and iso-conversional approaches dominate the field, they do not capture the vapor-phase transformations responsible for the formation of high-value products. Power-law models applied to individual volatile species represent an important step toward compound-specific analysis; however, they remain phenomenological and do not explicitly account for surface-mediated reaction mechanisms. Consequently, kinetic modeling remains largely decoupled from catalytic vapor upgrading, as evidenced by the scarce application of mechanistic formulations—such as Langmuir–Hinshelwood models—to complex multicomponent vapor environments derived from waste tires.

Within this context, and particularly for the catalytic upgrading of pyrolytic vapors derived from waste mining truck tires, these limitations clearly define the central motivations of the present doctoral research: (i) to elucidate the bifunctional metal–support interactions governing the catalytic upgrading of pyrolytic limonene to cymene, (ii) to propose a mechanistic reaction scheme capable of describing the catalytic cycle, and (iii) to derive a kinetic model consistent with the proposed mechanism. These motivations lead directly to the hypotheses and objectives presented in the following section.

1.3. Hypothesis and objectives

1.3.1. Hypothesis

The use of Pd-based catalysts supported on mixed oxides with a controlled density of Lewis acid sites will induce a bifunctional effect that enhances both the yield and selectivity towards cymene during the upgrading of pyrolytic vapors from waste tires. This improvement is attributed to the sequential promotion of isomerization and dehydrogenation reactions occurring on support and metal sites, respectively.

1.3.2. Objectives

General objective

To elucidate the bifunctional role of Pd/ZrO_2–TiO_2 catalysts in the selective conversion of pyrolytic vapors from waste mining truck tires into cymene, by correlating catalyst physicochemical properties with reaction mechanisms governing isomerization and dehydrogenation under ex-situ catalytic pyrolysis conditions.

Specific objectives

I. To determine the decomposition routes in the non-catalytic pyrolysis of waste mining tires and their main polymeric components, and to establish the reaction conditions that favor the formation of limonene as a precursor of cymene.

II. To evaluate and quantify the bifunctional acid–metal effect on *p*-cymene formation from the pyrolytic vapors of waste mining tires, using Pd/TiO_2-ZrO_2 catalysts with different densities of Lewis acid sites.

III. To develop a reaction mechanism and construct a consistent kinetic model describing the formation of cymene during the ex-situ catalytic pyrolysis of waste mining tires, supporting the rational design of new catalytic valorization strategies for these residues.

Chapter 2. Understanding the limonene synthesis from waste tire pyrolysis.

Chapter reproduced from Poblete et al. (2024). https://doi.org/10.1016/j.jaap.2025.107207

This chapter addresses the specific objective I of the doctoral thesis and provides a comprehensive analysis on the conversion of waste tires to produce pyrolytic limonene.

The pyrolysis of mining truck waste tires (MTWT) produces a multicomponent liquid abundant in limonene and its derivatives, including cymene and single-ring aromatics, among others. Nonetheless, although crucial for enhancing the chemical valorization of mining truck waste tires (MTWT), the reaction pathways for the synthesis and subsequent transformation of pyrolytic limonene remain insufficiently comprehended. This study introduces an innovative kinetic methodology for analyzing limonene production during MTWT pyrolysis. The study combines thermogravimetric analysis (TGA) and analytical pyrolysis (Py-GC-MS) to analyze the pyrolytic behavior of MTWT and its constituent polymers, natural rubber (NR), butadiene rubber (BR), and styrene-butadiene rubber (SBR). The results of Py-GC-MS experiments showed that limonene is generated from natural rubber after C-C cleavage of polymeric chains followed by (i) an intramolecular cyclization or (ii) a Diels-Alder reaction of two isoprene units. Thereafter, limonene undergoes secondary reactions to generate cycloalkenes and aromatics. Our findings show that the formation of isoprene from the cleavage reaction of NR has the lowest activation energy (53.3 kJ/mol) within the reaction mechanism, while limonene conversion into tertiary products like aromatics or cycloalkenes requires higher activation energies (219 kJ/mol). This result suggests that catalytic materials, higher residence times or lower reaction temperatures are required to control product distribution. The kinetic model presented in this chapter is further used (Chapter 3) for interpreting ex-situ catalytic pyrolysis of pyrolytic limonene conversion into cymene.

2.1. Introduction

In Chile, around 178,000 metric tons of waste tires were generated in 2022, with Mining Truck Waste Tires (MTWT) accounting for 37%. The unregulated disposal of MTWT and its limited biodegradability causes significant environmental issues such as water and soil contamination from leaching and the possibility of fire risk [4,5]. Consequently, Chilean Law 20920/2016 mandates the recycling of 100% of MTWT by 2030 to mitigate these impacts [6]. Traditionally, the revalorization of MTWT has been concentrated in mechanical processing for recovering steel and pulverized rubber to be used as additive for concretes, asphalts and recreational parks [51,61]. However, in recent years, the focus has shifted towards chemical and energetic valorization through pyrolysis. Pyrolysis is a thermochemical process taking place in an O_2-depleted atmosphere that converts MTWT into three valuable fractions: (i) recovered carbon black (rCB), (ii) pyrolytic tire liquid (PTL) and (iii) pyrolytic tire gas (PTG) [14,62] .In Chile, pyrolysis plants for the revalorization of waste tires have already been established [11,12]. For instance, the company Kal Tire has set up a pyrolysis plant for processing mining truck tires with a capacity of 7,200 metric tons per year (11% of the estimated production in Chile). Since MTWT pyrolysis represents an emerging business model in Chile, there exists a significant possibility to broaden the market for pyrolysis products across several sectors, including fuels, engineering additives, solvents, and others [11].

Tires are generally made up of natural rubber (NR), butadiene rubber (BR) and styrene-butadiene rubber (SBR). The proportion of these polymers dominates the mechanical performance; thus, tire composition varies depending on the intended application (light or heavy vehicles), and the manufacturer [63,64]. According to the United States Manufacturers Association, tires for trucks contain 75% natural rubber in their polymeric fraction. On the other hand, light vehicles have 56% of synthetic rubbers in their total polymeric fraction [64]. Rowhani et al. [63] found that tires from heavy vehicles contain 65% natural rubber, while tires from smaller automobiles include 35% natural rubber and a higher content of synthetic rubbers and additives. Thus, it is anticipated that, natural rubber would be the primary polymeric component in mining trucks waste tires.

The pyrolysis liquids from waste tires hold the greatest commercial value and potential to be upgraded to fine chemicals among pyrolysis products. PTLs contain aliphatic and aromatic hydrocarbons, along with other chemical species which can be recovered as a fuel (HHV = 38–45 MJ/kg) [65], fractionated towards fine chemicals, as engineering additives and more [66,67].

Limonene, one of the most abundant compounds in PTL, is a valuable industrial compound. It is widely employed in the production of food additives, specialty chemicals (such as monoaromatics), perfume additives, and pharmaceuticals [41,68]. This relevance has driven several studies focused on its recovery and purification from PTL, as well as optimizing operational conditions to increase its yield and selectivity [21,42–45,69–72]. Zhang et al. [70,71] studied the recovery and separation of limonene from PTL and proposed to epoxidize limonene upon oxidation to subsequently separate it from the crude fraction through simple distillation utilizing polyoxometalate immobilized on SBA-15 [71]. Despite advancements in purification strategies, most studies have primarily focused on optimizing limonene formation under various pyrolysis conditions. Several studies have explored the use of catalytic materials to enhance limonene selectivity and control its conversion pathways. Menares et al. [26] investigated the effect of metal-supported catalysts (Ni, Pd, Co, Fe) on limonene yield, reporting that Co/SiO_2 significantly increased limonene selectivity at 370 °C and a 1:5 (tire:catalyst ratio). Furthermore, Qu et al. [73] employed acid-modified zeolites to selectively convert limonene into monoaromatics, demonstrating that the acidity and pore structure of the catalyst played a crucial role in directing the reaction pathways. However, these authors did not provide a comprehensive discussion on the reaction pathways nor on the kinetic relevant steps involved in limonene formation from waste tires. This information is paramount to understand the intrinsic decomposition mechanisms of waste tires, while it also establishes a baseline for designing catalytic systems focused on the functionalities of active sites.

Danon et al. [21] identified a direct correlation between the proportion of natural rubber in waste tires and the yield of limonene and isoprene in PTL, although they did not explore the kinetic or mechanistic explanations for this relationship. More recently, Osorio-Vargas et al. [16] further investigated this correlation through micropyrolysis coupled to gas chromatograph/mass spectrometer (Py-GC-MS) experiments with natural rubber, butadiene rubber, styrene-butadiene rubber, and waste tires at 450 °C to pinpoint the primary source of limonene formation. Their findings indicated that limonene and isoprene were the predominant products from natural rubber, with selectivities of 56.5% and 19.6%, respectively. In contrast, butadiene rubber and styrene-butadiene rubber primarily produced 4-vinylcyclohexene. This suggests that, under pyrolysis conditions, limonene predominantly originates from NR, with minimal interactions or contributions from styrene-butadiene rubber or butadiene rubber.

To further investigate the influence of temperature and heating rate on limonene production Xu et al. [43] performed fast pyrolysis experiments of bicycle tires using a Py-GC-MS system, analyzing the effects of temperature (700-1000 °C) and heating rates on product distribution in the pyrolytic vapors. Limonene showed a decrease when the temperature reached 800 °C, which was again attributed to the production of aromatic compounds by secondary cyclization and aromatization reactions. Similarly, Mkhize et al [40]. performed pyrolysis experiments of used truck tires, and observed that the limonene yield peaked at 475 °C and 25 °C/min but sharply decreased at higher temperatures, aligning with the trend reported by Xu et al. These findings are consistent with other studies indicating that limonene acts as an intermediate that can further degrade into aromatic compounds through cyclization and aromatization reactions at elevated temperatures [51]. In addition to these reaction pathways, several authors have proposed that limonene can also degrade into isoprene or form from isoprene through Diels-Alder reactions. For example, Menares et al. [45] reported that at temperatures above 600 °C, the Diels-Alder reaction between limonene and isoprene may reach equilibrium. Similarly, Kar et al. [46] reported a computational study of isoprene dimerization, where limonene formation was controlled by kinetics at low temperatures. These authors have proposed similar reaction pathways describing the pyrolysis of NR and the formation of limonene (Figure 1.2), based on the correlation between pyrolysis temperature and product distribution. While significant, these reaction pathways have not been systematically validated through kinetic modelling.

Most kinetic studies in pyrolysis focus on solid degradation by employing both model-based approaches (e.g., power-law, 1D, 2D, and 3D diffusion, contracting sphere) and model-free methods (e.g., Friedman method, FWO, KAS) to interpret thermogravimetric data [74–77]. These studies, typically conducted at low heating rates (< 100 ºC min^{-1}), provide limited insights into fast pyrolysis reactions. Moreover, the reported kinetic parameters are restricted to the solid conversion being very limited for explaining fast pyrolysis reactions in volatiles. Pioneering work by Osorio-Vargas et al. [25], using Py-GC-MS, has demonstrated the potential for quantifying volatile species like BTX and cymene. However, the kinetic model developed in this study does not derive from elementary reaction steps, limit its applicability in defining specific reaction pathways and their relative importance under varying conditions.

Given current limitations in our understanding of limonene formation and the kinetic behavior of waste tires during pyrolysis, the goal of this research is to develop a novel kinetic approach based

on elementary reaction steps for studying the formation and transformation of limonene during waste tire pyrolysis. The model incorporates both solid and gas-phase phenomena, allowing for a comprehensive analysis of the reaction network. This approach not only quantifies the formation and conversion of limonene but also provides kinetic parameters that can serve for reactor design strategies aimed at selective limonene recovery or controlled conversion to secondary products such as isoprene, cycloalkenes, and aromatics.

2.2. Material and methods

2.2.1. Feedstock and Chemical reagents

Mining truck waste tires were provided as granules by a local pyrolysis company. In addition, polyisoprene or natural rubber (NR, CAS 104389-31-3), with a molecular weight of 38000 $g \cdot mol^{-1}$, polybutadiene rubber (BR) and styrene-butadiene rubber (SBR) were purchased from Merck (Chile). Elemental and proximate composition of mining truck waste tires, natural rubber, polybutadiene rubber, and styrene-butadiene rubber were determined according to ASTM D3172 and ASTM D5291 standards [78,79] respectively (Table A-2.1). Moreover, D, L-limonene (≥ 95.0%, CAS Number 138-86-3) was acquired from Sigma-Aldrich (Chile). These materials were utilized in their analytical grade without any further purification.

2.2.2. Thermogravimetric analysis (TGA)

The thermogravimetric analysis of waste tires, and individual polymers (NR, BR, SBR) was performed in a thermobalance (Netzsch, model STA 409 PC). In a typical experiment, about 30 mg of the sample was heated between 20 °C and 650 °C at 10 $K \cdot min^{-1}$ under flowing nitrogen (50 $mL \cdot min^{-1}$). The resulting TG curves and their derivatives were used to elucidate major thermal events taking place during the analysis.

2.2.3. Fast pyrolysis experiments (Py-GC-MS)

Fast pyrolysis experiments were performed in a micropyrolysis system (CDS 5200 Pyroprobe, CDS Analytical, USA). The reactor was a quartz tube (25 mm long and 1.9 mm inner diameter) inserted into a probe and electrically heated by a Pt coil. In typical experiment, 0.5 ± 0.1 mg of polymer or MTWT were placed in the reactor and supported with quartz wool. The heating rate of filament for the experiments was fixed to 20000 $°C \cdot s^{-1}$, while the solid residence time during

pyrolysis was 20 s. In the reaction zone, a flow of He (99.996% purity) was maintained at 1 mL/min to drive the pyrolysis vapors into the analytical zone (GC/MS). Before entering the GC, the volatiles passed through a Tenax trap (Perkin Elmer pre-column) at 280 °C and a heated transfer line (CDS Analytical) set at 280 °C and connected to the gas chromatograph. The separation system consisted of an Elite 1701 column (30 m ×0.25 mm ×0.25 μm) and He as the carrier gas at 1 $mL \cdot min^{-1}$. The GC column was heated from 45 to 280 °C at 2.5 $°C \cdot min^{-1}$. The compounds were identified by their mass spectra in the m/z range of 30-600 Da. The MS spectra obtained were compared with the standard spectra of the compounds in the NIST library. Moreover, area-related selectivity criterion (Eq. 2.1) was applied to estimate product distribution in all the Py-GC-MS experiments.

$$S_i = \frac{\text{Area}_i}{\sum_{i=1}^{n} \text{Area}_i} \tag{2.1}$$

2.2.4. Proposal of a reaction map and kinetic modelling

The product distribution obtained from fast pyrolysis of MTWT and that from the natural and synthetic rubbers, was assessed to propose a comprehensive reaction map describing limonene formation. Then, the proposed reaction map was validated by considering experimental observations and previous reports from the literature [16,21,45,49,80,81]. Thereafter, kinetic measurements of NR (model of MTWT) at different solid residence times (2 – 40 s) and at three temperatures (400°C, 450°C and 500°C) were carried out. The measurements were performed following the same procedures as described in section 2.2.3.

Before the kinetic study, we confirmed the absence of heat transfer limitations by calculating dimensionless numbers such as Py^{I}, Py^{II}, and Biot (Bi) [45,82]. These pyrolysis numbers (Py^{I} and Py^{II}) describe the connection between the reaction kinetics for solid degradation and heat transfer, including both conduction and convection (Eqs. 2.2 and 2.3). Meanwhile, the Biot number correlates intra-particle heat transfer through conduction to that of external heat transfer via convection (Eq. 2.4).

$$\text{Py}^{I} = \frac{\lambda}{\rho \cdot C_p \cdot L^2 \cdot k} \tag{2.2}$$

$$\text{Py}^{II} = \frac{h}{\rho \cdot C_p \cdot L \cdot k} \tag{2.3}$$

$$\mathrm{Bi} = \frac{h \cdot L}{\lambda} \tag{2.4}$$

there, ρ is natural rubber density $[\mathrm{kg \cdot m^{-3}}]$, C_p specific heat capacity of natural rubber $[\mathrm{J \cdot kg^{-1} \cdot K^{-1}}]$, L is the length characteristic (considering sphere $L = r_p/6$) [m], λ is thermal conductivity of natural rubber $[\mathrm{W \cdot m^{-1} \cdot K^{-1}}]$, h is heat transfer coefficient $[\mathrm{W \cdot m^{-2} \cdot K^{-1}}]$, k is reaction rate constant of solid degradation in pyrolysis $[\mathrm{s^{-1}}]$, and r_p is radius of the spherical particles of natural rubber. These physicochemical properties are provided in Table A-2.2. The calculation and results of the dimensionless numbers is detailed in the Chapter 2 appendix, where the conditions for a kinetically controlled regime are informed (Tables A-2.1 – A-2.4 and Figure A-2.2).

The kinetic model for limonene formation from NR pyrolysis was performed under the following assumptions: (i) The Py-GC-MS system is modeled as a constant volume isothermal batch reactor, and (ii) The high heating rate minimizes a heating time delay, which allows considering that the reaction starts when the pyrolysis temperature is reached. Furthermore, the quantification of limonene was performed using standard calibration curves, following the method reported by Klemetsrud et al. [83]. Four calibration curves were constructed for different concentration ranges $[\mu\mathrm{mol \cdot 10^{-4}}]$ with correlation coefficients in the range of 0.981 and 0.999 (See Table A-2.5 and Figures A-2.3 – A-2.6).

The rate constants (k_i) involved in all the reaction steps were modeled by the Arrhenius equation (Eq. 2.5) where E_{ai} and A_i correspond to the activation energy and the pre-exponential factor of the i-th elementary reaction step, respectively.

$$k_i = A_i \cdot \exp\left(-\frac{Ea_i}{R \cdot T}\right) \tag{2.5}$$

The fitting of the rate constants for the multi-step model was performed using a code written in Python. The *scipy* package was used along with *solve_ivp* to solve the system of equations obtained from the molar balances of each compound. Then, the mean squared error (Eq. 2.6, MSE) between the experimental moles of limonene (measured by GC at specific residence times) and those predicted by the model (Eq. 2.6), were minimized to obtain the kinetic parameters (A_i and Ea_i).

$$\mathrm{MSE} = \sum_{i}^{n} \frac{\left(N_{\mathrm{L,exp}}(t_i) - N_{\mathrm{L,mod}}(t_i)\right)^2}{n - j} \tag{2.6}$$

where $N_{\mathrm{L,exp}}(t)$ is the experimental moles of limonene, $N_{\mathrm{L,mod}}(t))$ is the moles of limonene predicted by the model, *n* corresponds to the number of data points recorded for each temperature, and *j* the number of rate constants to be fitted.

Furthermore, the reliability of the kinetic model was confirmed by examining the time-depending degradation patterns of the solid. The NR content in the reactor was measured using an ultra-microbalance (Perkin Elmer AD 6000) both before and after pyrolysis. To standardize the NR mass measurements, the proportion of NR that was not converted was determined using Eq. 2.7 and considering char content to be negligible. Here $m_{\mathrm{NR}}\,(0)$ is the initial mass loaded into the reactor $m_{\mathrm{NR}}\,(t)$ is the mass measured after a reaction or pyrolysis time *t*. This equation was also used to record the moles predicted by the kinetic model (N_{NR}).

$$1 - X(t) = \frac{m_{\mathrm{NR}}(t)}{m_{\mathrm{NR}}(0)} = \frac{N_{\mathrm{NR}}(t)}{N_{\mathrm{NR}}(0)} \tag{2.7}$$

In addition, to study the limonene content with respect to the converted mass of solid for each reaction time at different temperatures, we used the concept of yield (Y_{L}), which is defined by the Eq. 2.8.

$$Y_{\mathrm{L}}(t) = \frac{m_{\mathrm{L}}(t)}{m_{\mathrm{vol}}(t)} = \frac{m_{\mathrm{L}}(t)}{m_{\mathrm{NR}}(0) - m_{\mathrm{NR}}(t)} = \frac{m_{\mathrm{L}}(t)}{X(t) \cdot m_{\mathrm{NR}}(0)} \tag{2.8}$$

where $m_{\mathrm{L}}(t)$ is the mass of limonene calculated for each pyrolysis time, $m_{\mathrm{vol}}(t)$ is the mass of volatiles generated for each pyrolysis time, and $X(t)$ is the degree of degradation of the solid.

2.3. Results and discussion

2.3.1. Thermal characterization of waste tires and individual polymers

Figure 2.1 displays the thermogravimetric analysis (TGA) and derivative thermogravimetry (DTG) curves for MTWT, NR, BR, and SBR. The TG profile indicates that both NR and MTWT undergo thermal degradation between 250 °C and 480 °C. Furthermore, the DTG curves of these materials exhibit a decomposition peak with a maximum at 380 °C, followed by a shoulder-like secondary

peak centered around 430 °C. The former is linked to the devolatilization process of natural rubber and typically corresponds to the production of limonene and isoprene [81], while the latter is associated to secondary degradation processes from the converted solid, such as cyclization, aromatization and cracking reactions [21,43,80]. The main distinction between NR and MTWT is in the mass that remains after complete conversion. NR has a residual mass of 3%, but MTWT has a significantly higher residual mass of 38%, which is explained by the presence of carbon fixed, and ashes formed from additives and the recovered carbon black (See Table A-2.1 for further details). Although there is a quantitative difference between NR and MTWT TG profiles, both exhibit comparable TG degradation trends, suggesting that mining tires include a significant proportion of natural rubber and, furthermore, that the other constituents don't appear to affect the degradation of natural rubber. This notion is validated in the subsequent sections by an examination of the pyrolytic behavior of these materials.

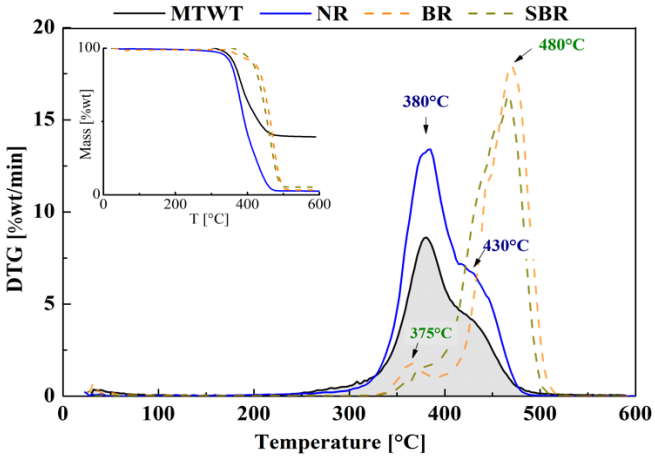

Figure 2.1. Thermal characterization of MTWT, NR, SBR and BR. Thermogravimetric analysis were performed with 30 mg of sample at 10 K/min under flowing nitrogen of 50 mL/min. The inset figure shows the mass as a function of temperature.

The BR and SBR polymers experience thermal degradation within the temperature range of 330 °C to 500 °C. They exhibit two distinct peaks in their derivative thermogravimetric curves, with one small peak centered at 375 ºC and a second, large peak at 480 °C. According to literature, the first peak is attributed to an initial breakdown of the polymeric structure by the fragmentation of C-C bonds, which is then followed by the depolymerization of the BR and SBR (2nd peak). This behaviour aligns with reported TG experiments conducted for waste tires from light duty vehicles,

which have larger proportions of BR and SBR [38,44,80]. Iwarere et al. [80] performed TG experiments with waste automobile and truck tires at different heating rates. The results indicated that at a heating rate of 10 °C·min^{-1}, the TG profile of automobile tires showed two peaks (at 380°C and 470°C), with the highest proportion at the higher temperature. This was attributed to a higher BR and SBR content in this type of tire.

Based on TG data, we have determined that MTWT are mainly composed of natural rubber. Consequently, natural rubber can serve as an appropriate model to describe the thermal degradation of MTWT.

2.3.2. Analysis of limonene production by MTWT pyrolysis

Preliminary Py-GC-MS analyses were conducted on MTWT and specific polymers (NR, BR or SBR) to examine the products distribution and determine the most significant limonene precursors. The pyrolysis temperature was set to 450°C, inspired by previous publications on limonene production in the pyrolysis of waste tires [16,49].

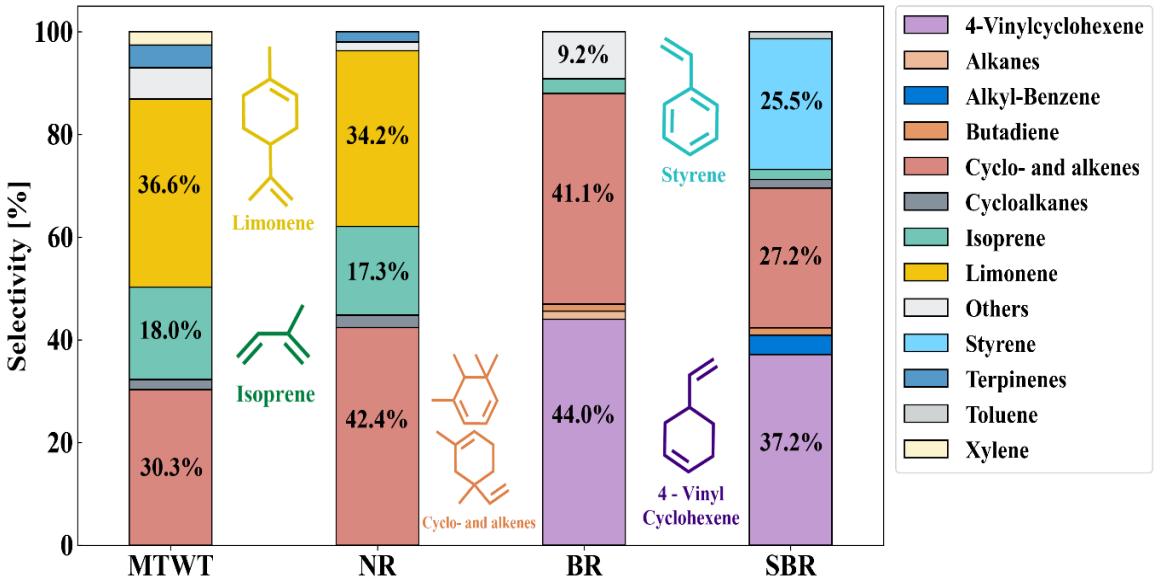

Figure 2.2. Distribution of vapor-phase products from the pyrolysis of MTWT, NR, BR, and SBR. These experiments were performed with 0.5 ± 0.1 mg of sample at 450°C under a helium flow rate of 1 mL/min.

The main compounds generated after MTWT and NR pyrolysis are limonene, (cyclo-)alkenes and isoprene with average selectivities of (35.5%), (36%) and (17.5%), respectively. A similar trend in product distribution from MTWT and NR, is in line with our observations during TG experiments, and is ascribed to the high proportion of NR in the MTWT (>70%). On the other hand, the pyrolysis of the synthetic rubbers (BR and SBR) leads to a different products distribution being the 4-vinyl-cyclohexene, and the cyclic- and linear alkenes the most abundant compounds. Remarkably, the conversion of SBR also produced styrene as a major compound (25.5 wt.%). The Py-GC-MS results confirmed that NR is precursor of limonene while SBR and BR do not lead to detectable quantities of this compound, which confirm previous observations of our group [16,42,45,84]. Accordingly, NR is considered an appropriate solid model to describe limonene formation from MTWT pyrolysis.

The compounds shown in Figure 2.2 provide a static picture of the reaction map presented in Figure 1.2. However, a time-dependent study would provide quantitative data on limonene production during MTWT pyrolysis, providing valuable kinetic information on the actual chemical processes taking place.

Figure 2.3 displays the time-dependent profiles for limonene yield (defined in Eq. 2.8) at pyrolysis temperatures between 400 and 500 ºC. From Fig. 2.3 it is evident that the yield of limonene increases as residence time and temperature rise, which is ascribed to an increment in the NR depolymerization. However, the raising of the temperature also produce a variation in the temporal pattern of limonene yields, being linear at 400 ºC and steeply transformed into a parabolic-like curve at 500 ºC. A maximum yield at 500 °C was observed at 30 s, consistent with that reported in other papers on limonene formation from waste tires in the temperature range studied [21,39,81].

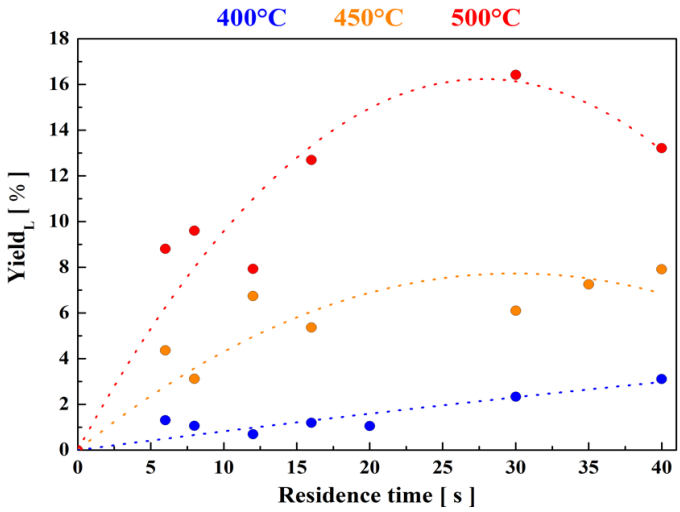

Figure 2.3. Limonene yield as a function of solid residence time at 400, 450 and 500 ºC measured in a Py-GC-MS system. Experiments performed with 0.5 mg of NR. Trend (dash line to guide the eye) and experimental data (dots).

The decrease in the steepness of the trend curves for Y_L after 30 seconds is due to the start of secondary reactions (such as isomerization and dehydrogenation) that result in the production of alkenes and cyclo alkenes at the expense of limonene (See Figure A-2.8). This observation supports the reaction steps outlined in Table 2.1 and aligns with observations of Fig. 2.2, where alkenes and cycloalkenes are shown to be the most prevalent compounds in the pyrolytic vapor at 450 °C. Moreover, this behaviour demonstrates that limonene is an intermediary in the reaction mechanism which is relevant to unravel the kinetic behaviour of NR transformation during MTWT pyrolysis.

2.3.3. Kinetic modeling analysis

The formation of limonene from the pyrolysis of natural rubber (NR) can be conceptualized through a series of elementary reaction steps, which have been proposed based on mechanisms reported in the literature (Figure 1.2).

Table 2.1. Reaction steps and mole balance equations describing limonene formation from natural rubber pyrolysis.

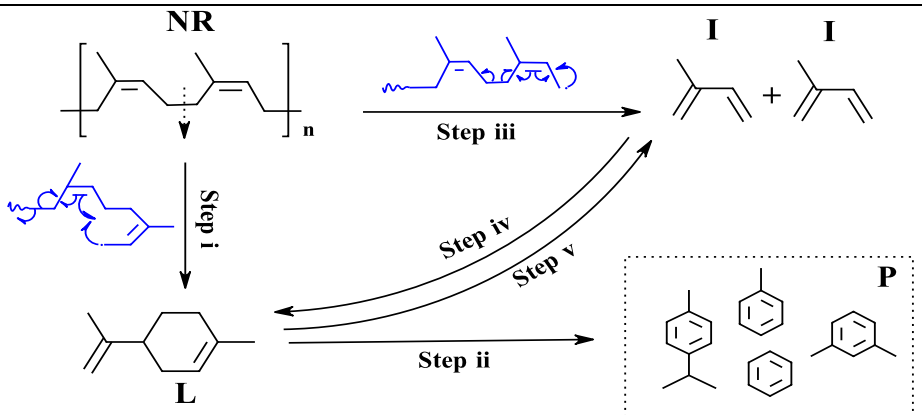

Reaction Steps		Mole balances	
$NR \xrightarrow{k_1} L$	(i)	$\frac{dN_{NR}}{dt} = -k_1 \cdot N_{NR} - k_3 \cdot N_{NR}$	(2.9)
$L \xrightarrow{k_2} P$	(ii)	$\frac{dN_L}{dt} = k_1 \cdot N_{NR} - k_2 \cdot N_L + k_4 \cdot N_I^2$	(2.10)
$NR \xrightarrow{k_3} 2I$	(iii)	$\frac{dN_I}{dt} = k_3 \cdot N_{NR} - k_4 \cdot N_I^2 + k_5 \cdot N_L$	(2.11)
$2I \xrightarrow{k_4} L$	(iv)		
$L \xrightarrow{k_5} 2I$	(v)		

The reaction initiates with the degradation of natural rubber, producing reactive intermediates that subsequently undergo intramolecular cyclization to form limonene (Step i); thereafter, (Step ii) limonene is converted into a hydrocarbon pool (P). Parallelly, the natural rubber undergoes unzipping and C-C breakdown to form two isoprene monomers (Step iii), which could form limonene by an equilibrated Diels-Alder reaction (Steps iv and v). For kinetic modelling, these pathways have been synthesized into five principal reaction steps involving natural rubber, limonene, isoprene, and aromatics as the primary species (Table 2.1). Additionally, in modelling this reaction scheme, the pyrolyzer was treated as a batch reactor, with the solid residence time considered equivalent to the reaction time. The mass balance equations for limonene, isoprene, and natural rubber (solid) are outlined in Equations 2.9 to 2.11.

The kinetic model successfully fitted the experimental data measured for limonene production as confirmed by the calculated mean squared errors (MSE) of $5.54 \cdot 10^{-6}$, $3.02 \cdot 10^{-4}$, $1.01 \cdot 10^{-3}$, at 400 °C, 450 °C and 500 °C, respectively.

Figure 2.4a shows a parity plot between the measured moles of limonene and those modeled from the mass balances using the kinetic model described in Table 2.1. The model predicts the production of limonene (N_L) with an average error of 20% and with an average r^2 of 0.98. This result is considered reasonably good considering that micropyrolysis itself is a technique implying experimental errors and because the highest variabilities were found at high residence times.

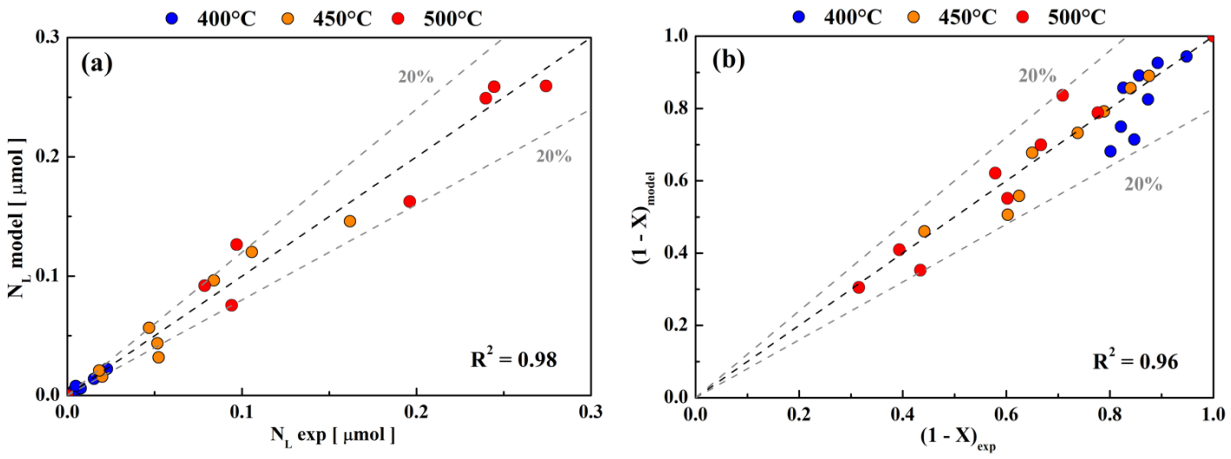

Figure 2.4. (a) Parity plot moles of limonene experimental and modelled. (b) Parity plot of unreacted fraction NR experimental and modelled.

Moreover, the model's robustness was assessed to determine its ability to accurately describe solid conversion. This was accomplished by comparing the measured mass fraction of unreacted NR with the mass fraction predicted by the Model 1, namely during Steps i and iii (Fig. 2.4b). Since the minimization of the target function was made based on the moles of limonene generated, proper prediction of NR conversion is considered as an indirect corroboration of the model's robustness. The parity plots for the unreacted fraction of NR and limonene production confirm the model's robustness to provide a holistic understanding for coupling solid depolymerization with the synthesis of limonene.

The Fig. 2.5a shows the moles of limonene generated after NR pyrolysis along with the trend curves derived from the kinetic modelling of reaction steps (i) to (v) in Table 2.1, using Eqs. 2.9 – 2.11. The increment in the moles of limonene generated with rising temperature aligns with the degradation, driven by the primary scission reactions of polyisoprene depolymerization, while the shape of the curves at $T > 400$ ºC suggest its participation in secondary reactions (See Table A-2.6 and Figure A-2.8).

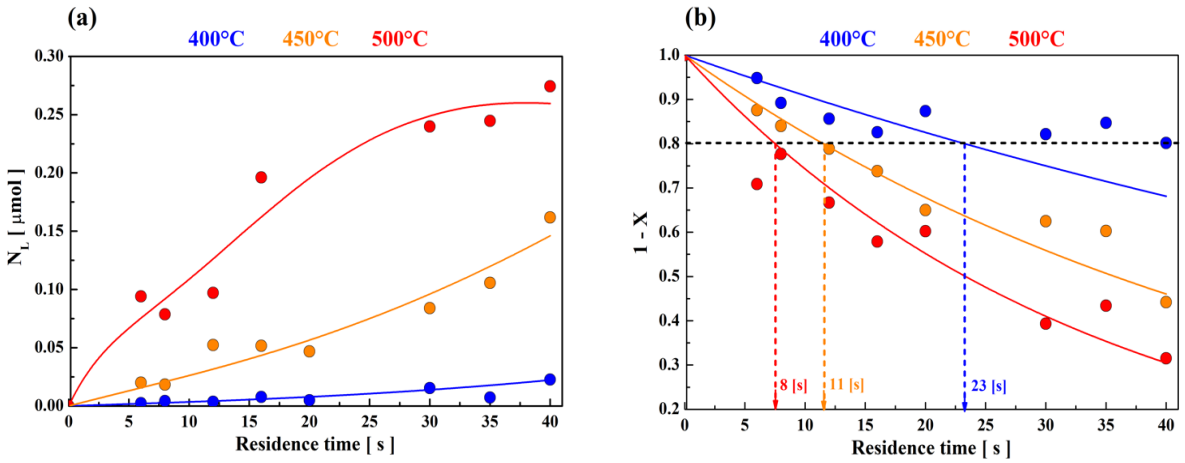

Figure 2.5. (a) Comparison of kinetic Model 1 defined in Table 2.1 (lines) and experimental data (symbols) for moles of limonene as a function of solid residence time at different temperatures. (b) Comparison of unreacted fraction NR predicted by kinetic Model 1 defined in Table 2.1 (lines) and experimental data (symbols) as a function of solid residence time at different temperatures.

Figure 2.5b shows the behavior of the unconverted fraction of NR (Eq. 2.7) measured as a function of temperature and solid residence time and that predicted from the kinetic modeling of steps (i), (ii), (iv) and (v). At first glance, Figure 2.5b indicates that the model exhibits greater limitations at 400 °C as the solid residence time increases. This behavior will be further discussed as the individual reaction steps and results are analyzed in detail.

Moreover, the correlation of Figs. 2.5a and 2.5b allows inferring the relationship between limonene production and NR conversion (primary reactions). Therefore, they represent a complementary understanding of MTWT degradation and volatile´s formation during pyrolysis. For example, at 400 °C and t < 30 s, the unconverted fraction of NR (1-*X*) is >85% while the limonene production (N_L) results in a linear response. This implies that secondary reactions do not affect the process at lower conversions, which is corroborated by the poor yield of aromatics (cymene, benzene, and toluene), cycloalkenes and alkenes reported under these conditions (See Figure A-2.8).

On the other hand, at 500°C and t > 30 s, the NR conversion increased dramatically (X = 61%), while the limonene production rate stopped its linear behavior, implying that secondary processes began to take precedence under this operating condition. However, from Fig. 2.5a and 2.5b it is possible to conclude that limonene is not only formed from the degradation of the solid, but that

there is a parallel reaction occurring at higher temperatures. This can be analyzed by considering a constant unreacted fraction for the three temperatures in Fig. 2.5b. For example, if an unreacted fraction of 80% is considered, this corresponds to times of 23 s, 12 s and 8 s for 400 °C, 450 °C and 500 °C, respectively. Observing the moles of limonene produced at these times for each temperature, it is observed that despite having the same solid conversion, limonene produced increases with temperature (500 °C > 450 °C > 400 °C) (See Table A-2.7). This fact is consistent with reaction steps (iii) and (iv) in which the isoprene formed from NR allows the formation of limonene.

Table 2.2. Kinetic model fitting parameters for the moles of limonene generated by NR pyrolysis.

Step	A_i	Ea_i **[kJ/mol]**	r^2 $[-]^*$
(i)	$9.26 \cdot 10^9$	179.5	0.99
(ii)	$9.07 \cdot 10^{18}$	300.6	0.84
(iii)	8.41	37.63	0.93
(iv)	$1.67 \cdot 10^{10}$	173.6	0.88
(v)	$2.22 \cdot 10^{19}$	304.1	0.93

* r^2 correspond to fit Arrhenius equation.

The values of the rate constants for this model and the Arrhenius plots are provided in Table A-2.8 and Figure A-2.9, respectively.

Table 2.2 shows positive values for activation energies and the correlation coefficients (r^2) of the Arrhenius plots were between 0.84 – 0.99, for all the rate constants, suggesting a physicochemical consistency of *Ea* from kinetic point of view. The lowest values of the activation energies indicate that the step (iii) (degradation of NR to isoprene) and step (iv) (formation of limonene from isoprene) are the most feasible reaction steps leading to limonene formation. Moreover, the predicted values for Ea_1 and Ea_3 are in the same order as those previously reported for describing the kinetic behavior of solid conversion during the pyrolysis of waste tires [21,39,45,74,80]. Such results confirm the capacity of Model 1 to describe the NR conversion and limonene production during fast pyrolysis. On the other hand, the higher activation energies observed for secondary reactions (steps ii and v) suggest that these reactions will be strongly favored at high temperatures.

This behavior is consistent with the inflection point observed at 500 °C, However, major divergences of the model were found at high solid residence times (t >30 s) which coincide with the limitations of the model to predict the behavior of secondary and higher-order reaction products [83]. Moreover, the Ea_2 and Ea_4 fit shows a $r^2 < 0.9$ and a lower degree of fit for the conversion of the solid at 400 °C and $t > 20$ s.

Analyzing the activation energies for steps (iv) and (v), since Ea_5 is significantly higher than Ea_4, it can be concluded that this reaction is most likely far from equilibrium. This suggests that, under pyrolysis conditions, the reaction mainly favors the formation of limonene from two isoprene monomers. According to the above discussion, we have then discarded step (v) from the mechanism, i.e., the Diels-Alder reaction to form limonene from isoprene is irreversible.

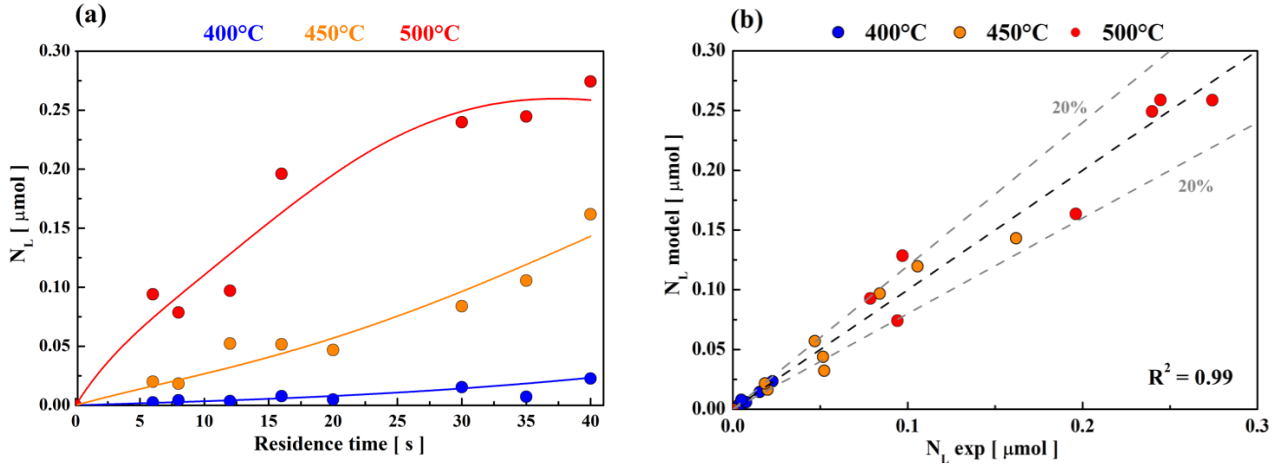

Figure 2.6. (a) Comparison of kinetic Model 2 (lines) and experimental data (dots) for moles of limonene as a function of solid residence time at different temperatures. (b) Parity plot moles of limonene experimental and modeled.

After running the simulation excluding step (v) from the kinetic model (Fig. 2.6a and 2.6b), the mean squared errors were $4.11 \cdot 10^{-6}$, $2.6 \cdot 10^{-4}$, $7.9 \cdot 10^{-4}$ for 400 °C, 450 °C, and 500 °C, respectively. These results show that there is a slight improvement in the mathematical prediction as compared to the previous model, which is also confirmed by the values of r^2 (0.99).

Although, no significant improvements are observed in the prediction of the synthesis of limonene by considering the irreversibility in the Diels-Alder reaction, the modeling of the solid conversion was drastically improved (Fig. 2.7a and 2.7b). The results now lead to a higher correlation factor 0.97 and to an improvement of the prediction capacity for temperatures of 450 °C and 500 °C, and

t > 30 s. Despite both models being able to predict the experimental data of the unreacted fraction of NR with similar accuracy, when the Diels-Alder reaction towards limonene formation is irreversible, Model 2 reduced the overestimation of the limonene conversion by secondary reactions.

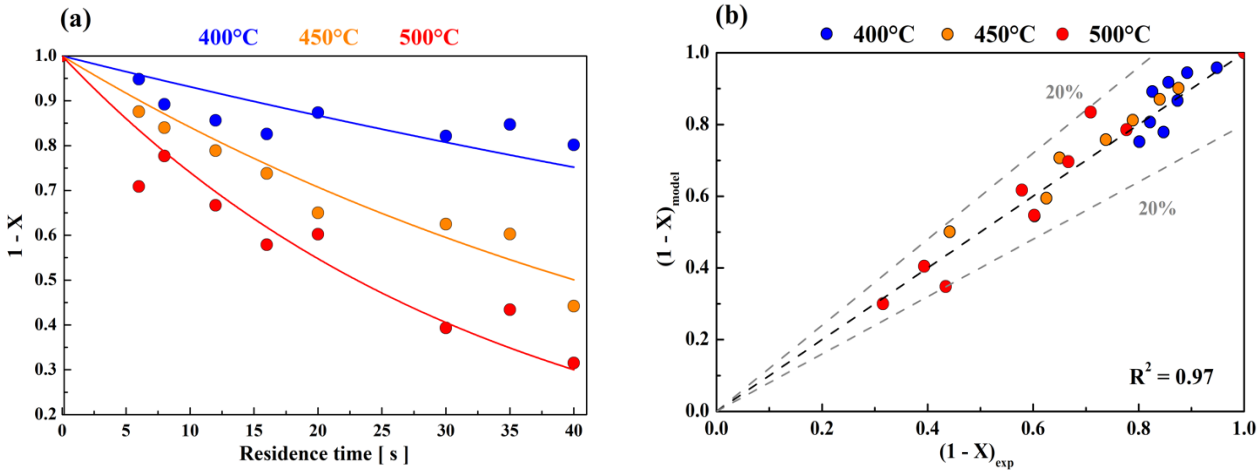

Figure 2.7. (a) Comparison of unreacted fraction NR of kinetic Model 2 (lines) and experimental data (dots) as a function of solid residence time at different temperatures. (b) Parity plot of unreacted fraction NR experimental and modeled.

The values of the rate constants and the Arrhenius plots for Model 2 are provided in Table A-2.9 and Figure A-2.10.

The calculated activation energies under this modelling condition yields values of the same order as those previously discussed for steps (i) to step (iv). This also indicates that step (v) can be considered obsolete in Model 1.

Table 2.3. Kinetic model fitting parameters for the moles of limonene generated by NR pyrolysis discarding the reversibility of the Diels-Alder reaction (step v).

Step	A_i	Ea_i [kJ/mol]	r^2 [−]*
(i)	$2.20 \cdot 10^9$	171.2	1.00
(ii)	$1.06 \cdot 10^{14}$	218.8	0.94
(iii)	$1.03 \cdot 10^2$	53.34	0.97
(iv)	$3.06 \cdot 10^6$	120.2	0.98

* r^2 correspond to fit Arrhenius equation.

Model 2 shows better correlation coefficients (r^2) from the Arrhenius plots than Model 1 (0.94 – 1.0). However, the trend of calculated activation energies is analogous to the Model 1, with the step with the lowest energy barrier for the conversion of NR into two isoprene monomers (step iii). In fact, the computed activation energy for this stage is in the same order of magnitude as that previously estimated (53.3 kJ·mol^{-1}). Furthermore, the computed activation energy for step (ii) (218.8 kJ·mol^{-1}) suggests that the production of aromatics and other hydrocarbons from limonene is hindered at $T < 500$ °C. This finding is consistent with previous literature reporting the product distribution from waste tire pyrolysis [38,39,44,45]. The irreversibility of the Diels-Alder reaction was also observed in the work of Osorio-Vargas et al. [49]. They performed fast pyrolysis of limonene at 400 °C and analyzed the products generated by GC-MS. The main compounds detected in the pyrolysis vapor were limonene, cymene, and p-cymenene with 76.6%, 13.8%, and 6.1%, respectively, and the presence of isoprene was not reported. Those results confirm that limonene does not convert back to isoprene at low temperatures (400 °C), and furthermore, the side reaction of limonene (step ii) has a high energy barrier (Table 2.3), which would explain the higher presence of unreacted limonene in the pyrolysis vapor as temperature decreases. Also, third kinetic modelling approach was also inspected without considering step (iv), i.e. the irreversible Diels-Alder reaction from limonene to isoprene (step (v)) (not shown). However, the rate constants of this Model 3 did not follow the behavior of the Arrhenius equation, thus this model was discarded (Table A-2.10 and Table A-2.11).

2.4. Conclusions

The kinetics for the formation of limonene in the fast pyrolysis of mining truck waste tires was investigated and modeled, focusing on natural rubber (NR) as the primary precursor. NR pyrolysis was explained by a multi-step mechanism which is well-interpreted by power law kinetics. The NR degradation has the lowest activation energy (53.34 kJ·mol^{-1}) while the conversion of limonene into tertiary products was energetically hindered (218.8 kJ·mol^{-1}). These findings indicate that maximizing limonene selectivity in the pyrolytic vapor requires fine-tuning of operating conditions and/or the use of catalytic materials. The model is primarily tailored to NR-rich matrices such as MTWTs, which may limit its applicability to more heterogeneous tire formulations with higher BR/SBR contents. Moreover, it focuses on the main reaction pathways, potentially overlooking

interactions between limonene and co-evolving volatiles, as well as side reactions (e.g., cyclization and aromatization) that can become significant under different operating regimes.

Building on this baseline, the next chapter applies the kinetic framework in a tandem configuration (Py-GC/MS coupled to a downstream catalytic microreactor) to upgrade pyrolytic limonene toward selective cymene formation over Pd/Lewis bifunctional catalysts from a mechanistic point of view.

Chapter 3. Mechanistic approach to the transformation of pyrolytic limonene over bifunctional Pd/TiO_2-ZrO_2 catalysts.

Chapter reproduced from Poblete et al. (2025). Submitted to Chemical Engineering Journal.

This chapter addresses Objectives II and III of the doctoral thesis by studying the catalytic upgrading of pyrolytic limonene into cymene over Lewis-acid supports (TiO_2, ZrO_2–TiO_2) and Pd/Lewis bifunctional catalysts.

This research explores the mechanistic role played by bifunctional catalysts (Pd/TiO2–ZrO2) in the conversion of limonene to cymene. Supported-Pd(1 wt.%) catalysts exhibit different densities of weak acid sites (quantified as Weak Lewis/Total Acid Sites), arranged in the following order: TiO_2 < Pd/TiO_2 < ZrO_2–TiO_2 < Pd/ZrO_2–TiO_2. A two-stage microreactor configuration facilitated sequential pyrolysis of natural rubber (model compound of mining truck tires) and ex-situ catalytic upgrading. The reaction products were analyzed through Py-GC-MS/FID system. The limonene conversion reaction occurs through three competing pathways: (1) isomerization of limonene followed by dehydrogenation of terpinenes to cymene; (2) direct dehydrogenation of limonene to p-cymenene; and (3) side reactions that produce alkenes and cycloalkenes. A Langmuir-Hinshelwood kinetic model, which includes competitive adsorption of limonene and pyrolysis byproducts, suggests that the dehydrogenation of terpinenes and the initial hydrogen abstraction of limonene are the kinetically relevant steps for routes (1) and (2), respectively. This study represents a novel approach that combines the mechanistic exploration with kinetic modeling of the catalytic conversion of limonene to cymene from pyrolytic vapors, providing important insights for the enhancement of waste-derived hydrocarbons.

3.1. Introduction

Mining trucks are equipped with massive off the road (OTR) tires, typically 2–4 m in diameter and weighing over 3 tons, with relatively short lifespans. These tires represent not only a significant operational expense but also a growing source of solid waste in the mining industry. Due to their poor biodegradability and inadequate disposal, they pose severe environmental risks such as

leachate contamination of soils and water bodies and fire hazards [85]. This challenge is particularly critical in Chile, where mining activity is intensive and approximately 49,000 tons of mining truck waste tires (MTWT) are generated annually, accounting for about 35% of the country's total waste tires [4]. According to the Chilean Recycling Industry Association (ANIR), by 2022 only 13.1% of these tires were treated through conventional methods such as shredding, retreading, or energy recovery, while the destination of the majority remained uncertain [86]. To address this, Chile's Extended Producer Responsibility Law (Law 20.920/2016) mandates 100% recycling of MTWT by 2030, fostering the development of advanced valorization routes such as pyrolysis, which is already being deployed at industrial scale [11,12].

Pyrolysis converts MTWT into recovered carbon black, pyrolytic gas, and pyrolytic oils. Pyrolytic oils are especially attractive not only as a potential fuel but also as a source of engineering additives, solvents and chemical building blocks [14,62]. Notably, when these oils are produced from mining tires, they contain substantial amounts of limonene; a biodegradable terpene with broad industrial use and potential as a platform molecule [21,39,87]. Among its derivatives, cymene is particularly valuable for applications in fragrances, pharmaceuticals, solvents, and as a precursor for terephthalic acid. Compared with petrochemical routes (e.g., Friedel–Crafts alkylation of benzene), the limonene-to-cymene pathway offers a greener and more selective alternative [88]. This scenario has led to increasing interest in catalytic strategies for limonene upgrading.

Several authors have demonstrated the feasibility of limonene-to-cymene conversion over heterogeneous catalysts such as zeolites, clays, and metal oxides, under various conditions [89]. Tavera-Ruiz et al. [60], investigated the catalytic reforming of waste tire pyrolysis vapors in a fixed-bed reactor using heteropolyacids supported on silica. They showed that catalysts richer in Lewis sites (Mo- and V-based HPAs) favored cymene formation, while Brønsted-rich systems (W-based HPAs) mainly promoted cracking and gas formation, highlighting the role of acid site type in controlling limonene conversion. Building on this, Osorio-Vargas and co-workers carried out a series of catalytic fast pyrolysis studies of waste tires using micropyrolysis coupled with mass spectrometry (Py–GC–MS) at temperatures between 400 – 500 °C. They first demonstrated that Pd sites selectively promoted the formation of aromatics such as cymene, as compared to other metal nanoparticles like Ni or Co catalysts, which led primarily to cracking products [42]. Later, they examined Pd supported on halloysite nanotubes, where Pd located inside the lumen (gibbsite-like surface Al–OH) increased acidity and doubled cymene selectivity relative to Pd supported

outside (on siloxane-like surface Si–O–Si), evidencing a synergy between support acidity and Pd^0 sites in limonene isomerization–dehydrogenation [16]. More recently, they compared tungstophosphoric acid supported on CeO_2, SiO_2, and TiO_2, showing that catalysts dominated by weak Lewis sites (e.g., 1%TPA/TiO_2) favored cymene formation, whereas stronger Brønsted acidity promoted C–C scission to BTX [25]. While these works linked acidity and metals to product selectivity, they mainly relied on global trends and simplified kinetic models, leaving the mechanistic roles of Lewis sites and Pd unresolved.

More recently, Wu et al. [52] and Zhang et al. [28] employed tandem micro-reactor systems to simulate continuous pyrolysis–catalysis of waste tires operation. They reported cymene selectivities up to 79% and nearly 100%, respectively, when using limonene as a model compound. However, performance dropped with real pyrolytic vapors, revealing the complexity of competing reactions and the limits of model-compound approaches.

According to the previous reports, catalysts that combines Lewis's acidity with Pd dehydrogenating capacity are particularly attractive for promoting the limonene-to-cymene reactions. In this sense, mixed ZrO_2–TiO_2 oxides are very attractive supports, as the dispersion of Zr over TiO_2 modulates both the density and the strength of Lewis acid sites, as predicted by Tanabe's model [56], while simultaneously providing a stable anchoring sites for the uniform dispersion of Pd nanoparticles [54].

Although previous catalytic pyrolysis studies have highlighted the potential of acid and Pd-based catalysts for producing cymene from waste tire pyrolysis, they often rely on generalized kinetic models. This simplification has led to limited understanding on the reaction mechanisms involved, and on the roles of Pd and acid sites. Therefore, this study provides a novel approach to the kinetic understanding of the catalytic transformation of pyrolytic limonene into cymene over Pd supported on mixed oxides. To that aim natural rubber (NR) is used as a representative solid model of mining truck tires to generate limonene-rich pyrolytic vapors, which are subsequently upgraded over a catalytic bed placed in an ex-situ tandem reactor. The reaction performance is correlated with the acid properties of the catalysts, and the role of Pd sites is also elucidated. Moreover, the activity data is interpreted through a Langmuir–Hinshelwood kinetic model, describing three reaction routes for limonene transformation into aromatics, cymene and other competing species.

3.2. Material and methods

3.2.1. Feedstock and chemical agents

Polyisoprene (NR, CAS 104389-31-3) was acquired at its analytical degree (molecular weight of 38000 g/mol) and used for characterizations and pyrolysis without further treatment. Moreover, *D,L*-limonene (≥95.0%), *p*-cymene (99%, CAS 99-87-6), absolute ethanol (C_2H_6O, CAS 64-17-5), $PdCl_2$ (>99% purity, CAS-7647-10-1), Triethanolamine (TEA (≥99.0%, CAS 102-71-6), and zirconium butoxide (CAS 1071-76-7) were acquired from Sigma-Aldrich (Chile). In addition, the titanium oxide (anatase, CAS 1317-70-0) used as catalyst support was purchased from Fisher Scientific®.

3.2.2. Catalysts synthesis and characterization

A series of TiO_2-based supports containing 0.5-15 wt.% Zr were synthetized to evaluate the influence of zirconia loading on acidity and catalytic performance. The supports ZrO_2–TiO_2 were synthesized via wet impregnation of TiO_2 with (x)·Zr (x = 0.5, 3, 7, 10, and 15% wt). Zirconium butoxide was added to a beaker containing 50 mL of ethanol, and the mixture was stirred using ultrasound for 5 minutes to ensure proper homogenization. Then, pre-dried TiO_2 was sieved at particle sizes between 125–210 µm and added to the flask; thereafter the suspension was stirred again for another minute. The resulting mixture was then placed in a rotary evaporator at 100 rpm and 40 °C until complete solvent evaporation. The recovered solid was dried in an oven (Lab Tech, LDO-150F) at 50 °C for 24 hours and subsequently calcined in flowing air (50 $mL \cdot min^{-1}$) at 500 °C for 2 hours (heating rate of 2 $°C \cdot min^{-1}$) to obtain the mixed oxide support, hereafter referred to as ZrO_2–TiO_2.

The catalytic screening of supports was performed in the same micro-pyrolysis system described in Chapter 2, using an ex-situ configuration in which the natural rubber (NR) sample (0.5 mg) and the catalyst (5 mg) were separated by a plug of quartz wool inside the reactor (catalyst/NR mass ratio = 10). All screening experiments were conducted at 400 °C with a solid residence time of 30 s. These conditions were selected based on the kinetic model developed in Chapter 2 to ensure that the primary product in the vapor phase is pyrolytic limonene. Maintaining a limonene-rich vapor stream allows a consistent assessment of the intrinsic activity of the supports toward cymene formation under identical vapor–solid contact conditions.

Finally, 1 wt.% Pd was incorporated onto both TiO_2 and ZrO_2–TiO_2 supports via incipient wetness impregnation, using appropriate volumes (determined from N_2 adsorption at 77 K on supports) of a $PdCl_2$ solution adjusted to pH ~1.5. Triethanolamine (TEA) was used to promote a uniform metal distribution on the supports, following the procedure described by Soled et al [90]. Subsequently, the materials underwent calcination at 500 °C for 4 hours to eliminate any remaining TEA and to facilitate the formation of oxidized palladium species. The resulting solids were then treated in a U-shaped quartz reactor (6 mm inner diameter) under a continuous hydrogen flow (40 $mL \cdot min^{-1}$), at 2 $°C \cdot min^{-1}$ until 400 °C with a dwell time of 2 hours to ensure complete reduction of the palladium oxide.

X-ray diffraction (XRD) analysis of the ZrO_2–TiO_2 was conducted in a Bruker D4 Endeavor diffractometer equipped with Cu Kα radiation (λ = 0.154 nm), operating at 40 kV and 20 mA. Data were collected over a 2θ range of 3–90°, with a step size of 0.02 s^{-1}. The crystalline structure was identified through a search-match procedure utilizing the HighScore Plus software and the Crystallography Open Database.

Bulk surface acidity was analyzed via ammonia temperature-programmed desorption (NH_3-TPD) in a Micromeritics 3Flex analyzer equipped with a thermal conductivity detector (TCD) and coupled to a Pfeiffer Vacuum OmniStar GSD 320 mass spectrometer. In a typical analysis 100 mg of sample (catalyst or support) were heated under flowing He (100 $mL \cdot min^{-1}$) by heating to 350 °C at a rate of 20 $°C \cdot min^{-1}$ and holding for 30 minutes to remove physiosorbed species. Thereafter, the sample was cooldown to 100 °C, and ammonia was introduced via 0.5 cm^3 pulses at 10-minute intervals until saturation. Following NH_3 saturation, the system was purged with helium at 100 $mL \cdot min^{-1}$ for 30 minutes at 100 °C to remove weakly adsorbed ammonia and stabilize the baseline. Subsequently, the temperature was increased to 500 °C at a rate of 10 $°C \cdot min^{-1}$. Desorbed species, including NH_3, H_2O, and N_2, were monitored using the mass spectrometer by tracking their respective m/z fragments: 16, 18, and 28. Because m/z = 28 may also arise from CO, m/z =14 (N^*) was additionally recorded to confirm assignment to N_2. The desorption profiles and acid site densities were normalized per gram of catalyst. The deconvolution of the TCD signal was performed considering the mass signal m/z = 16, as the representative of ammonia, thus avoiding possible interferences from adsorbed species resulting from NH_3 decomposition at high temperatures [91,92]. Acid site strength was classified based on the temperature of desorption: weak acid sites were assigned to peaks appearing below 200 °C, medium-strength sites were

defined within the range of 200–400 °C, and strong acid sites were considered those desorbing above 400 °C [93,94].

The nature of the surface acid sites was studied through Fourier-transform infrared spectroscopy with pyridine (IR-Pyridine). The measurements were carried out in a flow cell equipped with CaF_2 windows placed in a Nicolet iS10 spectrometer (ThermoScientific) equipped with a DTGS detector which was operated at 32 scans and 4 cm^{-1} resolution. For each experiment, samples were pressed into self-supported pellets (13 mm diameter, approximately 10 mg) which underwent thermal treatment under vacuum (Pfeiffer HiCube Eco Turbo) at 400 °C for 12 hours to remove physiosorbed species. Then the system temperature was reduced to 150 °C, and a reference spectrum was recorded. Subsequently, pyridine vapor was introduced into the cell allowing adsorption until saturation. Thereafter, sequential desorption was conducted at 150, 250, and 300 °C, each following a 30 min equilibration period, to assess the strength and stability of Brønsted and Lewis acid sites. For FTIR-derived weak-to-total ratios (W/TS_{IR}), the characteristics Lewis band at 1605 cm^{-1} was deconvoluted; W/TS_{IR} was computed as $(A_{150°C} - A_{250°C})/A_{150°C}$. *(*For cross-technique comparison, W/TS values from TPD and FTIR were normalized to each technique's maximum; the secondary y-axis in Figure 3.4b spans 0–1.)

The textural properties of catalysts and supports were investigated through N_2 adsorption–desorption isotherms measured at 77 K, utilizing a Gemini VII Surface Area Analyzer (Micromeritics). Prior to measurements, samples were degassed at 200 °C for 4 hours to eliminate adsorbed impurities. Specific surface areas were calculated using the Brunauer–Emmett–Teller (BET) method. Pore volume of the supports used for incipient wetness impregnation synthesis was also determined from this analysis.

The average Pd particle size was estimated by CO pulse chemisorption, assuming a stoichiometry of CO/Pd = 1.5. This value reflects a mixture of linear (1:1) and bridged (1:2) adsorption modes of CO on Pd and is recommended in the British Standard [95,96]. The analysis was carried out using CHEMBET 3000 analyzer equipped with a thermal conductivity detector (TCD). Approximately 100 mg of catalyst was loaded into a U-shaped quartz sample tube and pretreated under flow of N_2 (30 $mL \cdot min^{-1}$) at 200 °C for 1 hour. After this step, the sample was cooled to room temperature, and the gas was switched to 10% H_2/Ar. The catalysts were then reduced at 400 °C for 1 hour. Upon completion of the reduction, N_2 flow was resumed while cooling the sample to room temperature. Subsequently, CO pulses (5% CO/He) of 50 µL were injected every 2 minutes until a

constant TCD signal was achieved, indicating surface saturation. The amount of CO adsorbed in the support was considered negligible and the CO adsorption volume was used to calculate the metal dispersion (D (%)) and estimate the mean particle diameter (d_p) using the following equations [97]:

$$D\ (\%) = \frac{V_{ads} \cdot K \cdot M}{V_m \cdot W_s \cdot C} \cdot 100\% \qquad (3.1)$$

$$d_p\ (nm) = \frac{6 \cdot A \cdot M}{\rho \cdot D \cdot N} \cdot 10^9 \qquad (3.2)$$

here, V_{ads} is the CO adsorption volume cm^3, and K is the stoichiometry factor which was equal 1.5 in this case. *M* is atomic weight of Pd (106.4 $g \cdot mol^{-1}$), V_m is molar volume of adsorbed gas (22,400 $cm^3 \cdot mol^{-1}$), W_s is the sample mass (g), and C represented the percentage content of Pd (%). A is the surface atom density of Pd (1.27×10^{19} atoms$\cdot m^{-2}$), ρ is bulk density of Pd (12.02×10^6 $g \cdot m^{-3}$) and N is Avogadro's number (6.02×10^{23} mol^{-1}).

Additionally, scanning transmission electron microscopy coupled with energy-dispersive X-ray spectroscopy (STEM–EDX) was performed simultaneously for structural and chemical analysis, using a JEOL JEM-2010 TEM (200 kV) equipped with an Oxford Instruments XMax 80 detector, to assess Pd dispersion and elemental distribution (Ti, Zr, Pd).

3.2.3. Kinetic modeling of the catalytic conversion of pyrolytic limonene into cymene

Pyrolysis experiments: Fast micro-pyrolysis experiments, both with and without catalysts, were conducted using a tandem micro-reactor system (Rx-3050TR, Frontier Laboratories Ltd., Japan). This system has two reactors connected in series: the first reactor (Reactor 1) performs the pyrolysis of the natural rubber in a stainless-steel reaction cup (80 µL), while the second reactor (Reactor 2) enables catalytic reactions in a tubular fixed bed (ID: 3 mm; L: 78 mm), as illustrated in Figure 3.1. The experiments were conducted in two modes:

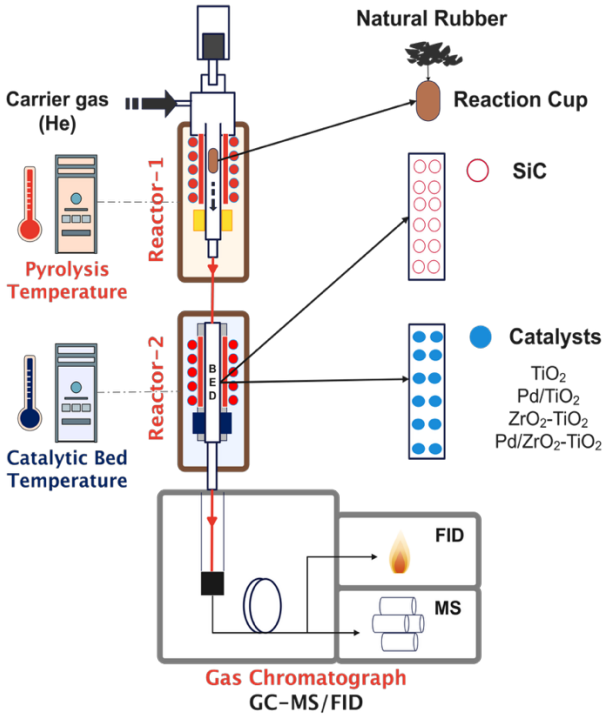

Figure 3.1. Scheme of experimental setup for coupled pyrolysis and ex-situ catalytic conversion of pyrolytic vapors (Py-GC-MS/FID).

(i) Non-catalytic pyrolysis: These experiments were carried out to produce specific concentrations of limonene in the pyrolysis vapors by controlling the reaction conditions in the first reactor. This is a *sine qua non* condition to perform reliable kinetic analysis for catalytic limonene conversion. In a typical experiment, specific quantities of natural rubber (230 – 300 mg) were placed in the reaction cup and then were subjected to pyrolysis at different temperatures (350 – 500 ºC), using flowing He (50 mL·min^{-1}) as the carrier gas. The pyrolysis products then passed through the second reactor (filled with an inert SiC bed) and were subsequently analyzed using the chromatographic system. The possibility of transforming limonene during the pass of the pyrolytic vapors through the secondary reactor, was discarded by recording and comparing the pyrograms at the inlet and outlet of Reactor 2. The mass of natural rubber, the reaction temperature, and solid residence time in Reactor 1 were adjusted using the kinetic modeling approach described in Chapter 2 to achieve the desired concentration of pyrolytic limonene [87].

(ii) Catalytic pyrolysis: The catalytic experiments were performed under ex situ mode. The operation of Reactor 1 was the same as previously described for non-catalytic experiments, while

the second reactor was loaded with catalytic material (TiO_2, ZrO_2–TiO_2, Pd/TiO_2 and Pd/ZrO_2–TiO_2). The temperature in the catalytic bed (300 – 500 ºC) was controlled independently to the first reactor. Residence time of pyrolytic limonene (τ) was adjusted by varying the limonene feed from Reactor 1, ranging from 0 to 9 s. In complementary tests, the catalyst mass was varied (1.1–8.3 mg) to probe intermediate formation along the fixed bed**.**

Products identification and quantification: The pyrolysis vapors generated during non-catalytic and catalytic experiments were separated using gas chromatography (Trace GC Ultra) equipped with a Restek Rtx-1701 capillary column (60 m × 0.25 mm ID × 0.25 µm film thickness) and analyzed with a mass spectrometer (ISQ MS) and a flame ionization detector (FID), both from Thermo Fisher Scientific. Gas flow and column pressure were regulated by a high-pressure flow controller (HP-3050F, Frontier Laboratories Ltd.), maintaining the micro-pyrolyzer pressure at 0.4 MPa and the column head pressure at 0.14 MPa. High-purity helium (99.999%, Air Liquide, Belgium) was used as the carrier gas at a flow rate of 50 mL·min^{-1} for each experiment. The GC injector temperature was set at 280 °C with a split ratio of 1:50. The mass spectrometer's transfer line was maintained at 280 °C, the ion source at 250 °C, and electron ionization was performed at 70 eV, scanning m/z 29–300. The carrier gas and volatiles were split approximately equally between the MS and FID detectors via a three-way splitter. The FID operated at 250 °C with an ignition threshold of 0.5 pA. Product identification was based on retention times, manual inspection of MS fragmentation patterns, and comparison with the NIST mass spectral library (version 2.3). Quantification of target products such as limonene and cymene were carried out with the FID detector, by using calibration curves (See Figure A-3.1) [29]. The other pyrolysis products were quantified based on their effective carbon number (ECN) as outlined in the supplementary material (Table A-3.1) [98].

Reaction performance metrics

To quantitatively evaluate the performance of the catalytic pyrolysis system, three key metrics were defined: pyrolysis product yield, limonene conversion, and reaction rate. These parameters enable the assessment of both the pyrolysis behavior and the catalytic effects.

$$Y_{p,i} = \frac{m_i}{m_{NR}} \cdot 100 \qquad (3.3)$$

$$X_i = \frac{m_{i,gen} - m_{i,out}}{m_{i,gen}} \qquad (3.4)$$

$$r_i = \frac{n_i}{W} \quad (3.5)$$

$$\tau = W/\dot{m}_{L,in} \quad (3.6)$$

$Y_{p,i}$ (%) is the yield of compound i (isoprene, limonene, and cycloalkenes & alkenes); limonene was quantified by external calibration, whereas isoprene, cycloalkenes, and alkenes were estimated using the ECN method. m_{NR} (µg) is the mass of Natural Rubber fed into the pyrolysis reactor (Reactor 1). X_i (a.u.) is the net conversion of compound i during the catalytic step; $m_{i,gen}$(µg) is the mass of compound i generated from pyrolysis of Natural Rubber (µg) predicted by the kinetic model validated in our previous work [87], and $m_{i,out}$ (µg) is the mass of compound i at the outlet of the catalytic reactor (i.e., the unconverted mass). Positive values of X_i indicate net consumption; negative values indicate net formation. r_i is the rate of formation of compound i after catalytic conversion of limonene ($mol \cdot s^{-1} \cdot mgcat^{-1}$), n_i denotes the moles of the compound i, and W is the mass of the catalyst loaded into the reactor (mg). τ (s) is the residence time, defined with the inlet mass flow of limonene to Reactor 2, $\dot{m}_{L,in}$ ($ug \cdot s^{-1}$).

Kinetic interpretations of reaction data

The kinetic interpretation of the catalytic transformation of pyrolytic limonene into cymene was performed using the packed bed reactor model (PBR), neglecting pressure drop, and expansion effects due to the dominance of the inert carrier gas:

$$\frac{W}{F_{L_0}} = \int_0^{X_L} \frac{dX}{(-r_L)} \quad (3.7)$$

where W corresponds to the mass of catalyst (mg) in the catalytic bed, F_{L_0} ($\mu mol \cdot s^{-1}$) is the inlet molar flow of limonene to Reactor 2, predicted from Reactor 1 operating conditions (temperature and natural rubber mass) using the validated NR-pyrolysis kinetic model from our previous work [87]. The reaction rate of limonene consumption per mass of catalyst ($-r_L$) was described using a Langmuir–Hinshelwood-type expression that accounts for competitive adsorption among surface species, as will be further elaborated in the next sections.

The experiments were performed at different W/F_{L_0} values and at three different temperatures (300, 400, and 500 °C). The kinetic parameters were fitted by minimizing the objective function (OF) defined in Eq. 3.8.

$$OF = \frac{\sum_{i=1}^{n}\left[\left(\frac{W}{F_{L0}}\right)_{mod,i} - \left(\frac{W}{F_{L0}}\right)_{exp,i}\right]^2}{n-j} \quad (3.8)$$

where n denotes the number of experimental data and j represents the number of fitted parameters. To compare the predictive performance of different kinetic models, the mean absolute percentage error (MAPE, %) was employed, as defined in Eq. 3.9:

$$MAPE = \sum_{i=1}^{n} \frac{\left|\left(\frac{W}{F_{L0}}\right)_{exp,i} - \left(\frac{W}{F_{L0}}\right)_{mod,i}\right|}{\left(\frac{W}{F_{L0}}\right)_{exp,i}} \cdot 100 \quad (3.9)$$

Finally, the physicochemical consistency of the fitted model, was confirmed by the inspecting following criteria: (i) adsorption processes must be exothermic ($\Delta H_{ads} < 0$), (ii) the surface reaction must present a positive activation energy ($E_a > 0$); (iii) the fitted parameters were checked against the guideline proposed in the literature [99]: $0 < -\Delta S_{ads} \lesssim 12.2 - 0.0014 \cdot \Delta H_{ads}$ ($cal \cdot mol^{-1}$).

Although this section focuses on the general kinetics of limonene conversion, the Langmuir–Hinshelwood framework also provides the basis for describing product selectivity. This is particularly relevant for cymene, which constitutes the key compound in this study. Therefore, a mechanism-oriented kinetic formulation and validation for limonene conversion into cymene over Pd/ZrO_2-TiO_2 is presented in the results and discussion section.

3.3. Results and discussion

3.3.1. Support characterization and screening

Before starting the study on the catalytic upgrading of pyrolytic vapors, a preliminary screening of catalyst supports was carried out using TiO_2 and TiO_2 modified with (x)·Zr (x = 0.5, 3, 7, 10, and 15% wt). The objective of this pre-screening was to analyze how the modification of the acidic properties of TiO_2 with ZrO_2 would provide intrinsic activity of mixed support for pyrolytic vapor

transformation. This first approach allows selecting a catalyst support for performing mechanistic elucidations on the bifunctional effects of Pd/ZrO_2-TiO_2.

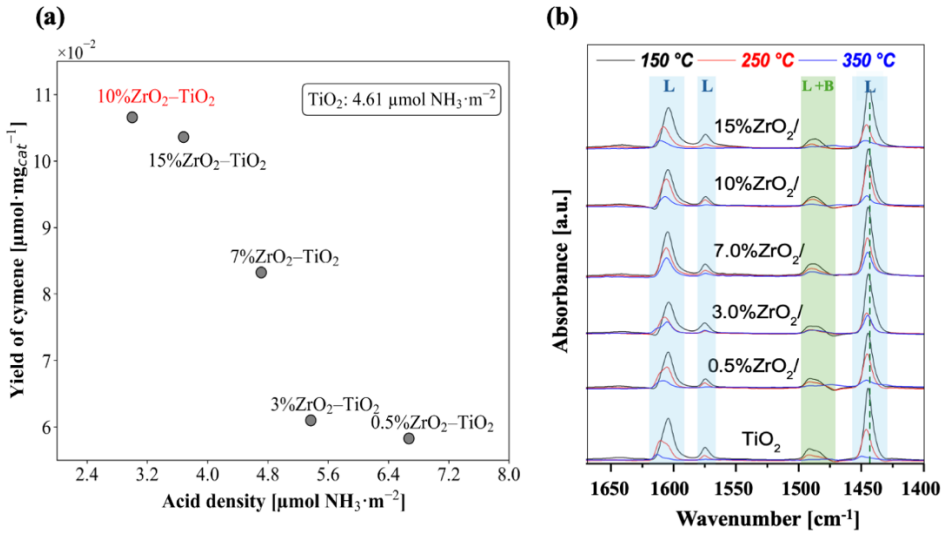

Figure 3.2. (a) Intrinsic cymene yield as a function of acid site density for Zr-modified TiO_2 supports under ex-situ conditions (400 °C, 30 s, catalyst/NR ratio = 10). (b) IR spectra of pyridine adsorbed on the TiO_2-based supports with Zr loadings in the 0.5–15 wt.% range. Band assignments: L = pyridine coordinated to Lewis acid sites; L + B = coexistence of Lewis- and Brønsted-bound pyridine.

Figure 3.2a shows the intrinsic cymene yield obtained over the Zr-modified TiO_2 supports. Notably, there is an increment in the yield to cymene as the support acidity decreases, which could be associated with a lower rate of cracking reactions, usually favored on highly acid supports (Figure A-3.2). Zirconia incorporation clearly alters the acidic properties of TiO_2; increasing Zr loadings is generally associated with higher surface Lewis's acidity [54,56]. This is confirmed by the pyridine-IR spectra in Figure 3.2b, which display only Lewis-related bands, indicating that zirconia affects the density of acid sites without changing their nature. According to these results, in the upcoming sections the mixed oxide containing 10% of Zr is selected as the support for Pd to conduct subsequent catalytic upgrading of waste tire pyrolytic vapors.

3.3.2. Catalyst characterization

Table 3.1 summarizes the textural, metallic and acid properties of the Pd/ZrO_2-TiO_2 catalysts. The incorporation of zirconia on titania caused an increase in surface area of 6 $m^2 \cdot g^{-1}$, while the pore volume decreased by 0.07 $cm^3 \cdot g^{-1}$. The increase in surface area is consistent with the high

dispersion of ZrO_2, which may hinder TiO_2 crystallization and increase surface roughness, despite the deposition of amorphous ZrO_2 onto the TiO_2 surface as confirmed by XRD diffractograms (Figure A-3.3 shows no ZrO_2 peaks) [54,100]. After Pd impregnation, only minor changes in textural parameters were observed (1 – 4 $m^2 \cdot g^{-1}$ increase in surface area), which indicates that Pd nanoparticles did not significantly modify pore structure. This is explained by the fact that Pd was highly dispersed on both supports (≈56% dispersion), corresponding to an average particle size of ~2 nm, as calculated from CO chemisorption. This high dispersion was also qualitatively confirmed by STEM-EDX observations (Figure A-3.4). The N_2 adsorption–desorption isotherms (Figure A-3.5) of all materials are Type IV profiles, characteristic of mesoporous materials, according to the IUPAC classification [101]. TiO_2 and Pd/TiO_2 show H1-type hysteresis loops, associated with uniform mesopores. In contrast, ZrO_2–TiO_2 and Pd/ZrO_2–TiO_2 exhibit H2-type hysteresis, suggesting more complex pore networks, likely due to partial pore blocking by highly dispersed amorphous ZrO_2.

Table 3.1. Physicochemical properties of the catalysts. S_{BET} is the specific surface area, V_p is pore volume, acid density and strength measured by NH_3 thermal desorption.

Catalyst	S_{BET} [$m^2 \cdot g^{-1}$]	V_p [$cm^3 \cdot g^{-1}$]	Pore diameter [nm]	Pd particle size* [nm]	Acid density [$\mu molNH_3 \cdot m^{-2}$]		
					Weak	Medium	Total
TiO_2	34	0.24	28.2	-	1.51	3.10	4.61
ZrO_2-TiO_2	40	0.17	17.0	-	1.11	1.89	3.00
Pd/TiO_2	35	0.13	13.7	1.99	1.66	3.17	4.83
Pd/ZrO_2-TiO_2	44	0.12	10.9	1.98	1.70	2.12	3.82

* Calculated from CO chemisorption.

NH_3-TPD analysis (See Figures A-3.6 – A-3.7) revealed that ZrO_2 incorporation decreased the contribution of both weak and medium-strength acid sites, consistent with the model proposed by Tanabe [56] in which Ti–O–Zr bond formation can modify surface electron density and attenuate acid centers. In both Pd-containing catalysts (Pd/TiO_2 and Pd/ZrO_2–TiO_2), the main desorption bands shifted to lower temperatures, indicating weaker acid strength (Figure A-3.7). This effect

suggests that, beyond the overall decrease in acidity, Pd incorporation also modifies the relative strength of surface sites, likely through TiO_2 surface distortions and/or electronic interactions zero-valence Pd acting as an electron density acceptor, thereby favoring the formation of weaker Lewis's acid sites [102,103]. Furthermore, mass spectrometry coupled to TPD further revealed the formation of N_2 (m/z = 28) and H_2O (m/z = 18) above 250 °C in these catalysts (See Figures A-3.6 and A-3.7), providing additional evidence that Pd can act as a dehydrogenating site through its π-backbonding capacity, weakening the N–H bond and promoting NH_3 decomposition [42,91,104–107]. Because m/z = 28 could also arise from CO, we verified that m/z = 14 (N^*) mirrors the m/z 28 profile; therefore, the 28 signal is assigned N_2.

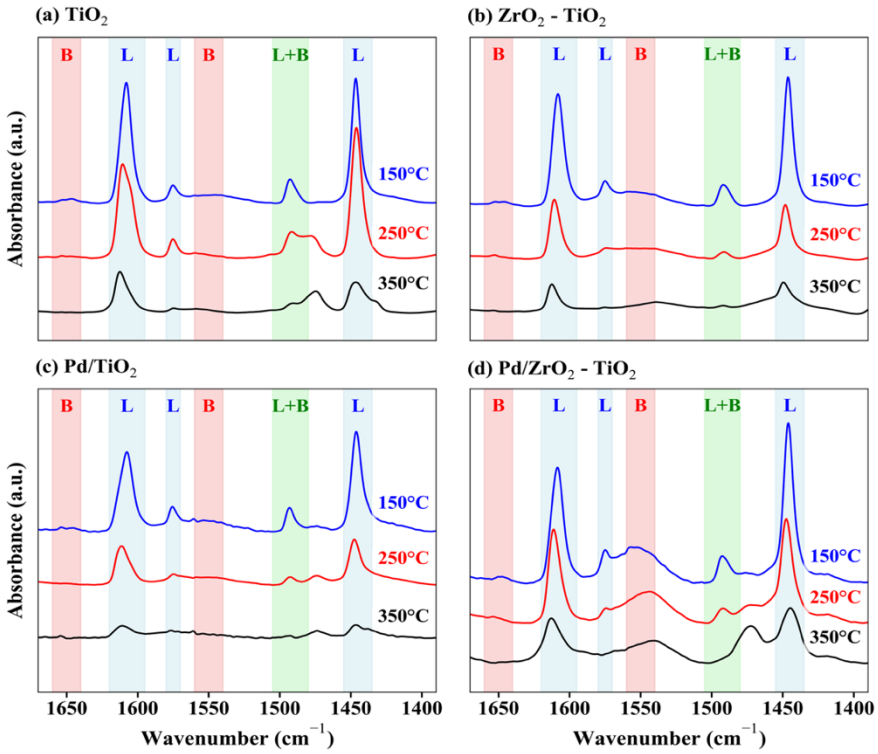

Figure 3.3. IR spectra of pyridine adsorbed on (a) TiO_2, (b) ZrO_2–TiO_2, (c) Pd/TiO_2, and (d) Pd/ZrO_2–TiO_2, after brief outgassing at the indicated temperatures. Band assignments: B = pyridinium ion (Brønsted acid sites); L = pyridine coordinated to Lewis's acid sites; L + B = coexistence of both species.

In Figure 3.3, the IR spectra of adsorbed pyridine for all catalysts show well-defined bands at 1445, 1575, and 1605 cm^{-1}, which are characteristic of pyridine coordinated to Lewis's acid sites. A weaker band at 1490 cm^{-1} is also detected, which is generally assigned to pyridine interacting

simultaneously with Lewis and Brønsted acid sites. However, in the present case, the contribution arises exclusively from pyridine coordinated to Lewis's acid sites. On the other hand, the bands at 1550 and 1650 cm^{-1}, typically associated with pyridine interacting with Brønsted acid sites, are absent in all recorded spectra. The progressive decrease in Lewis band intensity with increasing desorption temperature reflects the predominance of weak-to-medium sites, consistent with NH_3-TPD results. Thus, surface acidity in all catalysts can be ascribed mainly to Lewis centers of variable strength, further modulated by ZrO_2 and Pd incorporation.

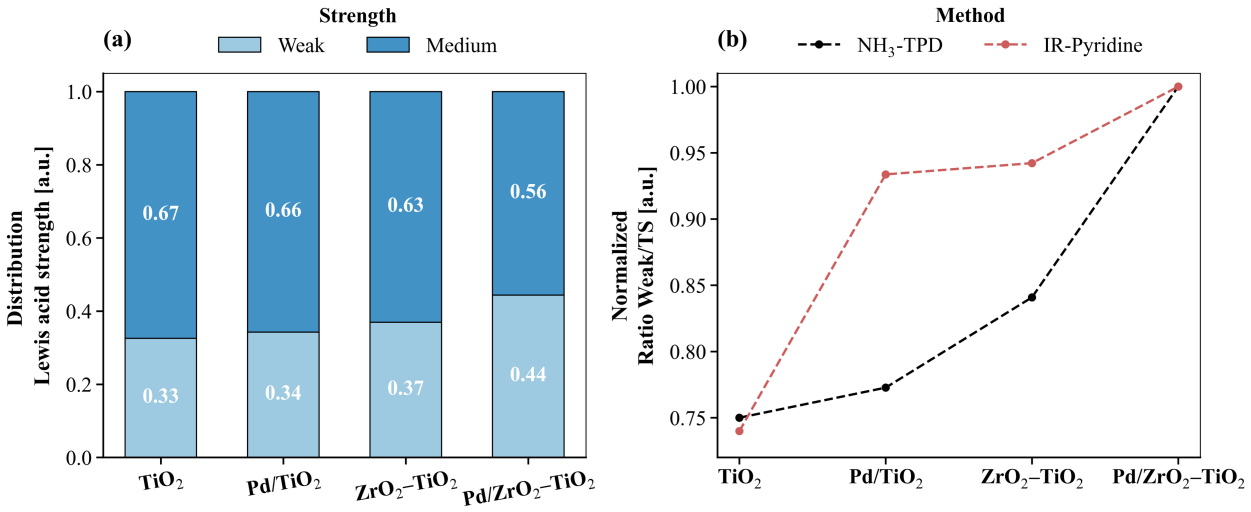

Figure 3.4. (a) Distribution of Lewis acid site strength from NH_3-TPD, showing the fractions of weak and medium sites for each catalyst. (b) Normalized ratio of weak-to-total surface Lewis acid sites (Weak/TS) obtained from NH_3-TPD and IR-pyridine. Both methods confirm enrichment of weak Lewis sites with ZrO_2 and Pd.

The quantitative effect of ZrO_2 and Pd on acidity is summarized in Figure 3.4. Both NH_3-TPD and pyridine-IR analyses revealed a progressive increase in the fraction of weak acid sites relative to the total acidity (Weak/TS), following the sequence TiO_2 < Pd/TiO_2 < ZrO_2–TiO_2 < Pd/ZrO_2–TiO_2. The good agreement between the two techniques (See Figure 3.4b) confirms that catalyst modification systematically enriched the surface in weak Lewis's acid sites, which is particularly relevant for the proposed mechanism of limonene transformation into cymene [25,60].

In summary, textural parameters were very similar among the catalysts, and Pd mean nanoparticle size resulted similar (≈2 nm) on both supports. The main differences arose from surface acidity:

ZrO_2 incorporation reduced total acidity but maintaining Lewis's character, while Pd increased the density and the fraction of weak sites and conferred a more pronounced dehydrogenating character. The Pd/ZrO_2–TiO_2 catalyst exhibited the highest weak-to-total site ratio (W/TS), highlighting the bifunctional synergy expected to govern limonene conversion to cymene. This aligns with literature assigning the double-bond isomerization limonene on Lewis's acid sites (weak), followed by Pd-catalyzed dehydrogenation to cymene [16,49].

3.3.3. Production of pyrolytic limonene from Natural Rubber.

The formation of cymene from natural rubber involves two coupled steps: the pyrolytic generation of limonene and its subsequent catalytic transformation. Since limonene is the precursor of cymene, controlling its production during pyrolysis is critical to ensure its availability for catalytic conversion.

Primary pyrolysis of NR produces a complex mixture of compounds derived from competitive and sequential reactions such as depolymerization, intramolecular cyclization, and cracking (see Figure 1.2). The qualitative analysis of Py-GC-MS data yielded as most abundant products from NR pyrolysis were limonene (85.5–33.0%), isoprene (2.0–47.6%), cycloalkenes (11.3–7.3%) and alkenes (7.4%) regardless the reaction temperature (Figure A-3.8). With increasing temperature, abundance (as area %) decreased, while isoprene, alkenes, and cycloalkenes became more prominent. This shift reduces the limonene available for catalytic conversion and may introduce competitive adsorption effects in the catalytic bed. Interestingly, rather than decreasing linearly, the limonene yield exhibited a maximum at 450 °C. This is consistent with the proposed kinetic model and other previous reports [21,26,41], which indicates the onset of secondary limonene reactions at higher temperatures, leading to the formation of additional cycloalkenes (e.g., Cyclohexene, 1-methyl-5-(1-methylethenyl)-(R)-, 9-(1-Methylethylidene)-bicyclo[6.1.0]nonane, and γ-Elemene) as well as isoprene and monoaromatics such as xylenes and toluene.

To derive these trends and predict limonene availability, the kinetic model developed in the Chapter 2 was applied [87]. The model correlates the limonene concentration with the NR mass and pyrolysis temperature through a series of pseudo-first order Power Laws applied to four elementary reaction steps: (i) NR degradation via intramolecular cyclization to limonene (L), (ii) conversion of limonene into cycloalkenes, alkenes, and aromatics (C), (iii) direct degradation of NR to isoprene monomers (I), and (iv) secondary formation of limonene through a Diels–Alder reaction between two isoprene molecules [87]. The corresponding mole balances are summarized in Table

3.2. The model was evaluated using the kinetic parameters summarized in Table 2.3, which were gathered from previous chapter [87].

Table 3.2. Reaction steps and mole balance equations describing limonene formation from natural rubber pyrolysis considering a batch reactor model, present in the previous Chapter.

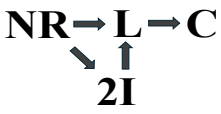

Reaction Steps		Mole balances
$NR \xrightarrow{k_1} L$	(i)	$\frac{dN_{NR}}{dt} = -k_1 \cdot N_{NR} - k_3 \cdot N_{NR}$
$L \xrightarrow{k_2} C$	(ii)	$\frac{dN_{L}}{dt} = k_1 \cdot N_{NR} - k_2 \cdot N_{L} + k_4 \cdot N_{I}^2$
$NR \xrightarrow{k_3} 2I$	(iii)	$\frac{dN_{I}}{dt} = k_3 \cdot N_{NR} - k_4 \cdot N_{I}^2$
$2I \xrightarrow{k_4} L$	(iv)	$\frac{dN_{C}}{dt} = k_2 \cdot N_{L}$

NR: Natural Rubber, **L**: Limonene, **I**: Isoprene, and **C**: Alkenes and cycloalkenes.

One of the major drawbacks in micro-pyrolysis systems is associated with the poor reproducibility of experimental data from one set-up to another. Therefore, the model developed in Chapter 2 (using the CDS Pyroprobe 5200 Analytical Setup) must be validated before its application on the tandem Rx-3050TR Frontier system, which is used for the catalytic tests. To validate the applicability of the kinetic model beyond the calibration data, and to confirm its use for estimating the limonene feed to the catalytic bed, we developed a series of non-catalytic experiments and compared model predictions against independent pyrolysis experiments performed in these two configurations.

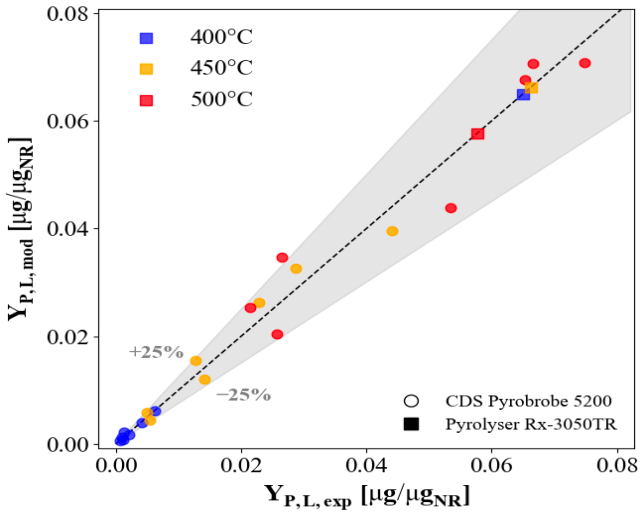

Figure 3.5. Parity plot of modeled vs. experimental limonene yield, $Y_{P,\text{limonene}}$[µg/µg$_{NR}$]. Colors denote temperature (400, 450, 500 °C); markers denote reactor system: ○ CDS Pyroprobe 5200, ■ Pyrolyser Rx-3050TR. Dashed line is $y = x$; shaded band indicates ±25% deviation.

Figure 3.5 shows that the model captures the non-catalytic generation of limonene with errors largely within ±25% across both pyrolysis reactors (Pyroprobe 5200 and Rx-3050TR). This agreement is consistent with the mechanistic model of Chapter 2 and summarized in Table 3.2, validates the model's transferability and supports its use to prescribe $Y_{P,\text{limonene}}$ as the inlet specification to the continuous catalytic bed.

The model reproduced the experimental distribution of limonene, isoprene, and cycloalkenes under isothermal conditions (350–500 °C) at fixed NR mass (~250 µg) in Rx-3050TR, with deviations only at 500 °C where isoprene was slightly overestimated (Figure 3.6). This discrepancy may be attributed to the no-consideration of secondary isoprene reactions, such as Diels–Alder condensations [45,46,108].

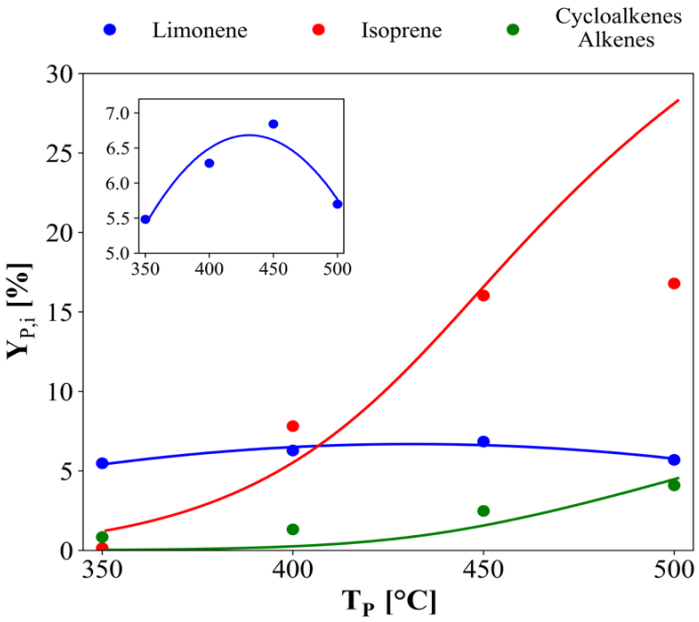

Figure 3.6. Yield of main compounds generated from the pyrolysis of Natural Rubber, relative to the mass of Natural Rubber fed, at different pyrolysis temperatures in Rx-3050TR. Experimental data (points) and kinetic model (line).

In addition, for practical application in catalytic experiments, the modeled limonene yield was correlated to pyrolysis temperature through a polynomial expression (Eq. 3.10, $r^2 = 0.9$), enabling prediction of limonene concentration at the inlet of the catalytic reactor.

$$Y_{P,i}(T_p) = -1.945 \cdot 10^{-6} \cdot T_P^2 + 1.677 \cdot 10^{-3} \cdot T_p - 0.2947 \quad (3.10)$$

Finally, control experiments were conducted between 300 and 500°C using second reactor empty. No additional secondary products or cymene were detected under these conditions, confirming that cymene formation requires specific catalytic active sites and is not formed upon thermochemical reactions only (Figures A-3.9 and A-3.10).

3.3.4. Bifunctional role of Pd/TiO_2-ZrO_2 during the conversion of pyrolytic limonene

Regardless of the catalyst employed, the main compounds generated during the catalytic pyrolysis of pyrolytic limonene were cymenes, cymenene, monoaromatics (e.g., xylenes, and toluene), and isomerized intermediates such as terpinenes and terpinolene (see Figure. A-3.11 for conventional

stacked-bar plots at 300, 400, and 500 °C). These distributions are consistent with previous studies, where noble metals such as Pd or Pt promote dehydrogenation reactions to form monoalkylated aromatics [16,42,109]. Under acidic conditions, cymene and cymenene may undergo further dealkylation to lighter aromatics at ≥500 °C [25,110], and even at 450 °C when Pd is supported on acidic oxides such as TiO_2 [49].

Based on the literature, three main pathways have been proposed for cymene formation from limonene: (i) disproportionation, (ii) hydrogenation/dehydrogenation, and (iii) isomerization to terpinene/terpinolene followed by dehydrogenation [37,109,111]. In the present study, the third pathway is considered predominant, as no menthenes, typical intermediates of the first two pathways, were detected. This interpretation is supported by the acid–metal nature of the catalysts, where Lewis's acid sites favor limonene isomerization to terpinene/terpinolene [25,60], and highly dispersed Pd enables their subsequent dehydrogenation. Two Pd-related dehydrogenation routes can therefore be envisaged: (i) dehydrogenation of terpinene/terpinolene to cymene, which dominates under the studied conditions used in this work, and (ii) partial dehydrogenation of limonene to cymenene, a pathway that may become more relevant at higher temperatures due to the increased participation of Pd's dehydrogenating function [16].

Finally, it is important to consider that, despite the formation of valuable products such as cymene and monoaromatics, limonene can also follow the previously mentioned parallel pathways in the absence of a catalyst, leading to the formation of compounds such as isoprene, alkenes, and cycloalkenes [42,112]. All possible transformation pathways of pyrolytic limonene are summarized in Figure 3.7. To identify which of these pathways are favored under the studied conditions, the following section focuses on the role of surface acidity in directing limonene conversion into cymene.

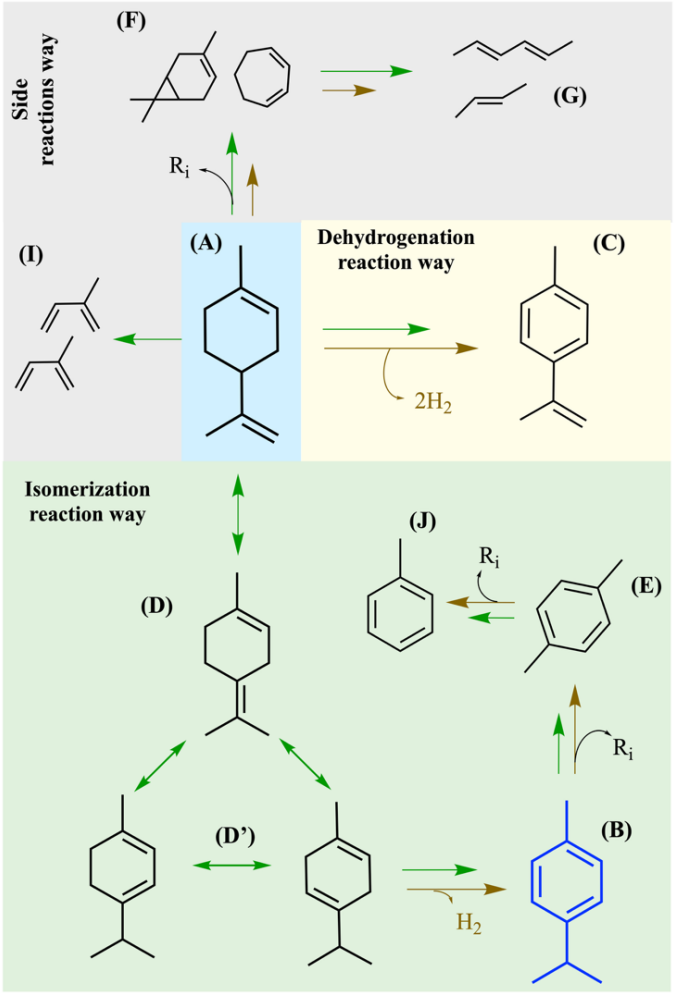

Figure 3.7. Simplified reaction scheme of the transformation of limonene to cymene, showing the predominant reaction pathways and the catalysts that most favor each step. (A) Limonene, (B) Cymene, (C) Cymenene, (D) Terpinolene, (D') Terpinenes, (E) p-Xylene, (J) Toluene, (F) Cycloalkenes, (G) Alkenes, and (I) Isoprene. Green arrow (acids-support), Brown arrow (palladium site).

Catalytic experiments were performed with a constant inlet molar flow of limonene (6.01 µmol/s), generated from NR pyrolysis at 450 °C, and a catalytic bed temperature of 400 °C was selected as a balance between activity and stability. A nominal catalyst loading of W = 5.1 mg (±0.2 mg run-to-run variation) was used for each catalyst studied. All catalysts predominantly exhibited Lewis's acidity, as confirmed by pyridine-IR, with the main differences arising from the strength distribution of these sites. For this reason, the analysis was focused on the proportion of weak-to-total acid sites (W/TS), rather than on the absolute acid site density, since no correlation was observed between limonene reactivity and total acidity (Figure A-3.12).

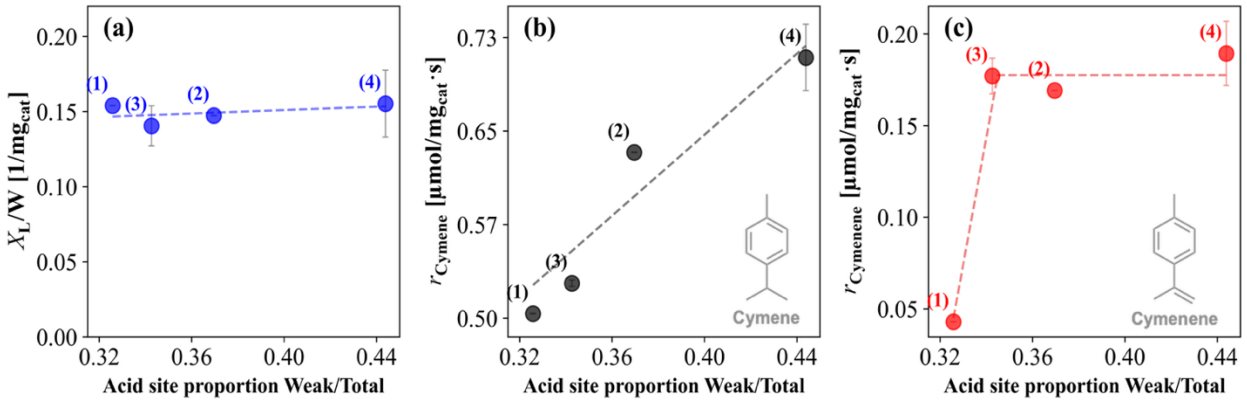

Figure 3.8. Effect of the proportion of weak acid sites (W/TS) on catalytic performance at 400 °C on: (a) Limonene conversion normalized by mass of catalyst; (b) Formation rate of cymene, (c) Formation rate of cymenene. Each x-axis value is the W/TS of a given catalyst, obtained from NH_3-TPD by peak deconvolution for each catalyst. The numbers above each data point correspond to the following catalysts: (1) TiO_2, (2) ZrO_2–TiO_2, (3) Pd/TiO_2, (4) Pd/ZrO_2–TiO_2. Error bars represent standard deviations from duplicate experiments for selected samples. These plots complement the conventional views provided in Figure A-3.11.

Figure 3.8 summarizes the effect of the proportion of weak acid sites (W/TS) on catalytic performance. Limonene conversion (Figure 3.8a) remained nearly constant at 150 mg_{cat}^{-1}, indicating that acid strength distribution does not directly control limonene reactivity but rather product selectivity. The cymene generation rate (Figure 3.8b) increased linearly with W/TS, from 10 to 14.5 µmol·mg_{cat}^{-1}·s^{-1}, consistent with the proposed scheme (Figure 3.7). This suggests that relative abundance of weak Lewis sites (W/TS) promotes the isomerization of limonene to terpinene/terpinolene, which are subsequently dehydrogenated to cymene on metallic Pd sites. A higher surface proportion of weak Lewis sites (higher W/TS) favors double bond migration or proton exchange without excessive stabilization of intermediates, in line with the Sabatier's principle. By contrast, stronger acidity can lead to undesired cracking, as reported for zeolites and other Brønsted-rich oxides [14,60]. Cymenene generation (Figure 3.8c) was 4–10 times lower than cymene, with rates of 3.2–3.7 µmol·mg_{cat}^{-1}·s^{-1}, on Pd- and Zr-containing catalysts and ~1 µmol·mg_{cat}^{-1}·s^{-1}, on TiO_2. This indicates limited direct dehydrogenation of limonene, enhanced only slightly by ZrO_2–TiO_2, and strongly promoted by Pd. The preference for cymene suggests that

limonene adsorption occurs predominantly via the exo-cyclic double bond rather than the ring, facilitating isomerization reaction and subsequent dehydrogenation [16,32,42].

The role of Pd was further isolated by comparing Pd/TiO_2 and TiO_2, which have similar acid site densities (4.83 vs. 4.61 $\mu molNH_3 \cdot m^{-2}$) and W/TS ratios (0.34 vs. 0.33). Differences in selectivity can therefore be attributed to Pd. Additional results (Figure A-3.13) show that while Pd moderately increases cymene formation, it strongly enhances cymenene and monoaromatic yields (xylene, toluene). This behavior indicates that Pd introduces parallel dehydrogenation pathways: (i) from isomerized limonene (terpinene/terpinolene) to cymene which can subsequently convert to aromatics, and (ii) directly from limonene to cymenene. Given its high dispersion, Pd interacts closely with Lewis's acid sites, and its electronic configuration enables π-backbonding interactions that mimic the electron-acceptor character of Lewis centers while conferring a markedly higher dehydrogenation capacity. Thus, instead of two independent functions, the catalyst surface can be regarded as an integrated active ensemble, where acid-like and metallic properties converge to selectively promote the transformation of limonene into cymene. This perspective will serve as the basis for the mechanistic proposal in the following section.

To provide additional evidence for the proposed pathways (Figure 3.7) and to confirm the role of terpinene and terpinolene as intermediates for cymene formation, the evolution of products was studied at different space times $\tau(s)$ over $Pd/ZrO_2–TiO_2$ at 400 °C. For this purpose, the mass of natural rubber (290 μg) and the pyrolysis temperature in Reactor 1 (T_p = 450 °C), were kept constant allowing for a steady limonene mass flow rate ($\dot{m}_{L_0}$) to the catalytic Reactor 2, while the catalyst mass (W) was varied to adjust residence time ($\tau = W/\dot{m}_{L_0}$).

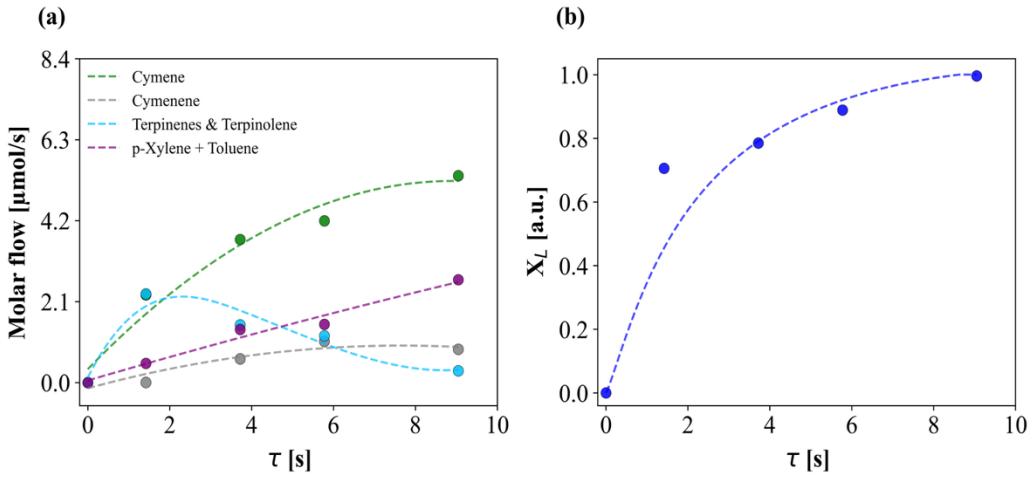

Figure 3.9. (a) Molar flow of the main products: cymene (green), cymenene (grey), terpinenes + terpinolene (magenta), and p-xylene + toluene (cyan); and (b) Limonene conversion (X_L) as a function of residence time (τ) during the catalytic transformation of pyrolytic limonene over $Pd/ZrO_2–TiO_2$ at 400 °C. Dashed curves are trend lines. Residence time: $\tau = W/\dot{m}_{L_0}$ (s), where W is the catalyst mass (g), and $\dot{m}_{L_0}$ the inlet mass flow of limonene ($g \cdot s^{-1}$).

Figure 3.9a shows that terpinene and terpinolene reach a maximum molar flow at intermediate residence times (~2s), followed by a gradual decrease as space time increases. This behavior is characteristic of transient intermediate species that are formed and subsequently consumed in downstream reactions. In parallel, cymene and monoaromatic compounds increase steadily with space time, consistent with their formation through consecutive reactions, particularly Pd-assisted dehydrogenation of limonene isomers. In contrast, cymenene is produced at a much lower rate (ca. six times lower than cymene) and remains nearly constant, reinforcing that the bifunctional catalyst preferentially promotes the acid–metal pathway (isomerization - dehydrogenation) rather than direct limonene dehydrogenation. Figure 3.9b, which shows limonene conversion (X_L) as a function of τ, confirms that the catalytic system remains active throughout the studied interval, reaching conversions close to 100% at 6s. Additionally, the most significant change in conversion occurs during the initial segment (0–2 s), which coincides with the peak formation of terpinene and terpinolene. This suggests that the first step in the transformation of limonene is dominated by an isomerization reaction catalyzed by acid sites.

Finally, to further test the proposed scheme shown in Figure 3.7, the reactivity of other pyrolysis-derived compounds was examined (Figure 3.10). Cycloalkenes exhibited a net conversion of

~50%, indicating strong interaction with the catalyst and likely competition with limonene for adsorption on Lewis's acid sites, due to the presence of double bonds in cyclic structures such as cyclohexene, 1-methyl-5-(1-methylethenyl)-(R). In contrast, both isoprene and alkenes showed negative conversions, demonstrating that they were formed during the catalytic stage. These trends can be explained by limonene degradation to isoprene via retro Diels–Alder-type reactions and by cracking of cycloalkenes into alkenes, processes typically promoted by acid–metal catalysts, respectively [14].

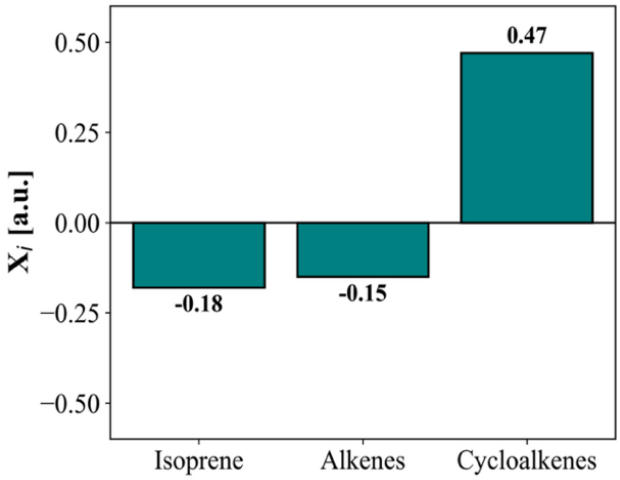

Figure 3.10. Net conversion (X_i) of isoprene, alkenes, and cycloalkenes from the pyrolytic vapors after passing through the Pd/ZrO_2–TiO_2 catalytic bed. Results correspond to a pyrolysis temperature of 450 °C and a catalytic bed temperature of 400 °C. Positive values indicate consumption; negative values indicate formation.

These results highlight once more that (i) terpinene and terpinolene are key intermediates for cymene formation, (ii) cymene is the dominant product due to the bifunctional synergy of Lewis sites and Pd, and (iii) competitive adsorption of cycloalkenes must be considered when developing a kinetic model. This validates the reaction scheme proposed in Figure 3.7 and emphasizes the need to account for side-compound, particularly from cycloalkenes, when interpreting catalytic performance.

3.3.5. Mechanistic interpretation of Limonene-to-Cymene conversion

Based on the proposed reaction scheme (Figure 3.7) and the results discussed above, the following hypotheses were considered for the formulation of a Langmuir–Hinshelwood-type kinetic model describing the catalytic transformation of pyrolytic limonene and the cymene generation:

(1) The pyrolysis vapors stream passing through the fixed-bed catalytic reactor (Reactor 2) consists primarily of limonene (A), along with by-products derived from NR pyrolysis (P), such as isoprene, alkenes, and cycloalkenes, among which cycloalkenes are the only species explicitly treated as competitive adsorbates for active sites.

(2) In the kinetic formulation, only the cycloalkene fraction of P contributes to the competitive adsorption terms, due to their potential adsorption via exposed double bonds on both metallic Pd and Lewis acid sites.

(3) By-products from surface dealkylation reactions are considered undesired compounds.

(4) Desorption of all key products (B = cymene, C = cymenene, D/D′ = terpinolene/terpinenes, E+J = aromatics, F+I = undesired products) is assumed.

(5) The rate-determining step (RDS) for each pathway corresponds to a unimolecular surface reaction.

(6) A single type of active site is considered, representing the bifunctional acid–metal character of the catalyst. Here, (*) denotes a vacant site; for any species i, i^* denotes the adsorbed species.

<u>Adsorption equilibria</u>

Limonene: $A + (*) \overset{K_A}{\rightleftharpoons} A^*$, $\theta_A = K_A \cdot F_A \cdot \theta_*$

Pyrolysis byproducts: $P + (*) \overset{K_P}{\rightleftharpoons} P^*$, $\theta_P = K_P \cdot F_P \cdot \theta_*$

Where θ_i y θ_* are the fractional coverages of species i and vacancies, respectively. K_i is the adsorption equilibrium constant; and F_i is the molar flow rate of species i.

Reaction pathways of limonene transformation

Route 1 – Isomerization/Dehydrogenation to cymene

Isomerization steps

(1.1) Limonene to terpinolene: $A^* \overset{K_1}{\rightleftharpoons} D^*$, $\theta_D = K_1 \cdot \theta_A$

(1.2) Terpinolene to terpinenes: $D^* \overset{K_2}{\rightleftharpoons} D'^*$, $\theta_{D'} = K_2 \cdot \theta_D$

Dehydrogenation steps

(1.3) 1° Dehydrogenation (RDS): $\mathbf{D'^* + (*) \xrightarrow{k_{1,1}} BH^* + H^*}$, $\mathbf{r_{1,1} = k_{1,1} \cdot \theta_{D'} \cdot \theta_*}$

(1.4) 2° Dehydrogenation: $BH^* + (*) \xrightarrow{\mathbf{k_{1,2}}} B^* + H^*$, $r_{1,2} = k_{1,2} \cdot \theta_{BH'} \cdot \theta_*$

Possible secondary routes of adsorbed cymene (B^*):

(1.5) Dealkylation: $B^* + (*) \xrightarrow{\mathbf{k_{1,3}}} E^* + R_i^*$, $r_{1,3} = k_{1,3} \cdot \theta_B \cdot \theta_*$

(1.6) Desorption: $B^* \xrightarrow{\mathbf{k_{1,4}}} B + (*)$, $r_{1,4} = k_{1,4} \cdot \theta_B$

Desorption of by-products and other reactions:

(1.7) Hydrogen desorption: $2H^* \xrightarrow{k_{1,5}} 2(*) + H_2$, $r_{1,5} = k_{1,5} \cdot \theta_H^2$

(1.8) Xylene desorption: $E^* \xrightarrow{k_{1,6}} E + (*)$, $r_{1,6} = k_{1,6} \cdot \theta_E$

(1.9) Toluene formation: $E^* \xrightarrow{k_{1,7}} J^* + R_i^*$, $r_{1,7} = k_{1,7} \cdot \theta_E$

(1.10) Toluene desorption $J^* \xrightarrow{k_{1,8}} J + (*)$, $r_{1,8} = k_{1,8} \cdot \theta_J$

(1.11) By-product dealkylation desorption: $2\,(R_i^* \xrightarrow{k_{1,9}} R_i + (*))$, $r_{1,9} = k_{1,9} \cdot \theta_{R_i}$

Given that the first dehydrogenation of terpinenes was proposed as the rate-determining step (RDS), the rate expression for Route 1 can be written as:

$$(-r_1) = k_{1,1} \cdot \theta_{D'} \cdot \theta_* = k_1 \cdot K_1 \cdot K_2 \cdot K_A \cdot F_A \cdot \theta_*^2$$

In addition to the main pathway (Route 1), the kinetic model includes the other two reaction pathways: direct Pd-assisted dehydrogenation to *p*-cymenene (Route 2) and competitive transformations of limonene into other products such as isoprene and cycloalkenes (Route 3).

Route 2 – Direct Dehydrogenation to cymenene

This pathway proceeds via sequential H-abstraction steps on adsorbed limonene; the first dehydrogenation is the rate-determining step (RDS):

$$A^* + (*) \xrightarrow{k_2} CH_3^* + H^*, \qquad (-r_2) = k_2 \cdot \theta_A \cdot \theta_*$$

Subsequent dehydrogenations and cymenene (C) desorption are detailed in Table A-3.2.

Route 3 – Side reactions to isoprene and cycloalkenes

Generation of isoprene and cycloalkenes from adsorbed limonene is considered as alternative pathways:

$$A^* + (*) \xrightarrow{k_{3,1}} I^* + I^*, \qquad A^* + (*) \xrightarrow{k_{3,2}} F^* + R_i^*, \qquad r_3 = k_3 \cdot \theta_A \cdot \theta_*$$

With full stepwise schemes provided in Table A-3.2.

Considering all three pathways, the overall rate of limonene consumption can be expressed as:

$$(-r_A) = (-r_1) + (-r_2) + (-r_3)$$

$$(-r_A) = (-r_1) \cdot \left(1 + \frac{r_2}{r_1}\right) + (-r_3)$$

where r_2/r_1 represents the formation rate ratio between cymenene and cymene, which varies with the temperature of Reactor 2. Substituting the kinetic expressions, the overall rate becomes:

$$(-r_A) = (k_1 \cdot K_1 \cdot K_2 \cdot K_A \cdot F_A \cdot \Phi(T) + k_3 \cdot K_A \cdot F_A) \cdot \theta_*^2$$

where $\Phi(T) = 1 + r_2/r_1$, and the values calculated for each temperature are reported in Table A-3.3.

The fraction of vacant sites (θ_*) was calculated using two alternative site balance formulations (Table 3.3): (i) including only limonene adsorption, and (ii) including competitive adsorption of pyrolysis by-products. Comparison of these models provides insight into the potential inhibitory effect of pyrolysis by-products on the catalytic transformation of limonene.

Table 3.3. Global rate expressions and parameter mapping for Models I and II describing limonene consumption considering alternative site-balance formulations.

Model	**Rate of limonene, $(-r_A)$**	**Parameter mapping**	**Parameters fitted**
I – Only limonene adsorption	$\frac{\Phi(T) \cdot \alpha \cdot F_A + \beta \cdot F_A}{(1 + K_A \cdot F_A)^2}$	$\alpha = k_1 \cdot K_1 \cdot K_2 \cdot K_A$ $\beta = k_3 \cdot K_A$ $\Phi(T) = 1 + r_2/r_1$	α (T) β (T) K_A
II – Adsorption of limonene and pyrolysis by-products	$\frac{\Phi(T) \cdot \alpha \cdot F_A + \beta \cdot F_A}{(1 + K_A \cdot F_A + K_P \cdot F_P)^2}$		α (T) β (T) K_A K_P

* $\Phi(T)$ in the expressions is obtained from the experimental rate ratio r_2/r_1, (Table A-3.3).

Figure 3.11 compares the parity plots of Model I and Model II at 300, 400, and 500 °C. In both cases, the shaded area indicates a ±25% deviation between experimental and calculated values. Model II shows improved agreement with experimental data across all conditions, particularly at 300 °C. At this temperature, Model I exhibits a mean absolute percentage error (MAPE) of 30.2%, whereas Model II achieves 10.3%. This improvement is attributed to the inclusion of competitive adsorption of pyrolysis by-products generated in Reactor 1. The stronger effect at lower temperature is consistent with the exothermic nature of adsorption processes, which become more relevant at 300 °C.

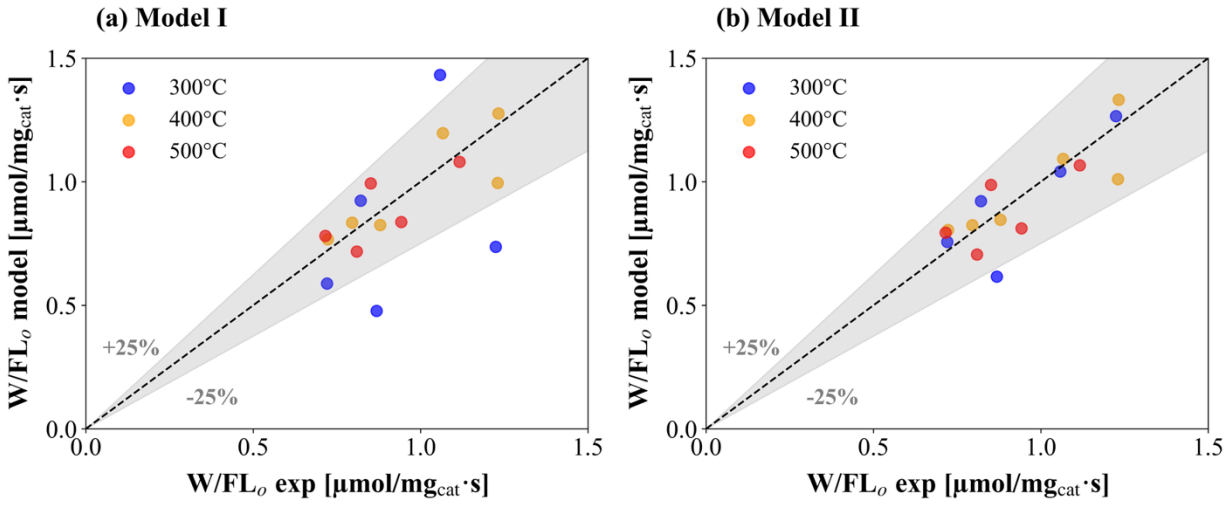

Figure 3.11. Parity plots comparing experimental and calculated values of W/F_{L_0} for the catalytic conversion of pyrolytic limonene using (a) Model I – considering only limonene adsorption, and (b) Model II – including competitive adsorption of pyrolysis by-products. Data points correspond to experiments at 300 °C (blue), 400 °C (orange), and 500 °C (red). The shaded area represents a ±25% deviation from the ideal 1:1 line (solid line).

Additional models considering hydrogen coverage (θ_H) from the dehydrogenation steps of Routes 1 and 2 were also tested. However, despite the inclusion of an additional adjustable parameter, these models did not significantly improve the fitting compared with Model I. This confirms that the better performance of Model II arises not from over-parametrization, but from the more realistic consideration of competitive adsorption of pyrolysis by-products. Their details and relative errors are presented in the appendix of Chapter 3 (Table A-3.4).

Considering that Model II best represents the conversion of pyrolytic limonene over the catalyst, it was selected as the baseline model to expand the study and obtain a global kinetic description capable of predicting both limonene conversion and product selectivity towards cymene. This step is critical to connect the kinetic model with the experimentally observed selectivity trends, since the catalytic system does not only convert limonene but also distributes it among cymene (B), cymenene (C, via a competitive pathway), and aromatics such as xylene (E) formed through cymene dealkylation. To achieve this, the adsorption constants (K_A, K_P) obtained from the previous optimization were fixed, ensuring consistency with the description of limonene consumption. The parameters α and β were re-estimated together with two additional constants

($k_{1,3}$, $k_{1,4}$) associated with the formation and consumption of cymene, this time using the experimental cymene molar flow as the objective function for parameter estimation.

The system of differential equations describing the conversion of limonene (X) into cymene and the distribution towards the other relevant products is given by:

$$\frac{dX}{dW} = \frac{(\Phi(T) \cdot \alpha + \beta) \cdot (1 - X)}{\left(1 + K_A \cdot F_{A_0} \cdot (1 - X) + K_P \cdot F_P\right)^2} \qquad (3.11)$$

$$\frac{dF_B}{dW} = r_B = \frac{k_{1,4}}{k_{1,4} + k_{1,3} \cdot \theta_*} \cdot (-r_1) \qquad (3.12)$$

$$\frac{dF_C}{dW} = r_2 = \alpha \cdot F_{A_0} \cdot (1 - X) \cdot (\Phi(T) - 1) \cdot \theta_*^2 \qquad (3.13)$$

$$\frac{dF_{H_2}}{dW} = r_B + 2 \cdot r_2 \qquad (3.14)$$

with: $\theta_* = \frac{1}{1+K_A \cdot F_{A_0} \cdot (1-X)+K_P \cdot F_P}$, and $\Phi(T)$ defined previously as the experimental rate ratio between Routes 1 and 2.

Here, r_1 and r_2 correspond to the rates of cymene and cymenene formation, respectively, while the contribution of Route 3 is lumped in the parameter β and thus does not appear explicitly in the system. Equation (3.12) accounts for both the formation of cymene via Route 1 and its consumption by dealkylation, while Equation (3.13) describes the direct formation of cymenene as a competitive pathway. The detailed derivation, including the treatment of surface intermediates and site balances, is provided in the appendix of Chapter 3.

The system of differential equations (Eqs 3.11 – 3.14) was integrated in Python with SciPy (*solve_ivp*, stiff solver BDF) using mass of catalyst (W) as the independent variable. The resulting predictions were compared with the experimental data (Figure 3.12). The quality of the extended model was first evaluated through parity plots, which allow a direct visualization of the agreement between calculated and experimental values for molar flow cymene, as well as for limonene conversion, cymenene, and hydrogen.

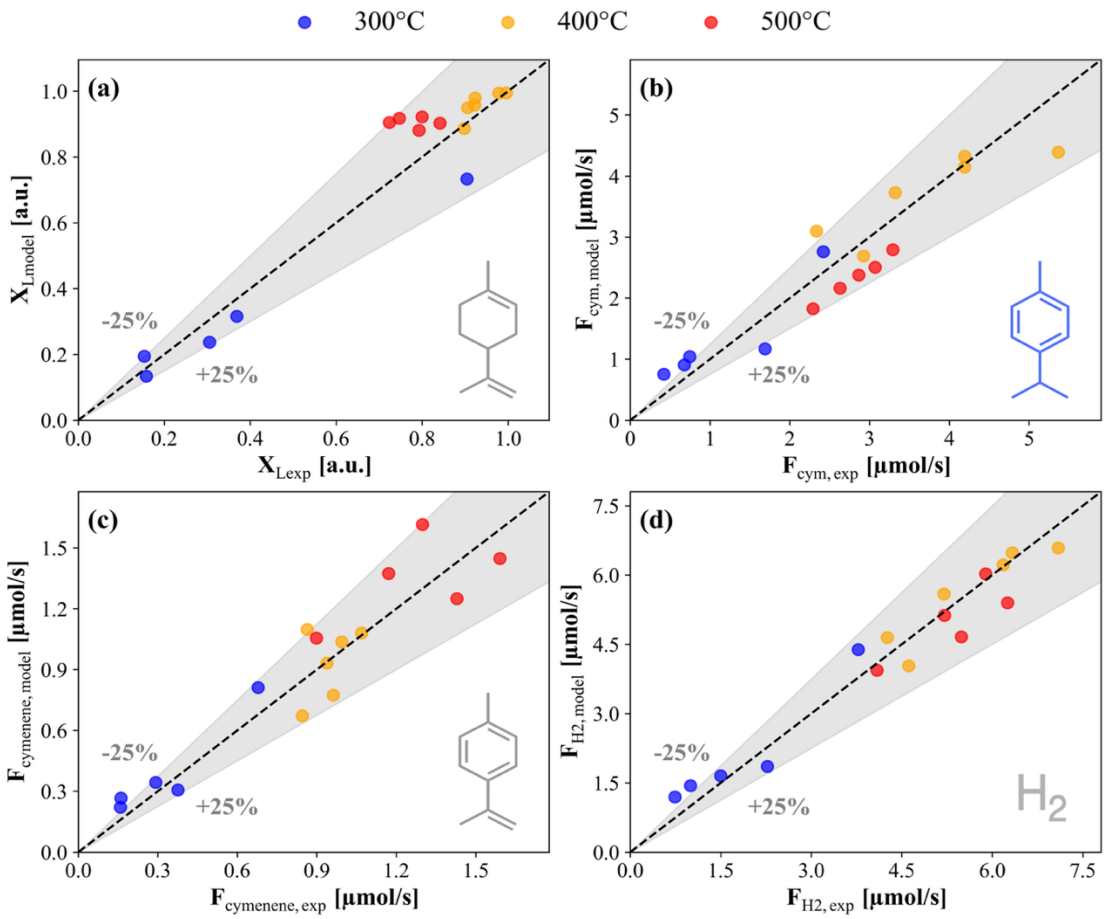

Figure 3.12. Parity plots comparing experimental and model-predicted values for (a) limonene conversion and the outlet molar flow rates of: (b) cymene, (c) cymenene, and (d) H_2 at 300 °C (blue), 400 °C (orange), and 500 °C (red). The shaded area corresponds to a ±25% deviation from the ideal 1:1 agreement (dashed line).

Figure 3.12 shows that the extended model reproduces the experimental data well across the three studied temperatures, with about 80% of the points falling within the ± 25% deviation band across all plots. This level of accuracy is generally considered acceptable in heterogeneous catalytic systems and has even been reported in kinetic studies of reactions with lower intrinsic variability than the present system [113–115], highlighting the robustness of the proposed model. In Figure 3.12a, a slight underestimation of limonene conversion is observed at 300 °C, which may be related to the stronger effect of competitive adsorption of pyrolysis by-products explicitly included in the model. It should also be noticed that the model assumes that all pyrolysis by-products (P) interact with the surface in the same manner (single K_P) an intentional lumping that likely contributes to

this residual bias. At 500 °C, in contrast, the model tends to overestimate conversion, suggesting that additional inhibitory effects not captured in the current formulation (e.g., surface blocking by dealkylation products) may become relevant at high temperature. With respect to cymene (Figure 3.12b), the largest deviations appear at 300 °C, which can be attributed to the variability at low temperature due to the presence of other pyrolysis-derived compounds. At 400 °C the agreement between predicted and measured data improves, and the amount of cymene generated increases; however, no clear systematic trend is observed in the residuals. At 500 °C, the model slightly underestimates cymene formation, and its overall yield decreases compared to 400 °C. This behavior is consistent with the onset of dealkylation of cymene to aromatic compounds, as described in previous studies of tandem reactors where a decrease in cymene yield has been observed at >400°C [28]. In addition, higher temperature favors the direct dehydrogenation pathway to cymenene (Route 2), reducing the relative contribution of cymene.

For cymenene (Figure 3.12c) and hydrogen (Figure 3.12d), the model predictions do not show a fully systematic trend, yet clear temperature effects are evident. Cymenene consistently increases with reactor temperature, reflecting the favored sequence of dehydrogenation steps, while hydrogen formation also rises from 300 to 400 °C, consistent with the endothermic nature of the dehydrogenation reactions, but levels off at 500 °C. The plateau in H_2 production suggests a limitation imposed by surface coverage or by-product desorption, which constrains the extent of dehydrogenation at higher temperature.

The kinetic and thermodynamic parameters were derived to ensure the physicochemical consistency of the model, according to the criteria defined in Section 3.2.3. The resulting parameters are reported in Table 3.4, and their implications are discussed in the following paragraphs.

The adsorption parameters in Table 3.4 were obtained from van't Hoff plots with coefficients of determination of r^2=0.98 (See Figure A-3.14). The calculated enthalpies are physically consistent, confirming the exothermic nature of the adsorption process; -73.5 kJ·mol^{-1} for limonene and -104.2 kJ·mol^{-1} for the lumped pyrolysis by-products. The more negative value obtained for the by-products, representative of alkenes (e.g., isoprene, hexene) and cycloalkenes (e.g., cyclohexene, 1-methyl-5-(1-methylethenyl)-(R), γ-elemene), indicates stronger adsorption compared to limonene.

Table 3.4. Thermodynamic and kinetic parameters obtained from the mechanistic model (Model II) for limonene conversion and product distribution over Pd/TiO_2–ZrO_2 catalysts.

Parameter	Description	Effect of temperature	Kinetic parameters
K_A	Adsorption equilibrium constant of limonene (**A**) on the active sites.	Decrease with T	$\Delta H_A\ [kJ \cdot mol^{-1}] = -73.50$ $\Delta S_A\ [J \cdot mol^{-1} \cdot K^{-1}] = -118.6$
K_P	Adsorption equilibrium constant of pyrolysis by-products (**P**) competing for sites.	Decrease with T	$\Delta H_P\ [kJ \cdot mol^{-1}] = -104.2$ $\Delta S_P\ [J \cdot mol^{-1} \cdot K^{-1}] = -193.7$
k_3	Rate constant for the lumped side reactions of adsorbed limonene to undesired products (Route 3).	Increase with T	$E_{a_3}\ [kJ \cdot mol^{-1}] = 109.2$
$k_{1,3}$	Rate constant for dealkylation of adsorbed cymene.	Increase with T	$E_{a_{1,3}}\ [kJ \cdot mol^{-1}] = 19.8$
$k_{1,4}$	Desorption rate constant of cymene.	Increase with T	$E_{a_{1,4}}\ [kJ \cdot mol^{-1}] = 12.32$

This trend is consistent with the experimental data and with the need to include an adsorption parameter for these compounds in the site balance, particularly at 300°C, where adsorption phenomena exhibit greater influence. Moreover, the calculated enthalpies fall within ranges

reported in literature; infrared spectroscopy and DFT studies have shown adsorption enthalpies of limonene on TiO_2 of -71 $\pm$ 11 kJ·mol^{-1} [116], while larger unsaturated molecules such as olefins and cycloalkenes tipically adsorb more strongly, with values between -80 and -130 kJ · mol^{-1}[117,118]. On the other hand, the adsorption entropies were also negative, as expected for molecules immobilized on the catalyst surface, reflecting the loss of translational and rotational degrees of freedom upon adsorption. The fitted values were -118.6 J·mol^{-1}·K^{-1} for limonene and -193.7 J·mol^{-1}·K^{-1}for the pyrolysis by-products. Both values are physically meaningful and satisfy the empirical correlation between -ΔH and -ΔS proposed by Vannice, which, for the obtained enthalpies, sets upper bounds of 154 and 197 J·mol^{-1}·K^{-1} for limonene and the by-products, respectively. Moreover, these entropies values fall within the range typically reported for olefins and aromatics adsorbed on other oxides [117], further supporting the validity of the adsorption parameters obtained in this study. Consistently, the corresponding gas-phase molar entropies for similar olefins/aromatics are on the order of ~300–360 J·mol^{-1}·K^{-1}, according to NIST SRD-69, so $|-\Delta S_{ads}| < S°_{gas}$ as expected.

The parameters associated with cymene formation provide direct evidence of the competition between its stabilization and secondary consumption. The desorption step ($k_{1,4}$) showed the lowest activation energy (12.3 kJ·mol^{-1}), consistent with a facile process that enables cymene to leave the surface once formed. This suggests a weak interaction with the catalytic surface, which is in line with the molecular structure of cymene and with its exclusion from the site balance; unlike limonene, cymene lacks an exocyclic double bond that could engage in stronger π–Lewis's interactions, thus favoring facile desorption once formed. In contrast, the dealkylation pathway ($k_{1,3}$) exhibited a slightly higher barrier (19.8 kJ·mol^{-1}) indicating that while this process becomes more relevant at elevated temperatures, it is less favorable than direct desorption. Moreover, the activation energy obtained for this process is consistent with values reported in the literature for the formation of aromatics from alkyl-aromatics over acidic catalysts such as zeolites [119]. This balance rationalizes the experimental trends; cymene is the dominant product at moderate temperature, whereas its yield decreases at 500 °C due to both partial conversion into aromatics and the increasing contribution of the direct dehydrogenation pathway of limonene to cymenene.

On the other hand, the side reactions of adsorbed limonene, represented by the rate constant k_3 displayed a much higher apparent activation energy (109.2 kJ·mol^{-1}). This confirms that, among the considered pathways, this route is the least favored by the catalyst and becomes significant only

at higher temperatures. Moreover, this value lies within the range reported in the literature for simplified kinetic models describing sequences of parallel and/or consecutive reactions (cracking, cyclization, and aromatization) [25,120,121], reinforcing the physical consistency of the kinetic scheme. All three parameters ($k_{1,3}$, $k_{1,4}$, and k_3) were obtained from Arrhenius correlations with coefficients of determination close to unity confirming the robustness of the fitted kinetic constants. In addition to the physicochemical consistency of the fitted parameters, a verification was carried out by comparing model predictions with independent experimental profiles at 400 °C, obtained by varying the catalyst mass in Reactor 2 under constant limonene feed from Reactor 1 (Figure 3.13).

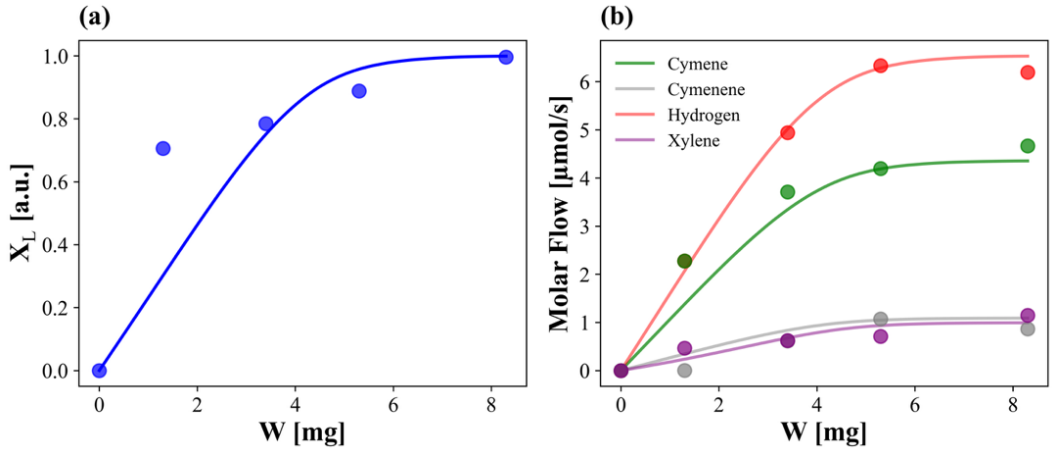

Figure 3.13. Independent validation of the extended kinetic model at 400 °C under constant feed conditions from Reactor 1 (limonene: 6.73 µmol/s; pyrolysis by-products: 17.0 µmol/s) and varying catalyst mass in Reactor 2 (W). (a) Limonene conversion; (b) molar flow of cymene, cymenene, hydrogen, and xylene. Symbols represent experimental data (including error bars for selected points), while solid lines correspond to model predictions.

Figure 3.13a shows that the model fairly reproduces most of the limonene conversion profile, although a deviation is observed at the reactor inlet, where the model does not fully capture the initial sharp increase in conversion. In contrast, Figure 3.13b demonstrates that the model successfully predicts cymene as the dominant product, reproducing both its stabilization at intermediate catalyst loadings and its partial consumption via dealkylation, as evidenced by the progressive formation of xylene. The accurate description of cymene's trajectory, together with the consistent prediction of secondary products such as cymenene and hydrogen, highlights the

robustness of the proposed kinetic scheme. Most importantly, this validation confirms cymene selectivity as the central descriptor of the catalytic performance, strengthening confidence in the mechanistic interpretation proposed in this work.

3.4. Conclusions

This study provides a mechanistic interpretation of the catalytic transformation of pyrolytic limonene into cymene over Pd/ZrO_2–TiO_2 catalysts. The combination of Lewis acidity and highly dispersed Pd (~56%) enabled cymene to be the dominant product, while cymenene and monoaromatics appeared only as minor species. A Langmuir–Hinshelwood kinetic model, explicitly considering the competing adsorption of limonene and pyrolysis-derived species, reproduced the experimental conversion trends with reasonable accuracy. The adsorption parameters for limonene ($\Delta H_A = -73.5$ kJ·mol^{-1}; $\Delta S_A = -118.6$ J·mol^{-1}·K^{-1}) are physicochemically consistent and similar to previous literature reports. The calculated activation energies for cymene formation ($E_{a_{1,4}} = 12.3\ \mathrm{kJ \cdot mol^{-1}}$) and for its dealkylation to aromatics ($E_{a_{1,3}} = 19.8\ \mathrm{kJ \cdot mol^{-1}}$) were also in line with values previously reported. The results support a pathway in which limonene is first isomerized to terpinene/terpinolene on Lewis sites and subsequently is dehydrogenated on metallic Pd, with parallel but less significant routes leading to cymenene and aromatics. Even with the necessary assumptions in compound quantification and the limonene feed from natural rubber pyrolysis to the second reactor, this study advances prior pyrolysis work by directly coupling experimental evidence with a surface-reaction kinetic model, capturing the observed trends robustly**.** Overall, this mechanistic approach establishes a validated scheme for pyrolytic limonene upgrading to cymene and paves the way toward the intelligent design of bifunctional catalytic reactors for the selective transformation of limonene-rich pyrolytic vapors, such as those derived from mining truck waste tires, into fine chemicals and value-added products.

Chapter 4. Conclusions and Outlook

4.1. General Conclusions

This doctoral research addressed the valorization of mining truck waste tires through the catalytic transformation of pyrolytic limonene into cymene over bifunctional Pd/ZrO_2-TiO_2. The work integrated the synthesis and characterization of catalysts, with micro-pyrolysis experimentation to elucidate the relationship between metal–acid cooperation and the reaction mechanisms controlling the formation of cymene from pyrolytic limonene. Collectively, the results contribute to the comprehensive understanding of the chemical reaction pathways and the catalytic phenomena, underlying the conversion of tire-derived vapors into high-value chemical compounds such as cymene.

The formation of pyrolytic limonene from waste tire pyrolysis was studied in an analytical system (Py-GC-MS) using waste tires and natural rubber. The results confirmed that limonene is formed from natural rubber after C–C bond cleavage of polymeric chains, followed by either (i) intramolecular cyclization or (ii) a Diels–Alder reaction between two isoprene units. Thereafter, limonene undergoes secondary reactions yielding cycloalkenes and aromatics. Moreover, the data recorded for different reaction conditions enabled the development of a detailed kinetic model which accurately predicted the evolution of limonene and the formation of secondary compounds over a wide temperature range, validating the mechanistic consistency of the model. This kinetic framework provided a strict control over limonene formation and other pyrolysis by-products, which is crucial for controlling the feed composition for subsequent catalytic studies.

Building upon this kinetic foundation, during the second stage of the thesis (specific objectives 2 ad 3) the catalytic conversion of pyrolytic limonene over Pd/TiO_2-ZrO_2 catalysts with different densities of Lewis acid sites was investigated. The impregnation of TiO_2 with of zirconia modified the electronic structure of titania surface, altering the strength and distribution of acid sites. Pyridine-FTIR spectra indicated the predominant presence of Lewis acid centers, while NH_3-TPD–MS profiles revealed the presence of medium-strength acidity.

Catalytic testing was carried out for TiO_2-ZrO_2 supports containing different loadings of Zr, demonstrating that those supports with 10 %wt of zirconia holds intrinsic activity for producing cymene precursors via isomerization. The impregnation of Pd onto TiO_2–ZrO_2 support resulted in a high Pd dispersion while preserving the predominantly Lewis acidic nature of the surface. The

Pd particle size was measured by CO-chemisorption and STEM-EDX analyses, both yielding a metal dispersion close to 50%. Moreover, Pd addition generates slightly quantitative changes in the density and distribution of surface acid sites, affecting both the total acidity and the weak-to-total site Lewis's ratios.

Catalytic evaluation of these catalysts for pyrolytic limonene conversion demonstrated that cymene formation is favored on materials exhibiting a higher proportion of weak-to-medium acid sites. This behavior was consistent with the Sabatier principle, suggesting that excessively strong acid–molecule interactions can promote bond cleavage, whereas moderate Lewis's acidity provides the optimal balance for selective isomerization and dehydrogenation routes.

The Langmuir–Hinshelwood kinetic model describing the catalytic transformation of pyrolytic limonene into cymene over Pd/TiO_2–ZrO_2 incorporated competitive adsorption of pyrolysis by-products and successfully reproduced experimental selectivity trends at different temperatures. The findings confirmed that Pd sites catalyze the dehydrogenation of limonene to cymenene, whereas weak Lewis's acid sites promote isomerization and subsequent conversion to cymene, validating the proposed bifunctional mechanism.

Integrating all these outcomes, this thesis establishes a mechanistic framework connecting the non-catalytic formation of pyrolytic limonene with its catalytic upgrading to cymene. The combination of novel experimental methodologies and mechanism-oriented modeling approaches revealed how catalyst composition, acidity, and metal dispersion collectively govern product distribution and reaction pathways. Overall, this work lays the foundation for designing catalytic micro-pyrolysis experiments that enable a quantitative interpretation of catalyst performance. Moreover, it provides a conceptual and methodological basis for advancing a mechanism-driven understanding of catalytic pyrolysis beyond traditional empirical interpretations.

4.2. Outlook

Future work should focus on extending the kinetic model developed in this thesis under more realistic conditions, particularly by applying it to the pyrolysis of mining truck waste tires (MTWT), where the coexistence of natural and synthetic rubbers may introduce polymer–polymer interactions that deviate from the current predictions. Applying the model under these conditions and at a larger scale, e.g., pilot, will allow assessment of its predictive robustness and of the achievable yields and selectivities. On the catalytic side, further investigation is also required to get insight into of metal–acid synergy and surface chemistry. Complementary techniques such as

in situ X-ray photoelectron spectroscopy (XPS) could help determine the oxidation states of Pd, Ti, and Zr and elucidate electronic interactions within the bifunctional interface.

The long-term stability of Pd/TiO_2–ZrO_2 catalysts should also be explored, focusing on the evolution of surface acidity and the mechanisms of coke deposition during repetitive cycles of reaction and regeneration.

Moreover, future studies should aim to identify and quantify surface intermediates under relevant reaction conditions. While true operando-DRIFTS may be challenging under pyrolytic atmospheres, in-situ spectroscopic approaches—such as transmission FTIR with limonene vapor feeds or temperature-programmed surface reactions coupled to mass spectrometry—could help clarify the adsorption and transformation pathways. Dedicated experiments using pure limonene could help elucidate how adsorption modes—particularly at the exocyclic double bond—govern the isomerization pathway, while Pd sites may activate C–H bonds and drive the parallel dehydrogenation route to cymenene.

Additionally, performing catalytic pyrolysis in the presence of hydrogen could reveal whether H_2 suppresses or enhances cymene formation, providing deeper insight into the balance between hydrogenation and dehydrogenation reactions. Ultimately, extending this research toward pilot-scale catalytic upgrading may pave the way for sustainable aromatic production from mining tire waste within a circular industrial framework.

Acknowledgements

This work was supported by the ANID National PhD Scholarship N°21210750 and the research project FONDECYT Regular Nº1240054. Access to key analytical and pyrolytic facilities was enabled through the FONDEQUIP Project EQMI170077, led by Prof. Serguei Alejandro at the Laboratorio de Cromatografía Gaseosa y Pirólisis Analítica (LCGPA), Universidad del Bío-Bío**.** I also acknowledge Prof. Cristian H. Campos and Universidad Andrés Bello (UNAB) for their guidance and support in advanced catalyst characterization techniques.

I gratefully acknowledge Johnson Matthey for providing $PdCl_2$ through the PGM Award Program, and Francisco Medina (LCGPA–UBB) for his guidance and assistance with micro-pyrolysis (Py-GC/MS) experiments.

Finally, I acknowledge the Thermochemical Conversion of Biomass (TCCB) group at Ghent University for providing the facilities, technical support, and collaboration that contributed to this work.

Internships

1. Laboratorio de Cromatografía Gaseosa y Pirólisis Analítica (LCGPA), Universidad del Bío-Bío (UBB), Concepción, Chile, under the tutelage of Prof. Serguei Alejandro. (July 4 – August 31, 2022).

2. Thermochemical Conversion of Biomass (TCCB) Group, Department of Green Chemistry and Technology, Ghent University, Ghent, Belgium, under the tutelage of Prof. Frederik Ronsse. (September 14, 2024 – February 21, 2025).

Scientific Contributions

Publications

1. **Poblete, J.**, Jiménez, R., Ronsse, F., Ghysels, S., & Arteaga-Pérez, L.E.*(2025). *Understanding limonene synthesis from waste tire pyrolysis through a kinetics-based perspective.* Journal of Analytical and Applied Pyrolysis, 107207. https://doi.org/10.1016/j.jaap.2025.107207.
2. **Poblete, J.**, Ghysels, S.* , Ronsse, F., Gómez, D., Jiménez, R., & Arteaga-Pérez, L.E.*(2025). *A mechanistic approach to the transformation of pyrolytic limonene into cymene over bifunctional Pd/TiO_2–ZrO_2 catalysts.* Chemical Engineering Journal. *(Submitted / Under review).*
3. Osorio-Vargas, P., Lick, I. D., Pizzio, L. R., Alejandro, S., Casas-Ledón, Y., **Poblete, J.**, et al. (2022). *Using tungstophosphoric acid-modified CeO_2, TiO_2, and SiO_2 catalysts to promote secondary reactions during waste tire pyrolysis.* Molecular Catalysis, 112682. https://doi.org/10.1016/j.mcat.2022.112682

Conferences

1. **Poblete, J.** (2024). *Estudio de la generación de p-cimeno a partir de la pirólisis catalítica ex-situ de caucho natural con catalizadores bifuncionales ácido-metálicos.* **XXIX Congreso Iberoamericano de Catálisis (CICAT 2024)**, Bilbao, Spain. *Oral presentation.*

2. **Poblete, J.** (2024). *Unraveling the mechanism of limonene generation through fast pyrolysis of waste tires: A model-based approach.* **24th International Symposium on Analytical and Applied Pyrolysis (Pyro2024)**, Beijing, China. *Oral presentation.*

3. Poblete, J. (2023). *Study of p-cymene generation from ex-situ catalytic pyrolysis of mining truck tires with bifunctional acid-metallic catalysts.* **XII Jornadas Chilenas de Catálisis y Adsorción**, Linares, Chile. *Poster presentation.*

References

[1] N.H. Zerin, M.G. Rasul, M.I. Jahirul, A.S.M. Sayem, End-of-life tyre conversion to energy: A review on pyrolysis and activated carbon production processes and their challenges, Science of The Total Environment 905 (2023) 166981. https://doi.org/10.1016/J.SCITOTENV.2023.166981.

[2] M. Hashamfirooz, M.H. Dehghani, M. Khanizadeh, M. Aghaei, P. Bashardoost, M.S. Hassanvand, M. Hassanabadi, F. Momeniha, A systematic review of the environmental and health effects of waste tires recycling, Heliyon 11 (2025). https://doi.org/10.1016/j.heliyon.2025.e41909.

[3] J.D. Martínez, An overview of the end-of-life tires status in some Latin American countries: Proposing pyrolysis for a circular economy, Renewable and Sustainable Energy Reviews 144 (2021) 111032. https://doi.org/10.1016/J.RSER.2021.111032.

[4] ANIR, Estudio del Material Disponible País (MDP) y el reciclado de los Neumaticos en Chile, 2022. https://www.anir.cl/wp-content/uploads/2022/12/ANIR2021-NFU-Estudio_del_material_disponible_País.pdf. (accessed July 31, 2024).

[5] Camara de la Industria del Neumatico de Chile, Generación de Neumaticos Fuera de Uso, 2020. https://cinc.cl/wp-content/uploads/2020/07/200727-Estadísticas-NFU.pdf (accessed July 31, 2024).

[6] Ministerio del Medio Ambiente, Ley REP: Se publicó decreto que obliga a empresas importadoras de neumáticos a recolectar y reciclar el 90% de ellos – MMA, (n.d.). https://mma.gob.cl/ley-rep-se-publico-decreto-que-obliga-a-empresas-importadoras-de-neumaticos-a-recolectar-y-reciclar-el-90-de-ellos/ (accessed July 31, 2024).

[7] W. Ferdous, A. Manalo, O. AlAjarmeh, A.A. Mohammed, C. Salih, P. Yu, M. Mehrinejad Khotbehsara, P. Schubel, Static behaviour of glass fibre reinforced novel composite sleepers for mainline railway track, Eng. Struct. 229 (2021) 111627. https://doi.org/10.1016/J.ENGSTRUCT.2020.111627.

[8] S. Wang, M. Cheng, M. Xie, Y. Yang, T. Liu, T. Zhou, Q. Cen, Z. Liu, B. Li, From waste to energy: Comprehensive understanding of the thermal-chemical utilization techniques for waste tire recycling, Renewable and Sustainable Energy Reviews 211 (2025) 115354. https://doi.org/10.1016/J.RSER.2025.115354.

[9] Y. Hu, X. Yu, J. Ren, Z. Zeng, Q. Qian, Waste tire valorization: Advanced technologies, process simulation, system optimization, and sustainability, Science of The Total Environment 942 (2024) 173561. https://doi.org/10.1016/J.SCITOTENV.2024.173561.

[10] M. Zhang, Y. Qi, W. Zhang, M. Wang, J. Li, Y. Lu, S. Zhang, J. He, H. Cao, X. Tao, H. Xu, A review on waste tires pyrolysis for energy and material recovery from the optimization perspective, Renewable and Sustainable Energy Reviews 199 (2024) 114531. https://doi.org/10.1016/J.RSER.2024.114531.

[11] Kal Tire, Reciclaje de Neumáticos de Minería., (n.d.). https://www.kaltiremining.com/es/reciclaje-de-neumaticos-de-mineria/ (accessed August 21, 2024).

[12] Arrigoni Ambiental NFU, Planta de Pirólisis, (n.d.). https://arrigoniambientalnfu.cl/quienes-somos/ (accessed June 25, 2022).

[13] Anglo American, Reporte de Sustentabilidad 2022, 2022.

[14] M. Arabiourrutia, G. Lopez, M. Artetxe, J. Alvarez, J. Bilbao, M. Olazar, Waste tyre valorization by catalytic pyrolysis – A review, Renew. Sustain. Energy Rev. 129 (2020) 109932. https://doi.org/10.1016/j.rser.2020.109932.

[15] J.D. Martínez, N. Puy, R. Murillo, T. García, M.V. Navarro, A.M. Mastral, Waste tyre pyrolysis – A review, Renewable and Sustainable Energy Reviews 23 (2013) 179–213. https://doi.org/10.1016/J.RSER.2013.02.038.

[16] P. Osorio-Vargas, K. Shanmugaraj, C. Herrera, C.H. Campos, C.C. Torres, F. Castillo-Puchi, L.E. Arteaga-Pérez, Valorization of Waste Tires via Catalytic Fast Pyrolysis Using Palladium Supported on Natural Halloysite, Ind. Eng. Chem. Res. 60 (2021) 18806–18816. https://doi.org/10.1021/acs.iecr.1c02797.

[17] A.A. Merchant, M.A. Petrich, Pyrolysis of scrap tires and conversion of chars to activated carbon, AIChE Journal 39 (1993) 1370–1376. https://doi.org/https://doi.org/10.1002/aic.690390814.

[18] P.T. Williams, Pyrolysis of waste tyres: A review, Waste Management 33 (2013) 1714–1728. https://doi.org/10.1016/J.WASMAN.2013.05.003.

[19] R.G. dos Santos, C.L. Rocha, F.L.S. Felipe, F.T. Cezario, P.J. Correia, S. Rezaei-Gomari, Tire waste management: an overview from chemical compounding to the pyrolysis-derived

fuels, J. Mater. Cycles Waste Manag. 22 (2020) 628–641. https://doi.org/10.1007/s10163-020-00986-8.

[20] H. Yaqoob, Y.H. Teoh, M.A. Jamil, M. Gulzar, Potential of tire pyrolysis oil as an alternate fuel for diesel engines: A review, Journal of the Energy Institute 96 (2021) 205–221. https://doi.org/10.1016/J.JOEI.2021.03.002.

[21] B. Danon, P. Van Der Gryp, C.E. Schwarz, J.F. Görgens, A review of dipentene (dl-limonene) production from waste tire pyrolysis, J. Anal. Appl. Pyrolysis 112 (2015) 1–13. https://doi.org/10.1016/J.JAAP.2014.12.025.

[22] M. Zhang, Y. Qi, W. Zhang, M. Wang, J. Li, Y. Lu, S. Zhang, J. He, H. Cao, X. Tao, H. Xu, S. Zhang, A review on waste tires pyrolysis for energy and material recovery from the optimization perspective, Renewable and Sustainable Energy Reviews 199 (2024) 114531. https://doi.org/https://doi.org/10.1016/j.rser.2024.114531.

[23] I.M. ROFIQUL, H. HANIU, A.B.M. RAFIQUL, Limonene-Rich Liquids from Pyrolysis of Heavy Automotive Tire Wastes, Journal of Environment and Engineering 2 (2007) 681–695. https://doi.org/10.1299/jee.2.681.

[24] D. Correa-Muriel, H. Valencia-Sánchez, H. Cortes-Hernández, D. González-Vera, J. Herrera, C.H. Campos, M.L. Casella, L.E. Arteaga-Perez, P. Osorio-Vargas, Nickel and Cobalt Ilmenites-Based Catalysts for Upgrading Pyrolytic Oil during Pyrolysis of Waste Tires, Catalysts 12 (2022). https://doi.org/10.3390/catal12111437.

[25] P. Osorio-Vargas, I.D. Lick, L.R. Pizzio, S. Alejandro, Y. Casas-Ledón, J. Poblete, M.L. Casella, L.E. Arteaga-Pérez, Using tungstophosphoric acid-modified CeO2, TiO2, and SiO2 catalysts to promote secondary reactions leading to aromatics during waste tire pyrolysis, Mol. Catal. 531 (2022) 112682. https://doi.org/10.1016/J.MCAT.2022.112682.

[26] T. Menares, R. Romero, F. Sobrevía, F. Ronsse, Y. Casas-Ledón, P. Osorio-Vargas, L.E. Arteaga-Pérez, Production of limonene from waste tires via catalytic fast pyrolysis: a statistical–based screening on Ni-, Pd-, Co-, and Fe-supported catalysts, Biomass Convers. Biorefin. 13 (2023) 11259–11274. https://doi.org/10.1007/s13399-022-03277-4.

[27] S.D. Stefanidis, E. Pachatouridou, E. Heracleous, A.A. Lappas, I.A. Vasalos, Chemical Recycling of End-of-Life Tires Using Catalytic Pyrolysis: Effects of Catalysts and Process Conditions toward the Production of a Highly Aromatic Pyrolysis Oil, Cite This: Ind. Eng. Chem. Res 64 (2025). https://doi.org/10.1021/acs.iecr.5c02163.

[28] Y. Zhang, X. Meng, J. Jiang, A.J. Ragauskas, J. Wang, Sustainable valorization of waste tires: Selective hydrotreating for renewable p-cymene production, Fuel 364 (2024) 131137. https://doi.org/10.1016/J.FUEL.2024.131137.

[29] Alibaba, d-Limonene product listings, (2025). https://spanish.alibaba.com/trade/search?spm=a2700.7724857.the-new-header_fy23_pc_search_bar.keydown__Enter&tab=all&SearchText=limonene&has4Tab=true (accessed November 7, 2025).

[30] R. Lopez, Economía Circular en Neumáticos OTR, Universidad de Chile, 2024.

[31] ECOTR, Antecedentes técnicos: Valorización de Neumáticos Fuera de Uso de la gran minería, 2017. https://rechile.mma.gob.cl/wp-content/uploads/2019/06/19.-Ecotr-Chile-Spa-proyecto-NFU-minero.pdf (accessed January 16, 2026).

[32] A. Corma, S. Iborra, A. Velty, Chemical Routes for the Transformation of Biomass into Chemicals, Chem. Rev. 107 (2007) 2411–2502. https://doi.org/10.1021/cr050989d.

[33] M.A. Martín-Luengo, M. Yates, M.J. Martínez Domingo, B. Casal, M. Iglesias, M. Esteban, E. Ruiz-Hitzky, Synthesis of p-cymene from limonene, a renewable feedstock, Appl. Catal. B 81 (2008) 218–224. https://doi.org/10.1016/j.apcatb.2007.12.003.

[34] M. Salgado-Ramos, S. Tabasso, E.C. Gaudino, G. Cravotto, Process Intensification for Sustainable Microwave-Assisted Bio p-Cymene Production from Limonene, Cite This: Ind. Eng. Chem. Res 63 (2024) 7507–7518. https://doi.org/10.1021/acs.iecr.4c00117.

[35] Alibaba, p-Cymene product listings, (2025). https://spanish.alibaba.com/g/p-cymene.html (accessed November 8, 2025).

[36] A. Marchese, C.R. Arciola, R. Barbieri, A.S. Silva, S.F. Nabavi, A.J.T. Sokeng, M. Izadi, N.J. Jafari, I. Suntar, M. Daglia, S.M. Nabavi, Update on monoterpenes as antimicrobial agents: A particular focus on p-cymene, Materials 10 (2017) 1–15. https://doi.org/10.3390/ma10080947.

[37] M. Kamitsou, G.D. Panagiotou, K.S. Triantafyllidis, K. Bourikas, A. Lycourghiotis, C. Kordulis, Transformation of α-limonene into p-cymene over oxide catalysts: A green chemistry approach, Appl. Catal. A Gen. 474 (2014) 224–229. https://doi.org/10.1016/j.apcata.2013.06.001.

[38] B. Danon, J. Görgens, Determining rubber composition of waste tyres using devolatilisation kinetics, Thermochim. Acta 621 (2015) 56–60. https://doi.org/10.1016/J.TCA.2015.10.008.

[39] N.M. Mkhize, B. Danon, P. van der Gryp, J.F. Görgens, Kinetic study of the effect of the heating rate on the waste tyre pyrolysis to maximise limonene production, Chem. Eng. Res. Des. 152 (2019) 363–371. https://doi.org/10.1016/J.CHERD.2019.09.036.

[40] N.M. Mkhize, P. van der Gryp, B. Danon, J.F. Görgens, Effect of temperature and heating rate on limonene production from waste tyre pyrolysis, J. Anal. Appl. Pyrolysis 120 (2016) 314–320. https://doi.org/https://doi.org/10.1016/j.jaap.2016.04.019.

[41] K. Januszewicz, P. Kazimierski, W. Kosakowski, W.M. Lewandowski, Waste tyres pyrolysis for obtaining limonene, Materials 13 (2020) 1–30. https://doi.org/10.3390/ma13061359.

[42] P. Osorio-Vargas, T. Menares, I.D. Lick, M.L. Casella, R. Romero, R. Jiménez, L.E. Arteaga-Pérez, Tuning the product distribution during the catalytic pyrolysis of waste tires: The effect of the nature of metals and the reaction temperature, Catal. Today 372 (2021) 164–174. https://doi.org/10.1016/j.cattod.2020.10.035.

[43] F. Xu, B. Wang, D. Yang, X. Ming, Y. Jiang, J. Hao, Y. Qiao, Y. Tian, TG-FTIR and Py-GC/MS study on pyrolysis mechanism and products distribution of waste bicycle tire, Energy Convers. Manag. 175 (2018) 288–297. https://doi.org/10.1016/J.ENCONMAN.2018.09.013.

[44] D. Zheng, J. Cheng, C. Dai, R. Xu, X. Wang, N. Liu, N. Wang, G. Yu, B. Chen, Study of passenger-car-waste-tire pyrolysis: Behavior and mechanism under kinetical regime, Waste Management 148 (2022) 71–82. https://doi.org/10.1016/J.WASMAN.2022.05.024.

[45] T. Menares, J. Herrera, R. Romero, P. Osorio, L.E. Arteaga-Pérez, Waste tires pyrolysis kinetics and reaction mechanisms explained by TGA and Py-GC/MS under kinetically-controlled regime, Waste Management 102 (2020) 21–29. https://doi.org/10.1016/J.WASMAN.2019.10.027.

[46] M. Kar, T.G. Lenz, J.D. Vaughan, Predictive Force-Field Calculations for the Equilibrium Dimerization of Isoprene, J. Phys. Chem 98 (1994) 2489–2493. https://doi.org/10.1021/j100060a043.

[47] S. Liu, J. Yu, K. Bikane, T. Chen, C. Ma, B. Wang, L. Sun, Rubber pyrolysis: Kinetic modeling and vulcanization effects, Energy 155 (2018) 215–225. https://doi.org/10.1016/j.energy.2018.04.146.

[48] K. Wang, T. Shan, B. Li, Y. Zheng, H. Xu, C. Wang, X. Tian, Study on pyrolysis characteristics, kinetics and thermodynamics of waste tires catalytic pyrolysis with low-cost catalysts, Fuel 356 (2024). https://doi.org/10.1016/j.fuel.2023.129644.

[49] P. Osorio-Vargas, C.H. Campos, C.C. Torres, C. Herrera, K. Shanmugaraj, T.M. Bustamante, J.N. Diaz de Leon, F. Medina, L.E. Arteaga-Pérez, Catalytic pyrolysis of used tires on noble-metal-based catalysts to obtain high-value chemicals: Reaction pathways, Catal. Today (2021). https://doi.org/10.1016/j.cattod.2021.06.029.

[50] J. Wang, X. Dong, Z. Zuo, Catalytic Pyrolysis of Waste Bicycle Tires and Engine Oil to Produce Limonene, (2023). https://doi.org/10.3390/en16114351.

[51] W.; Han, D.; Han, H. Chen, W. Han, D. Han, H. Chen, Pyrolysis of Waste Tires: A Review, (2023). https://doi.org/10.3390/polym15071604.

[52] J. Wu, Z. Zhang, D. Li, Y. Zhang, J. Wang, J. Jiang, Converting waste tires into p-cymene through hydropyrolysis and selective gas-phase hydrogenation/dehydrogenation, Waste Manag. 174 (2024) 282–289. https://doi.org/10.1016/J.WASMAN.2023.12.009.

[53] K. Ding, Z. Zhong, B. Zhang, J. Wang, A. Min, R. Ruan, Catalytic pyrolysis of waste tire to produce valuable aromatic hydrocarbons: An analytical Py-GC/MS study, J. Anal. Appl. Pyrolysis 122 (2016) 55–63. https://doi.org/10.1016/J.JAAP.2016.10.023.

[54] B.M. Reddy, A. Khan, Recent advances on TiO2-ZrO2 mixed oxides as catalysts and catalyst supports, Catal. Rev. Sci. Eng. 47 (2005) 257–296. https://doi.org/10.1081/CR-200057488.

[55] H. Hattori, Y. Ono, Solid acid catalysis: from fundamentals to applications, CRC Press, 2015.

[56] K. Tanabe, M. Misono, H. Hattori, Y. Ono, New solid acids and bases: their catalytic properties, Elsevier, 1990.

[57] E. Yılmazoğlu, M. Akgün, p-Cymene production from orange peel oil using some metal catalyst in supercritical alcohols, J. Supercrit. Fluids 131 (2018) 37–46. https://doi.org/10.1016/J.SUPFLU.2017.08.015.

[58] B. Qu, A. Li, Y. Qu, T. Wang, Y. Zhang, X. Wang, Y. Gao, W. Fu, G. Ji, Kinetic analysis of waste tire pyrolysis with metal oxide and zeolitic catalysts, J. Anal. Appl. Pyrolysis 152 (2020) 104949. https://doi.org/10.1016/J.JAAP.2020.104949.

[59] K. Wang, T. Shan, B. Li, Y. Zheng, H. Xu, C. Wang, X. Tian, Study on pyrolysis characteristics, kinetics and thermodynamics of waste tires catalytic pyrolysis with low-cost catalysts, Fuel 356 (2024) 129644. https://doi.org/10.1016/J.FUEL.2023.129644.

[60] C. Tavera-Ruiz, P. Gauthier-Maradei, · Mickaël Capron, D. Ferreira-Beltran, C. Palencia-Blanco, J.-C. Morin, · Franck Dumeignil, An Alternative to the Cymenes Production from Scrap Tire Rubber Using Heteropolyacid Catalysts, Waste Biomass Valorization 10 (2019) 3057–3069. https://doi.org/10.1007/s12649-018-0310-1.

[61] S. Dabic-Miletic, V. Simic, S. Karagoz, End-of-life tire management: a critical review, Environmental Science and Pollution Research 28 (2021) 68053–68070. https://doi.org/10.1007/s11356-021-16263-6.

[62] M. Zhang, Y. Qi, W. Zhang, M. Wang, J. Li, Y. Lu, S. Zhang, J. He, H. Cao, X. Tao, H. Xu, A review on waste tires pyrolysis for energy and material recovery from the optimization perspective, Renew. Sustain. Energy Rev. 199 (2024) 114531. https://doi.org/10.1016/J.RSER.2024.114531.

[63] A. Rowhani, T.J. Rainey, Scrap tyre management pathways and their use as a fuel - A review, Energies (Basel). 9 (2016) 1–26. https://doi.org/10.3390/en9110888.

[64] B. Rodgers, W. Waddell, Tire Engineering, The Science and Technology of Rubber (2013) 653–695. https://doi.org/10.1016/B978-0-12-394584-6.00014-5.

[65] G. Zhang, F. Chen, Y. Zhang, L. Zhao, J. Chen, L. Cao, J. Gao, C. Xu, Properties and utilization of waste tire pyrolysis oil: A mini review, Fuel Processing Technology 211 (2021) 106582. https://doi.org/10.1016/J.FUPROC.2020.106582.

[66] F. Campuzano, J. Daniel Martínez, A.F.A. Santamaría, S.M. Sarathy, W.L. Roberts, Pursuing the End-of-Life Tire Circularity: An Outlook toward the Production of Secondary Raw Materials from Tire Pyrolysis Oil, (2023). https://doi.org/10.1021/acs.energyfuels.3c00847.

[67] M. Chávez-Delgado, J.R. Colina, C. Segura, C. Álvarez, P. Osorio-Vargas, L.E. Arteaga-Pérez, J. Norambuena-Contreras, Asphalt pyro-rejuvenators based on waste tyres: An approach to improve the rheological and self-healing properties of aged binders, J. Clean. Prod. 452 (2024) 142179. https://doi.org/10.1016/J.JCLEPRO.2024.142179.

[68] J.B. Sharmeen, F.M. Mahomoodally, G. Zengin, F. Maggi, D. Montesano, R. Petrelli, molecules Essential Oils as Natural Sources of Fragrance Compounds for Cosmetics and Cosmeceuticals, (2021). https://doi.org/10.3390/molecules26030666.

[69] S.A. Groves, R.S. Lehrle, M. Blazsó, T. Székely, Natural rubber pyrolysis: Study of temperature-and thickness-dependence indicates dimer formation mechanism, J. Anal. Appl. Pyrolysis 19 (1991) 301–309. https://doi.org/10.1016/0165-2370(91)80051-9.

[70] Y. Zhang, G. Ji, A. Li, Production of limonene epoxides from tire pyrolysis oil by polyoxometalate immobilized on SBA-15, Process Safety and Environmental Protection 178 (2023) 287–295. https://doi.org/10.1016/J.PSEP.2023.08.018.

[71] Y. Zhang, S. Cheng, G. Ji, A. Li, Refinement of limonene epoxides from the light distillate of tire pyrolysis oil via catalytic epoxidation, Sep. Purif. Technol. 319 (2023) 124068. https://doi.org/10.1016/J.SEPPUR.2023.124068.

[72] V. Toteva, K. Stanulov, Waste tires pyrolysis oil as a source of energy: Methods for refining, Progress in Rubber, Plastics and Recycling Technology 36 (2019) 143–158. https://doi.org/10.1177/1477760619895026.

[73] B. Qu, Y.S. Zhang, T. Wang, H.S. Choi, Y. Zhang, Z. Fu, A. Li, G. Ji, Pyrolysis-catalysis of waste tire to enhance the aromatics selectivity via metal-modified ZSM-5 catalysts, Process Safety and Environmental Protection 190 (2024) 138–148. https://doi.org/10.1016/J.PSEP.2024.07.041.

[74] A.M. Ramírez Arias, J.C. Moreno-Piraján, L. Giraldo, Kinetic Study of Waste Tire Pyrolysis Using Thermogravimetric Analysis, ACS Omega 7 (2022) 16298–16305. https://doi.org/10.1021/acsomega.1c06345.

[75] J. Nisar, G. Ali, A. Shah, Z.H. Farooqi, R.A. Khan, M. Iqbal, M. Gul, Pyrolysis of waste tire rubber: a comparative kinetic study using different models, Energy Sources, Part A: Recovery, Utilization, and Environmental Effects (2020) 1–11. https://doi.org/10.1080/15567036.2020.1823530.

[76] V. Mortezaeikia, O. Tavakoli, M.S. Khodaparasti, A review on kinetic study approach for pyrolysis of plastic wastes using thermogravimetric analysis, J. Anal. Appl. Pyrolysis 160 (2021) 105340. https://doi.org/10.1016/J.JAAP.2021.105340.

[77] S.L. Narnaware, N.L. Panwar, Kinetic study on pyrolysis of mustard stalk using thermogravimetric analysis, Bioresour. Technol. Rep. 17 (2022) 100942. https://doi.org/10.1016/J.BITEB.2021.100942.

[78] ASTM International, Standard Test Methods for Instrumental Determination of Carbon, Hydrogen, and Nitrogen in Petroleum Products and Lubricants, West Conshohocken, PA, 2016.

[79] ASTM International, Standard Practice for Proximate Analysis of Coal and Coke, West Conshohocken, PA, 2013.

[80] S.A. Iwarere, N.M. Mkhize, Pyrolysis of various tyre types: Characteristics and kinetic studies using thermogravimetric analysis, Detritus 9 (2020) 165–173. https://doi.org/10.31025/2611-4135/2019.13870.

[81] N.M. Mkhize, P. van der Gryp, B. Danon, J.F. Görgens, Effect of temperature and heating rate on limonene production from waste tyre pyrolysis, J. Anal. Appl. Pyrolysis 120 (2016) 314–320. https://doi.org/10.1016/J.JAAP.2016.04.019.

[82] A.D. Paulsen, M.S. Mettler, P.J. Dauenhauer, The Role of Sample Dimension and Temperature in Cellulose Pyrolysis, Energy & Fuels 27 (2013) 2126–2134. https://doi.org/10.1021/ef302117j.

[83] B. Klemetsrud, J. Klinger, E. Bar Ziv, D. Shonnard, A kinetic study of the fast micro-pyrolysis of hybrid poplar, J. Anal. Appl. Pyrolysis 128 (2017) 353–362. https://doi.org/10.1016/J.JAAP.2017.09.014.

[84] P. Osorio-Vargas, I.D. Lick, · Felipe Sobrevía, D. Correa-Muriel, T. Menares, R. Manrique, M.L. Casella, · Luis, E. Arteaga-Pérez, Thermal Behavior, Reaction Pathways and Kinetic Implications of Using a Ni/SiO 2 Catalyst for Waste Tire Pyrolysis, Waste Biomass Valorization 12 (2021) 6465–6479. https://doi.org/10.1007/s12649-021-01494-y.

[85] R. Pascual, M. Román, M. López-Campos, M. Hitch, E. Rodovalho, Reducing mining footprint by matching haul fleet demand and route-oriented tire types, J. Clean. Prod. 227 (2019) 645–651. https://doi.org/10.1016/j.jclepro.2019.04.069.

[86] L.E. Arteaga-Pérez, S. Larrere, M. Chávez-Delgado, Y.J. Rueda Ordoñez, J.L. Concha, C. Segura, J. Norambuena-Contreras, Y. Casas-Ledón, Environmental life cycle assessment of encapsulated rejuvenators from mining truck waste tires via pyrolysis for asphalt self-healing, J. Clean. Prod. 490 (2025) 144787. https://doi.org/10.1016/j.jclepro.2025.144787.

[87] J. Poblete, R. Jiménez, F. Ronsse, S. Ghysels, L.E. Arteaga-Pérez, Understanding limonene synthesis from waste tire pyrolysis through a kinetics-based perspective, J. Anal. Appl. Pyrolysis 191 (2025) 107207. https://doi.org/10.1016/J.JAAP.2025.107207.

[88] J.A. Dávila, M. Rosenberg, C.A. Cardona, Techno-economic and Environmental Assessment of p-Cymene and Pectin Production from Orange Peel, Waste Biomass Valorization Volume 6 (2015) 253–261. https://doi.org/10.1007/s12649-014-9339-y.

[89] A. Satira, C. Espro, E. Paone, P. Calabrò, M. Pagliaro, R. Ciriminna, F. Mauriello, The Limonene Biorefinery: From Extractive Technologies to Its Catalytic Upgrading into p-Cymene, Catalysts 11 (2021) 387. https://doi.org/10.3390/catal11030387.

[90] S.L. Soled, A. Malek, S. Miseo, J. Baumgartner, C. Kliewer, M. Afeworki, P.A. Stevens, Supported Metal Catalysts: Some Interesting New Leads In An Old Field, Stud. Surf. Sci. Catal. 162 (2006) 103–110. https://doi.org/10.1016/S0167-2991(06)80896-7.

[91] G. Papapolymerou, V. Bontozoglou, Decomposition of NH3 on Pd and Ir Comparison with Pt and Rh, J. Mol. Catal. A Chem. 120 (1997) 165–171. https://doi.org/10.1016/S1381-1169(96)00428-1.

[92] A. Amano, H. Taylor, The decomposition of ammonia on ruthenium, rhodium and palladium catalysts supported on alumina, J. Am. Chem. Soc. 76 (1954) 4201–4204. https://doi.org/https://doi.org/10.1021/ja01645a057.

[93] M. Ortega, D. Gómez, R. Manrique, G. Reyes, J. Tatiana García-Sánchez, V. Gabriel, B. Medrano, R. Jiménez, L.E. Arteaga-Pérez, Reductive amination of phenol over Pd-based catalysts: elucidating the role of the support and metal nanoparticle size †, Cite This: React. Chem. Eng 8 (2023) 47. https://doi.org/10.1039/d2re00259k.

[94] R. Liu, Y. Bian, W. Dai, Qualitative and quantitative analysis of Brønsted and Lewis acid sites in zeolites: A combined probe-assisted 1H MAS NMR and NH3-TPD investigation, Chin. J. Struct. Chem. 43 (2024) 100250. https://doi.org/10.1016/J.CJSC.2024.100250.

[95] B.S. Institution, Determination of the Specific Surface Area of Powders. Recommendations for Methods of Determination of Metal Surface Area Using Gas Adsorption Techniques, BSI, London, 1995.

[96] G. Ertl, H. Knözinger, F. Schüth, J. Weitkamp, Handbook of Heterogeneous Catalysis, 2nd ed., Wiley-VCH, 2008. https://doi.org/10.1002/9783527610044.

[97] X. Wang, Y. Zhu, H. Huang, Y. Zhao, H. Dai, X. Zhang, T. Zheng, J. Ma, C. Wang, D. Yang, P. Ning, Morphology Effects on Structure-Activity Relationship of Pd/Y-ZrO 2 Catalysts for Methane Oxidation, Catalysts (MDPI) (2022). https://doi.org/10.3390/catal12111420.

[98] J.T. Scanlon, D.E. Willis, Calculation of Flame Ionization Detector Relative Response Factors Using the Effective Carbon Number Concept, J. Chromatogr. Sci. 23 (1985). https://doi.org/10.1093/CHROMSCI/23.8.333.

[99] M.A. Vannice, Kinetics of Catalytic Reactions, Springer US, 2006. https://doi.org/10.1007/b136380.

[100] S. Park, J.G. Seo, J.C. Jung, S.H. Baeck, T.J. Kim, Y.M. Chung, S.H. Oh, I.K. Song, Direct synthesis of hydrogen peroxide from hydrogen and oxygen over palladium catalysts supported on TiO2–ZrO2 mixed metal oxides, Catal. Commun. 10 (2009) 1762–1765. https://doi.org/10.1016/J.CATCOM.2009.05.026.

[101] M. Thommes, K. Kaneko, A. V Neimark, J.P. Olivier, F. Rodriguez-Reinoso, J. Rouquerol, K.S.W. Sing, Physisorption of gases, with special reference to the evaluation of surface area and pore size distribution (IUPAC Technical Report), 87 (2015) 1051–1069. https://doi.org/doi:10.1515/pac-2014-1117.

[102] X. Wang, Z. Rui, Y. Zeng, H. Ji, Z. Du, Q. Rao, Synergetic effect of oxygen vacancy and Pd site on the interaction between Pd/Anatase TiO2(101) and formaldehyde: A density functional theory study, Catal. Today 297 (2017) 151–158. https://doi.org/10.1016/J.CATTOD.2017.06.037.

[103] Z.-S. Huang, Y.-F. Wang, M.-Y. Qi, M. Conte, Z.-R. Tang, Y.-J. Xu, Interface Synergy of Exposed Oxygen Vacancy and Pd Lewis Acid Sites Enabling Superior Cooperative Photoredox Synthesis, Angewandte Chemie 136 (2024) e202412707. https://doi.org/https://doi.org/10.1002/ange.202412707.

[104] C.A. González, A.N. Ardila, C. Montes De Correa, M.A. Martínez, G. Fuentes-Zurita, Pd/TiO2 Washcoated Cordierite Minimonoliths for Hydrodechlorination of Light Organochlorinated Compounds, Ind. Eng. Chem. Res. 46 (2007). https://doi.org/10.1021/ie070713r.

[105] G. Busca, Metal Catalysts for Hydrogenations and Dehydrogenations, Heterogeneous Catalytic Materials (2014) 297–343. https://doi.org/10.1016/B978-0-444-59524-9.00009-2.

[106] D. Buhl, P.A. Weyrich, W.M.H. Sachtler, W.F. Hölderich, Support effects in the Pd catalyzed dehydrogenation of terpene mixtures to p-cymene, Appl. Catal. A Gen. 171 (1998) 1–11. https://doi.org/10.1016/S0926-860X(98)00039-8.

[107] D. Buhl, D.M. Roberge, W.F. Hölderich, Production of p-cymene from α-limonene over silica supported Pd catalysts, Appl. Catal. A Gen. 188 (1999) 287–299. https://doi.org/10.1016/S0926-860X(99)00219-7.

[108] C.M. Wang, Z.H. Liu, Y.K. Chen, J.M. Han, Y.L. Chen, M.M. Miao, H. Cao, An ab initio analysis of the Diels–Alder reaction between two isoprenes, Comput. Theor. Chem. 1017 (2013) 174–181. https://doi.org/10.1016/J.COMPTC.2013.05.023.

[109] H. Cui, J. Zhang, Z. Luo, C. Zhao, Mechanisms into dehydroaromatization of bio-derived limonene to: P -cymene over Pd/HZSM-5 in the presence and absence of H2, RSC Adv. 6 (2016) 66695–66704. https://doi.org/10.1039/c6ra17159a.

[110] D. Wang, X. Wei, S. Shou, J. Gong, Dealkylation in Fluid Catalytic Cracking Condition for Efficient Conversion of Heavy Aromatics to Benzene−Toluene−Xylene, ACS Omega 8 (2023). https://doi.org/10.1021/acsomega.2c06507.

[111] N.A. Comelli, E.N. Ponzi, M.I. Ponzi, Isomerization of α-pinene, limonene, α-terpinene, and terpinolene on sulfated zirconia, J. Am. Oil Chem. Soc. 82 (2005) 531–535. https://doi.org/10.1007/s11746-005-1105-2.

[112] P.T. Williams, A.J. Brindle, Catalytic pyrolysis of tyres: influence of catalyst temperature, Fuel 81 (2002) 2425–2434. https://doi.org/10.1016/S0016-2361(02)00196-5.

[113] G. Galdames, P. Santander, R. Jiménez, A. Karelovic, A detailed kinetic model for the methanol oxidative dehydrogenation on vanadia-based catalysts: Aggregation state role and active site requirements, Appl. Catal. A Gen. 682 (2024) 119807. https://doi.org/https://doi.org/10.1016/j.apcata.2024.119807.

[114] Z. Song, X. Wang, C. Chen, Y. Xu, Z. Wang, X. Wang, D. Liu, Stability and kinetics study of direct CO2 hydrogenation to aromatics over Cu-Fe2O3/HZSM-5-P bifunctional catalysts, Fuel 389 (2025) 134585. https://doi.org/https://doi.org/10.1016/j.fuel.2025.134585.

[115] S. Suzuki, J. Uchisawa, A. Obuchi, A. Yamamoto, T. Sakai, M. Nagata, M. Yoshimura, Comparative study of the reaction characteristics and kinetics of catalytic hydrogenation involving propylene, 1-butene, and their mixture over Pt/ZrO2, React. Kinet. Mech. Catal. 138 (2025) 1295–1310. https://doi.org/10.1007/s11144-024-02792-x.

[116] H. Fan, P.S.J. Lakey, E.S. Frank, D.J. Tobias, M. Shiraiwa, V.H. Grassian, Comparison of the Adsorption-Desorption Kinetics of Limonene and Carvone on TiO2 and SiO2 Surfaces

under Different Relative Humidity Conditions, J. Phys. Chem. C 126 (2022) 21253–21262. https://doi.org/10.1021/acs.jpcc.2c06853.

[117] C.T. Campbell, J.R. V Sellers, Enthalpies and Entropies of Adsorption on Well-Defined Oxide Surfaces: Experimental Measurements, Chem. Rev. 113 (2013) 4106–4135. https://doi.org/10.1021/cr300329s.

[118] L. Chen, R.S. Smith, B.D. Kay, Z. Dohnálek, Adsorption of small hydrocarbons on rutile TiO2 (110), Surf. Sci. 650 (2016) 83–92. https://doi.org/https://doi.org/10.1016/j.susc.2015.11.002.

[119] S.A. Ali, K.E. Ogunronbi, S.S. Al-Khattaf, Kinetics of dealkylation–transalkylation of C9 alkyl-aromatics over zeolites of different structures, Chem. Eng. Res. Des. 91 (2013) 2601–2616. https://doi.org/10.1016/J.CHERD.2013.04.014.

[120] K. Wang, T. Shan, B. Li, Y. Zheng, H. Xu, C. Wang, X. Tian, Study on pyrolysis characteristics, kinetics and thermodynamics of waste tires catalytic pyrolysis with low-cost catalysts, Fuel 356 (2024) 129644. https://doi.org/10.1016/J.FUEL.2023.129644.

[121] B. Qu, A. Li, Y. Qu, T. Wang, Y. Zhang, X. Wang, Y. Gao, W. Fu, G. Ji, Kinetic analysis of waste tire pyrolysis with metal oxide and zeolitic catalysts, J. Anal. Appl. Pyrolysis 152 (2020) 104949. https://doi.org/10.1016/J.JAAP.2020.104949.

[122] Matweb, Natural Rubber, Vulcanized (NR, IR, Polyisoprene), (2023). https://www.matweb.com/search/datasheet_print.aspx?matguid=6588439546ac4492965c894ddff3f5da (accessed December 10, 2023).

[123] G. SriBala, H.-H. Carstensen, K.M. Van Geem, G.B. Marin, Measuring biomass fast pyrolysis kinetics: State of the art, WIREs Energy and Environment 8 (2019) e326. https://doi.org/https://doi.org/10.1002/wene.326.

APPENDICES

Appendix: Chapter 2

A-2.1. Elemental and proximate composition of MTWT and physicochemical properties of natural rubber.

Table A-2. 1. Physicochemical properties of mining truck waste tires, natural rubber, butadiene rubber, and styrene-butadiene rubber.

Samples	Proximate analysis (wt.%)				Ultimate analysis*				
	Moisture	Volatile matter	Ash	Fixed Carbon	C (%)	N (%)	H (%)	S (%)	O** (%)
Natural Rubber	0.93	99.19	0.59	0.22	85.97	0,0	10.27	0.0	3.76
Butadiene Rubber	0.45	100	0.0	0.0	88.51	0.0	9.89	0.0	1.60
Styrene-Butadiente Rubber	0.65	100	0.0	0.0	87.15	0.0	8.90	0.0	3.95
Mining Truck Waste Tires	0.99	67.20	13.10	18.71	76.50	0.44	7.10	1.50	14.46

*Dry basis, ash-free.

** Oxygen content was calculated by difference from the measured elemental composition

The higher heating value (HHV) of the Mining Truck Waste Tires was reported as 33.5 MJ/kg.

Table A-2. 2. Physicochemical properties of natural rubber.

Physicochemical properties	Value	References
ρ [kg · m^{-3}]	920	(-)
C_p [J · kg^{-1} · K^{-1}]	440	[122]
λ [W · m^{-1} · K^{-1}]	0.150	
h [W · m^{-2} · K^{-1}]	2000	[45]

A-2.2. Transport limitations during pyrolysis of NR

To elucidate the rate constant (k) associated with solid decomposition, various kinetic models were investigated across a range of temperatures. The best model fitting to the data was **1-D diffusion model:**

$$\frac{d\alpha}{dt} = k \cdot \left(\frac{1}{2 \cdot \alpha}\right)$$

Here, α corresponds to the conversion of natural rubber and is calculated as the fractional weight difference between the initial mass of natural rubber (m_o) and the mass remaining after pyrolysis $\big(m(t)\big)$:

$$\alpha = \frac{m_o - m(t)}{m_o}$$

And the rate constant (k):

$$k = A_O \cdot \exp\left(-\frac{E_a}{R \cdot T}\right)$$

Where (E_a) is the activation energy and A_o is the pre-exponential factor.

This model was implemented in MATLAB® to solve the differential equation analytically, and rate constants were subsequently estimated using the **lsqcurvefit** function, which minimizes the following error function.

$$error = \sum_{i} \left(\alpha_{i,model} - \alpha_{i,exp}\right)^2$$

Table A-2. 3. Fitting model parameters with corresponding correlation coefficients

Parameters	**Values**	$\boldsymbol{R^2}$
$k\ (400°C)$	0.0010	0.8420
$k\ (450°C)$	0.0044	0.9644
$k\ (500°C)$	0.0102	0.9602
E_a [kJ/mol]	99.69	0.9872*

*Coefficient correlation in Arrhenius plot

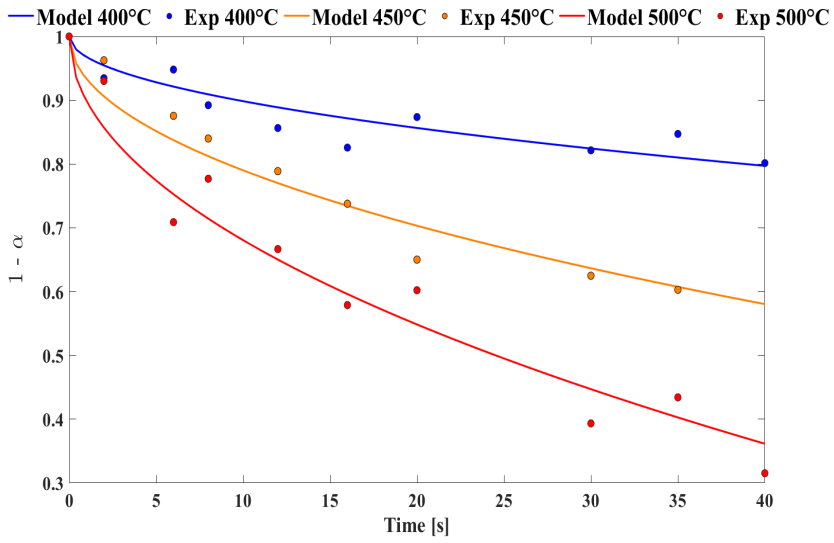

Figure A-2. 1. Kinetic model and experimental data for solid degradation NR by pyrolysis.

The information regarding the numbers as Py^{I}, Py^{II}, and Biot can be graphically represented. This graph allows for the differentiation of various zones corresponding to the regime that controls the pyrolysis process [123]. In Figure A-2.2, Py^{I}, Py^{II}, and Biot were calculated, considering the Natural Rubber properties presented in Table A-2.3 and the calculated k(500°C).

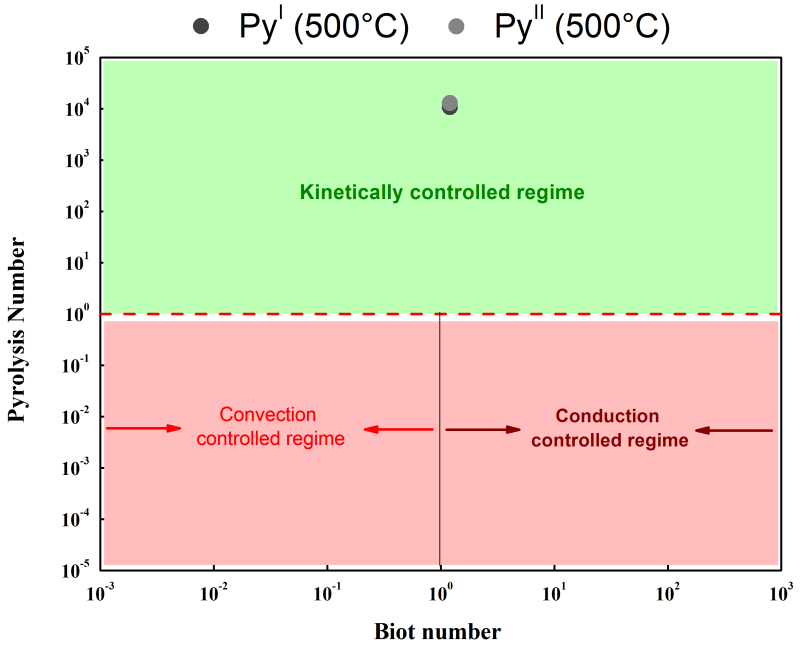

Figure A-2. 2. Thermal mapping of Py-GC/MS experiments at 500°C.

Table A-2. 4. Values were calculated for the dimensionless number at each temperature.

Dimensionless Number	**Temperature**		
	400°C	**450°C**	**500°C**
$\boldsymbol{Bi}$	1.125		
$\boldsymbol{P_y^I}$	56944	11827	5107
$\boldsymbol{P_y^{II}}$	50617	13305	5745

A-2.2. Calibration curves

Table A-2. 5. Calibration curves for limonene with respective concentration range and correlation coefficient.

Range moles of limonene $[\boldsymbol{\mu mol \cdot 10^{-4}}]$	$\mathbf{R^2}$ $[-]$	**Figure**
1.16 – 5.82	0.981	A-2.2
5.82 – 58.2	0.999	A-2.3
58.2 - 291	0.996	A-2.4
291 – 1,454	0.990	A-2.5

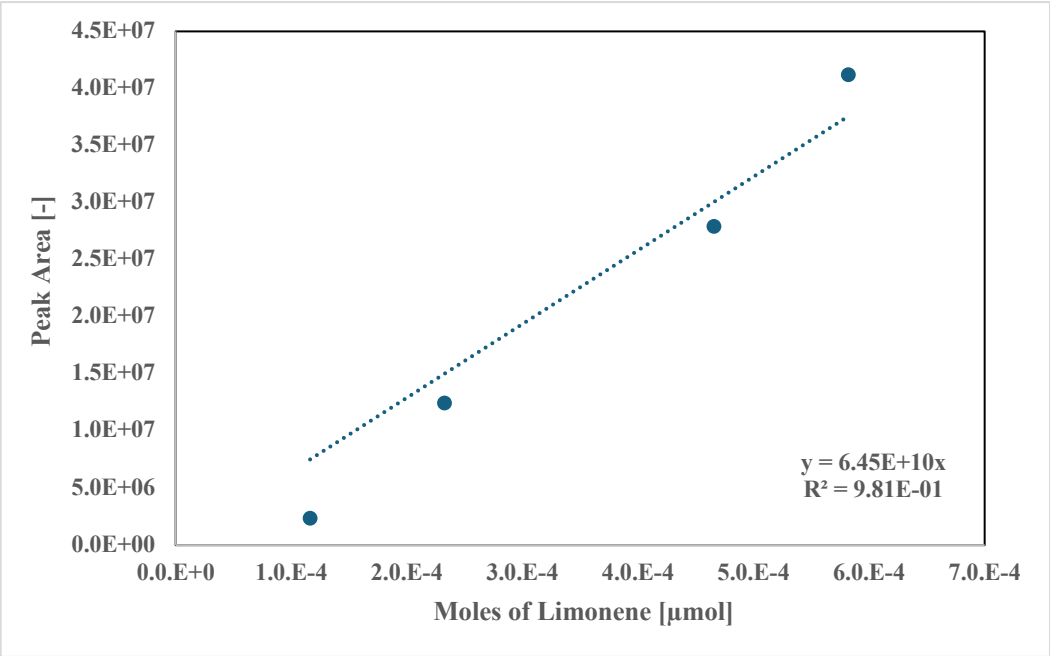

Figure A-2. 3. Plot of the limonene calibration curve for 1.16 – 5.82 [µmol · 10^{-4}].

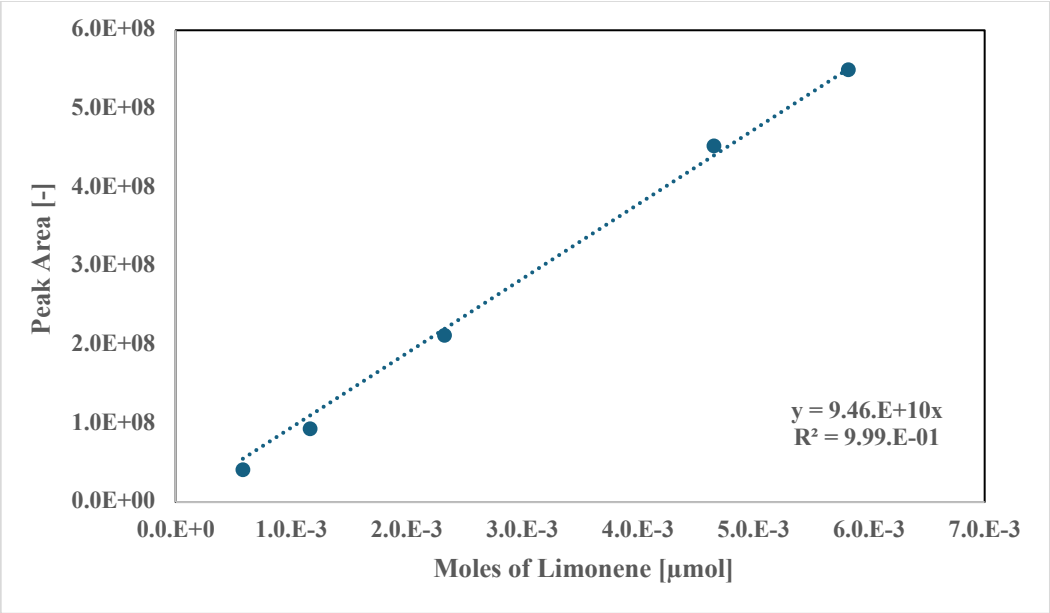

Figure A-2. 4. Plot of the limonene calibration curve 5.82 – 58.2 [µmol · 10^{-4}].

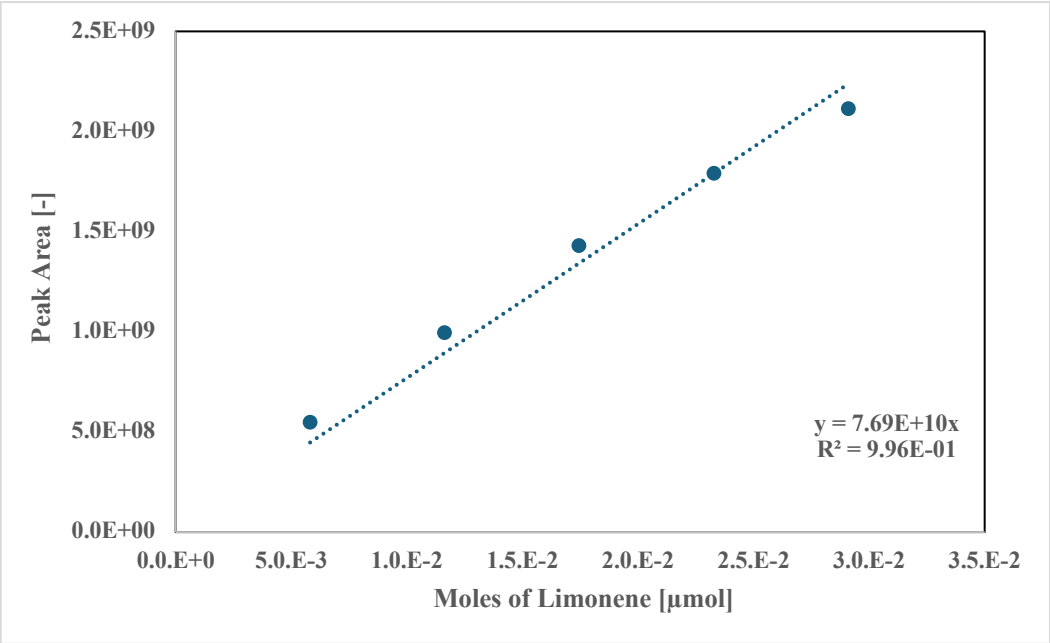

Figure A-2. 5. Plot of the limonene calibration curve for 58.2 – 291 [µmol · 10^{-4}].

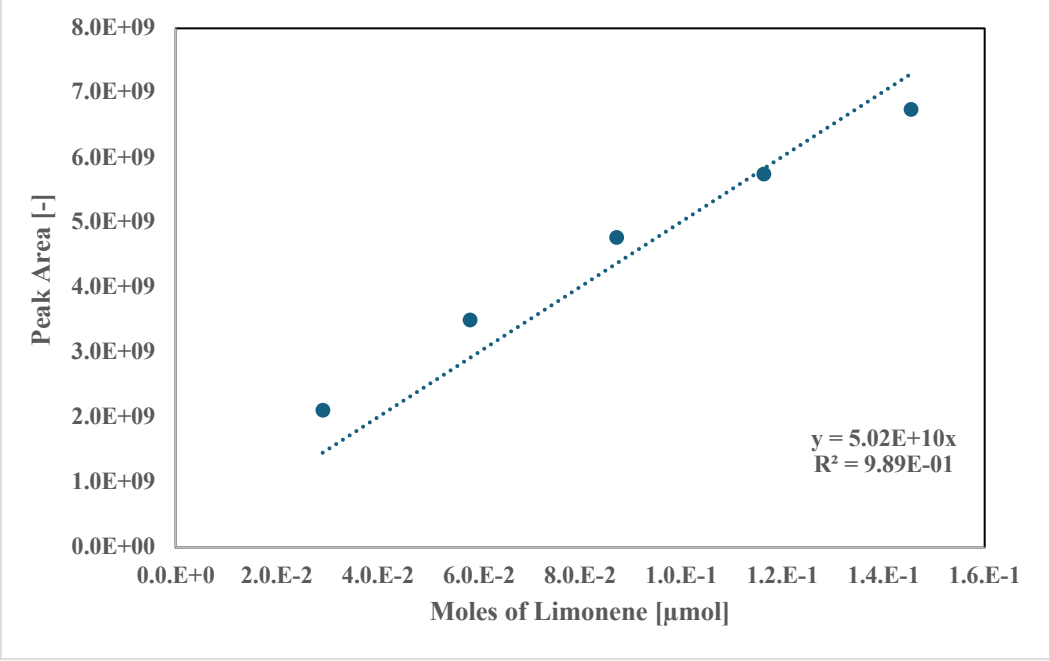

Figure A-2. 6. Plot of the limonene calibration curve for 291 – 1,454 [µmol · 10^{-4}].

A-2.4. Analysis of limonene generation by fast pyrolysis of NR

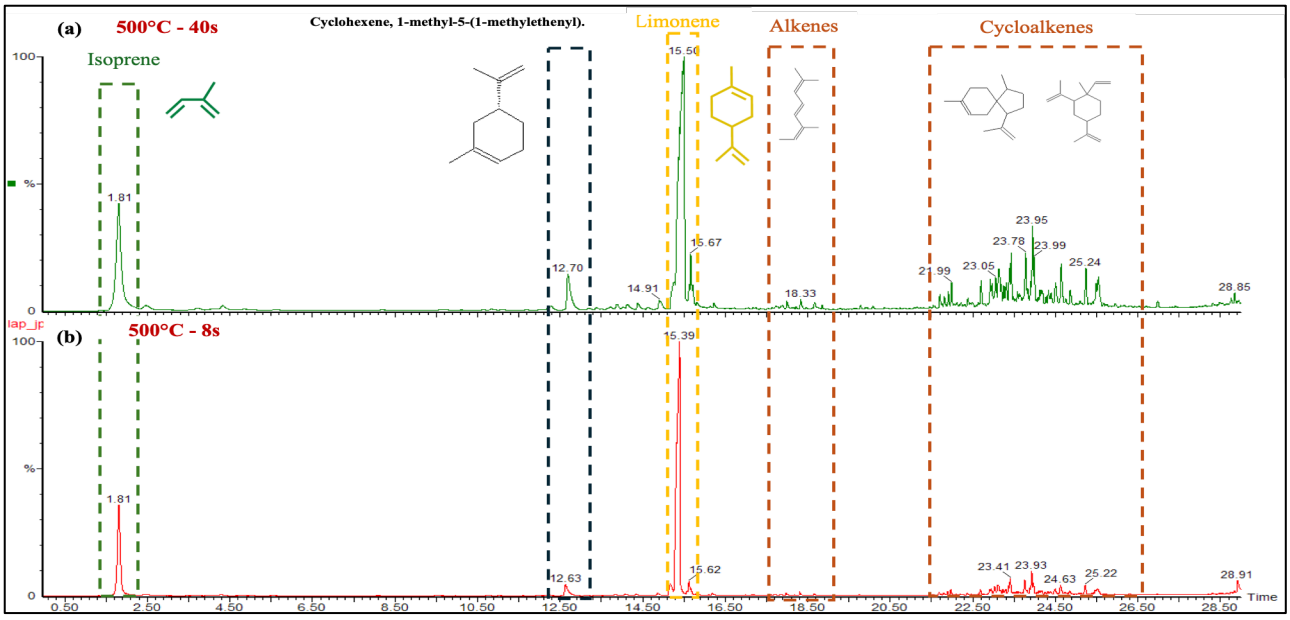

Figure A-2. 7. Chromatogram obtained by Py-GC/MS at 500°C - 40s and 500°C - 8s under a helium flow rate of 1 mL/min.

Table A-2. 6. Selectivity values obtained for limonene, isoprene, Cyclo- and alkenes at 400°C - 40s and 500°C - 30s.

Temperature [°C]	Time [s]	Selectivity [%]		
		Limonene	Isoprene	Cyclo- and alkenes
400	40	65.82	14.50	19.67
500	30	46.14	21.34	32.52

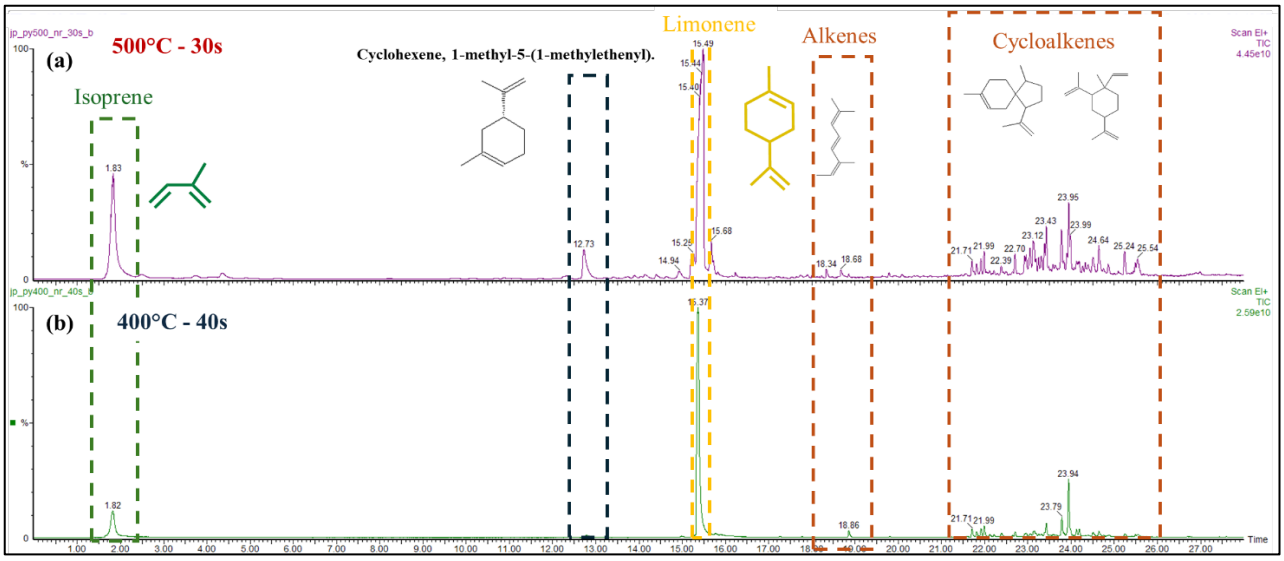

Figure A-2. 8. Chromatogram obtained by Py-GC/MS at 400°C - 40s and 500°C - 30s under a helium flow rate of 1 mL/min.

Table A-2. 7. Moles of limonene generated for an unreacted fraction of 80% at 400°C, 450°C y 500°C.

1 - X	Temperature [°C]	Time [s]	N_L [µmol]
0.8	400	23	0.01137
	450	12	0.03147
	500	8	0.08796

A-2.5. Kinetic Models

Table A-2. 8. Values of rate constants calculated for Model 1.

Rate constants	400°C	450°C	500°C
$\mathbf{k_1}$	$1.14 \cdot 10^{-4}$	$8.96 \cdot 10^{-4}$	$7.30 \cdot 10^{-3}$
$\mathbf{k_2}$	$9.75 \cdot 10^{-5}$	$2.98 \cdot 10^{-4}$	$1.15 \cdot 10^{-1}$

$\mathbf{k_3}$	$9.48 \cdot 10^{-3}$	$1.85 \cdot 10^{-2}$	$2.24 \cdot 10^{-2}$
$\mathbf{k_4}$	$8.42 \cdot 10^{-4}$	$2.03 \cdot 10^{-3}$	$4.94 \cdot 10^{-2}$
$\mathbf{k_5}$	$9.45 \cdot 10^{-5}$	$8.06 \cdot 10^{-4}$	$1.15 \cdot 10^{-1}$

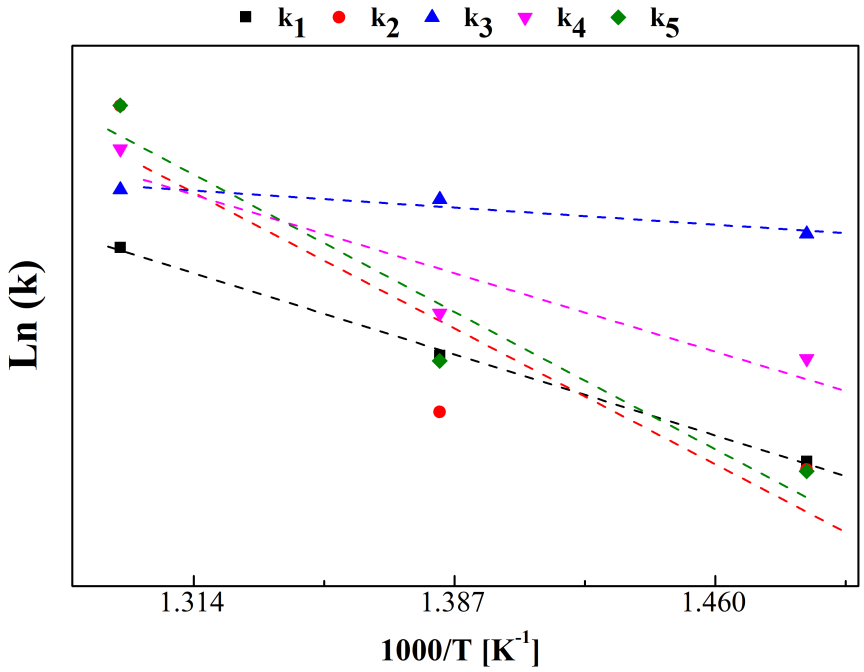

Figure A-2. 9. Arrhenius plot for Model 1.

Table A-2. 9. Values of rate constants calculated for Model 2.

Rate constants	400°C	450°C	500°C
$\boldsymbol{k_1}$	$1.12 \cdot 10^{-4}$	$1.01 \cdot 10^{-3}$	$5.83 \cdot 10^{-3}$
$\boldsymbol{k_2}$	$8.03 \cdot 10^{-4}$	$3.42 \cdot 10^{-2}$	$1.20 \cdot 10^{-1}$
$\boldsymbol{k_3}$	$7.02 \cdot 10^{-3}$	$1.63 \cdot 10^{-2}$	$2.39 \cdot 10^{-2}$

k_4	$1.58 \cdot 10^{-3}$	$5.08 \cdot 10^{-3}$	$2.58 \cdot 10^{-2}$

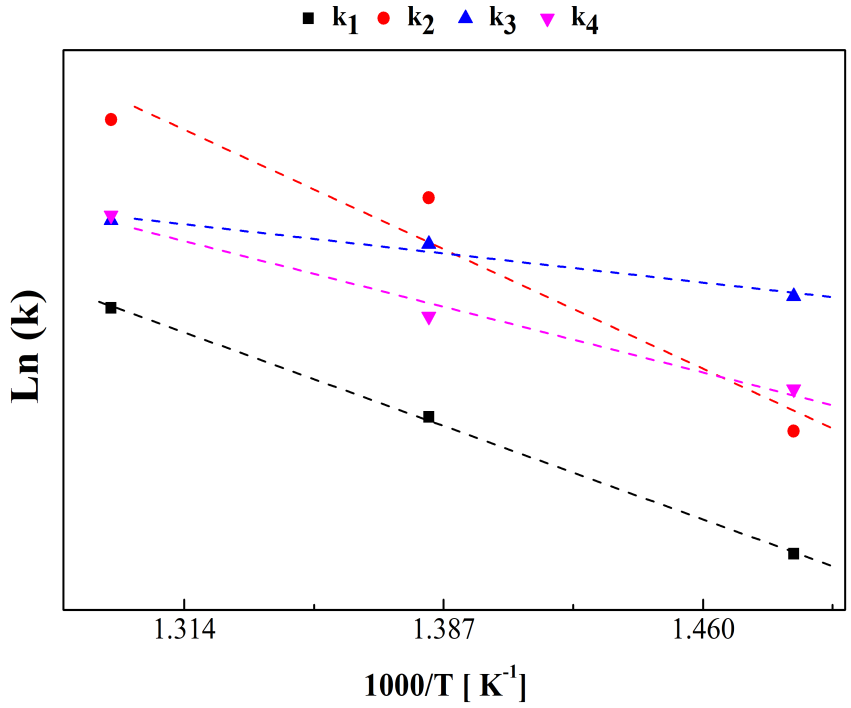

Figure A-2. 10. Arrhenius plot for Model 2.

Table A-2. 10. Reaction steps and mole balance equations for Model 3.

Reaction Steps		Mole balances
$NR \xrightarrow{k_1} L$	(i)	$\frac{dN_{NR}}{dt} = -k_1 \cdot N_{NR} - k_3 \cdot N_{NR}$
$L \xrightarrow{k_2} P$	(ii)	$\frac{dN_L}{dt} = k_1 \cdot N_{NR} - k_2 \cdot N_L - k_5 \cdot N_L$

$NR \xrightarrow{k_3} 2I$	(iii)	$\frac{dN_I}{dt} = k_3 \cdot N_{NR} + k_5 \cdot N_L$
$L \xrightarrow{k_5} 2I$	(v)	

Table A-2. 11. Values of rate constants calculated for Model 3.

Rate constants	**400°C**	**450°C**	**500°C**
$\boldsymbol{k_1}$	$1.86 \cdot 10^{-4}$	$1.42 \cdot 10^{-3}$	$4.46 \cdot 10^{-3}$
$\boldsymbol{k_2}$	$\mathbf{1.86 \cdot 10^{-4}}$	$\mathbf{6.06 \cdot 10^{-14}}$	$\mathbf{2.70 \cdot 10^{-3}}$
$\boldsymbol{k_3}$	$6.41 \cdot 10^{-3}$	$1.58 \cdot 10^{-2}$	$2.52 \cdot 10^{-2}$
$\boldsymbol{k_5}$	$\mathbf{1.85 \cdot 10^{-4}}$	$\mathbf{8.04 \cdot 10^{-15}}$	$\mathbf{3.85 \cdot 10^{-3}}$

Appendix: Chapter 3

A-3.1. Calibration curves and quantification of products

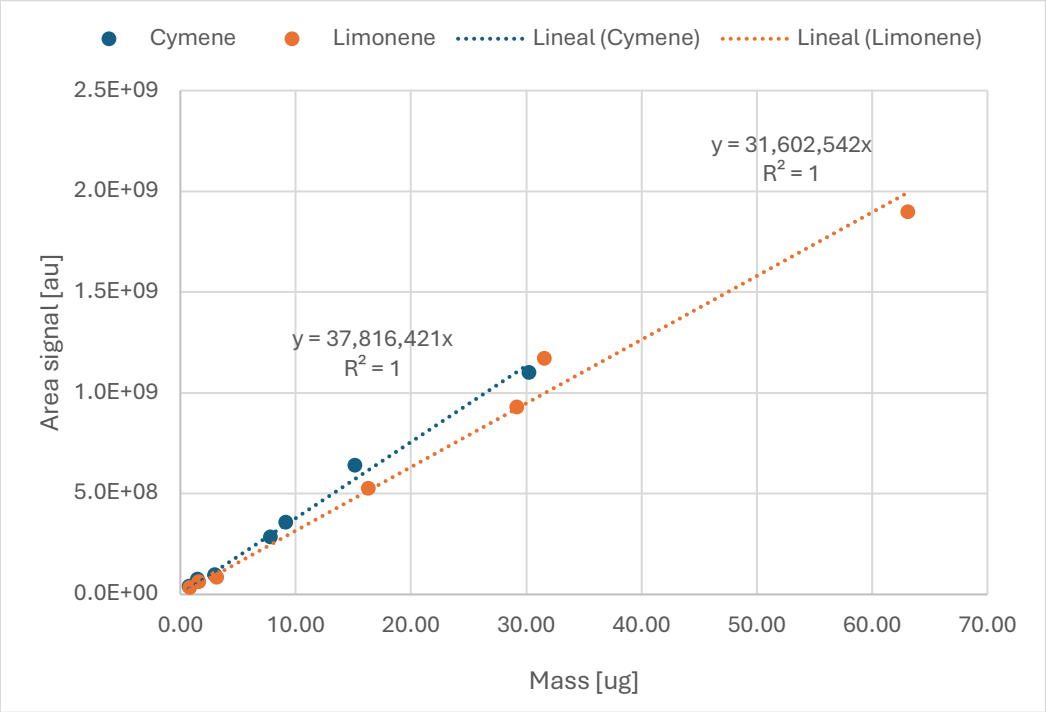

Figure A-3. 1. Calibration curves for limonene (orange) and p-cymene (blue) obtained by GC–FID. The peak area (arbitrary units) is plotted against injected mass (µg). Linear regression equations are displayed for each compound, showing excellent correlation ($R^2 = 1.0$). These calibration functions were used for the quantitative determination of limonene and p-cymene in pyrolysis–catalysis experiments

Table A-3. 1. Slopes from calibration and effective carbon number (ECN) assignments used for quantification of limonene, cymene, and other pyrolysis products. Response factors (F) were calculated from the ECN method considering the contribution of different carbon types.

Compounds	Slope (Area/mass)	ECN	F (R-Molar)	Aliphatic carbon	Aromatic carbon	Olefinic carbon	Acetylenic carbon	Carbonyl carbon	Carboxyl carbon	1° Alcohol	2° Alcohol
Limonene (Standard)	**31602542**	**9.8**	**1**	**6**	**0**	**4**	**0**	**0**	**0**	**0**	**0**
1,3-Cyclohexadiene, 1-methyl-4-(1-methylethyl)-	31602542	**9.8**	1	6	0	4	0	0	0	0	0
Cyclohexene, 3-methyl-6-(1-methylethylidene)-	31602542	**9.8**	1	6	0	4	0	0	0	0	0
Cyclohexene, 1-methyl-4-(1-methylethylidene)-	31602542	**9.8**	1	6	0	4	0	0	0	0	0
γ-Terpinene	31602542	**9.8**	1	6	0	4	0	0	0	0	0
Isoprene	15478796	4.8	2.04	1	0	4	0	0	0	0	0
Cyclohexene, 1-methyl-5-(1-methylethenyl)-	31602542	9.8	1	6	0	4	0	0	0	0	0
Bicyclo[4.1.0]heptane, 7-(1-methylethylidene)-	31925017	9.9	0.99	8	0	2	0	0	0	0	0
Cymene (Standard)	**37816421**	**10**	**1**	**4**	**6**	**0**	**0**	**0**	**0**	**0**	**0**
p-Xylene	30253136.8	8	1.25	2	6	0	0	0	0	0	0
Toluene	26471494.8	7	1.43	1	6	0	0	0	0	0	0
p-Cymenene	37438256.8	9.9	1.01	2	6	2	0	0	0	0	0

A-3.2. Supports screening and catalyst characterization

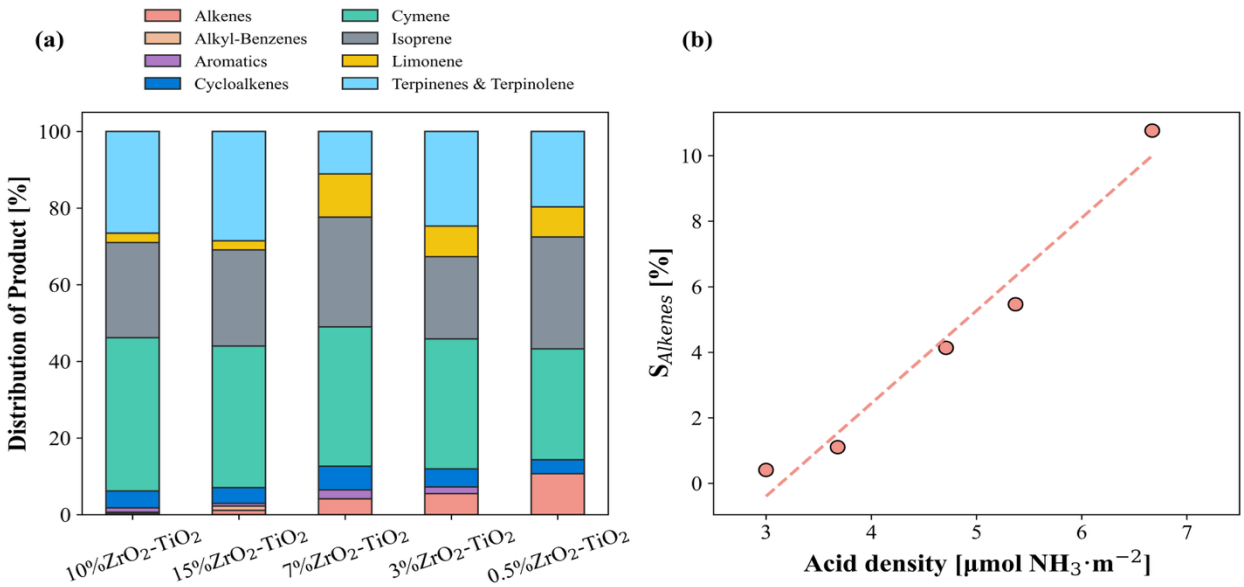

Figure A-3. 2. (a) Product distribution obtained during the ex-situ catalytic upgrading of limonene-rich pyrolytic vapors over Zr-modified TiO_2 supports. (b) Selectivity to alkenes, used as a diagnostic marker for acid-catalyzed cracking pathways, plotted as a function of acid density of supports. All experiments were conducted under identical ex-situ conditions (400 °C, 30 s, catalyst/NR = 10).

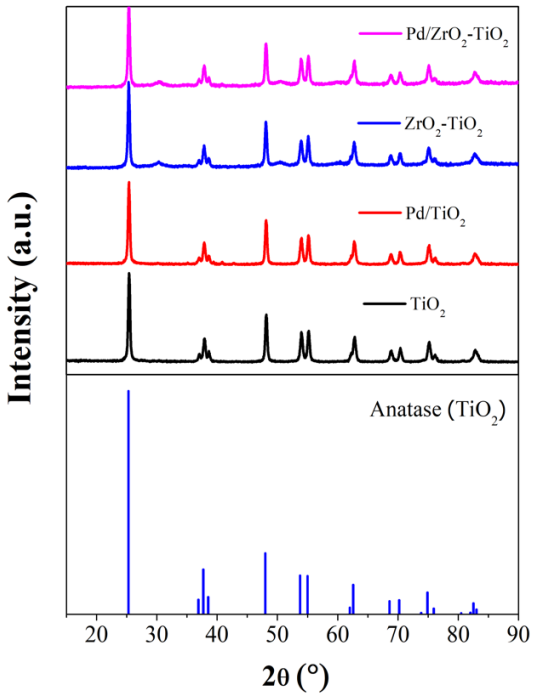

Figure A-3. 3. XRD patterns of TiO_2, Pd/TiO_2, ZrO_2 –TiO_2, and Pd/ZrO_2–TiO_2 catalysts. Characteristic peaks of anatase TiO_2 are indicated for comparison.

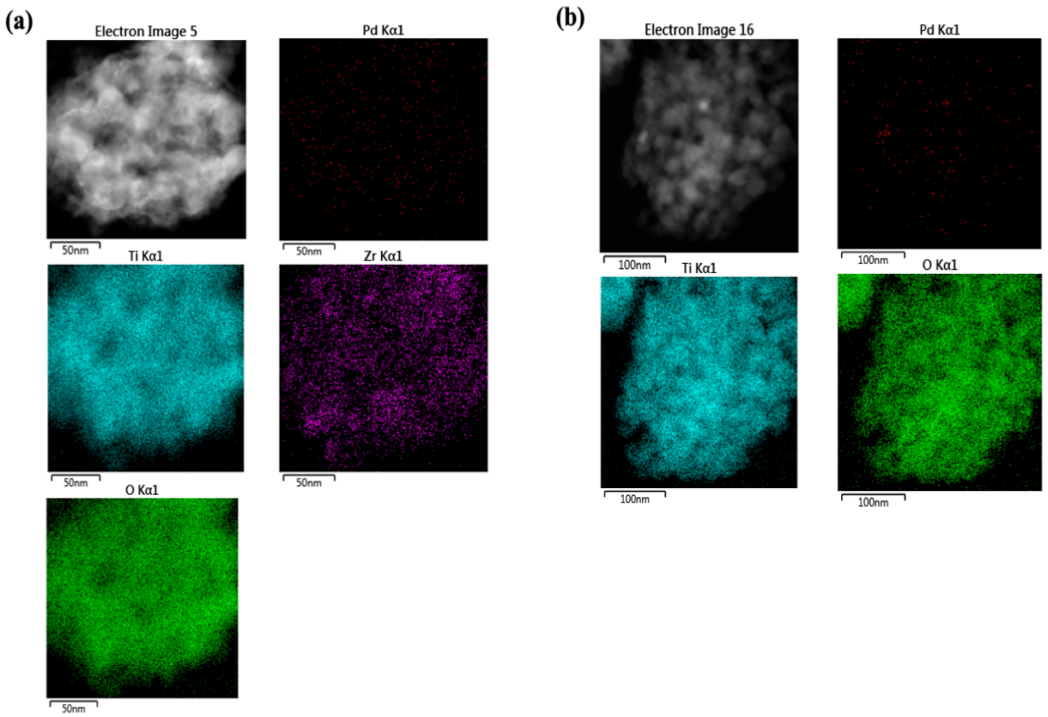

Figure A-3. 4. STEM–EDX elemental mapping of (a) $Pd/ZrO_2–TiO_2$ and (b) Pd/TiO_2 catalysts. The images confirm the homogeneous distribution of Pd nanoparticles over the oxide supports.

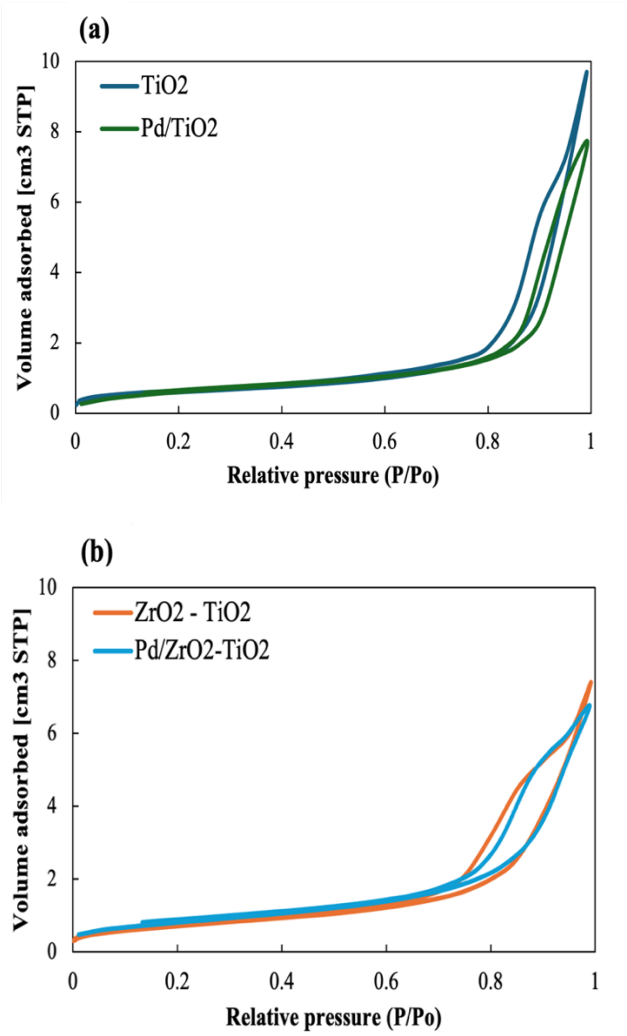

Figure A-3. 5. N_2 adsorption–desorption isotherms of (a) TiO_2 and Pd/TiO_2, and (b) ZrO_2–TiO_2 and Pd/ZrO_2–TiO_2. All samples exhibit type IV isotherms with H_2-type hysteresis loops, characteristic of mesoporous materials.

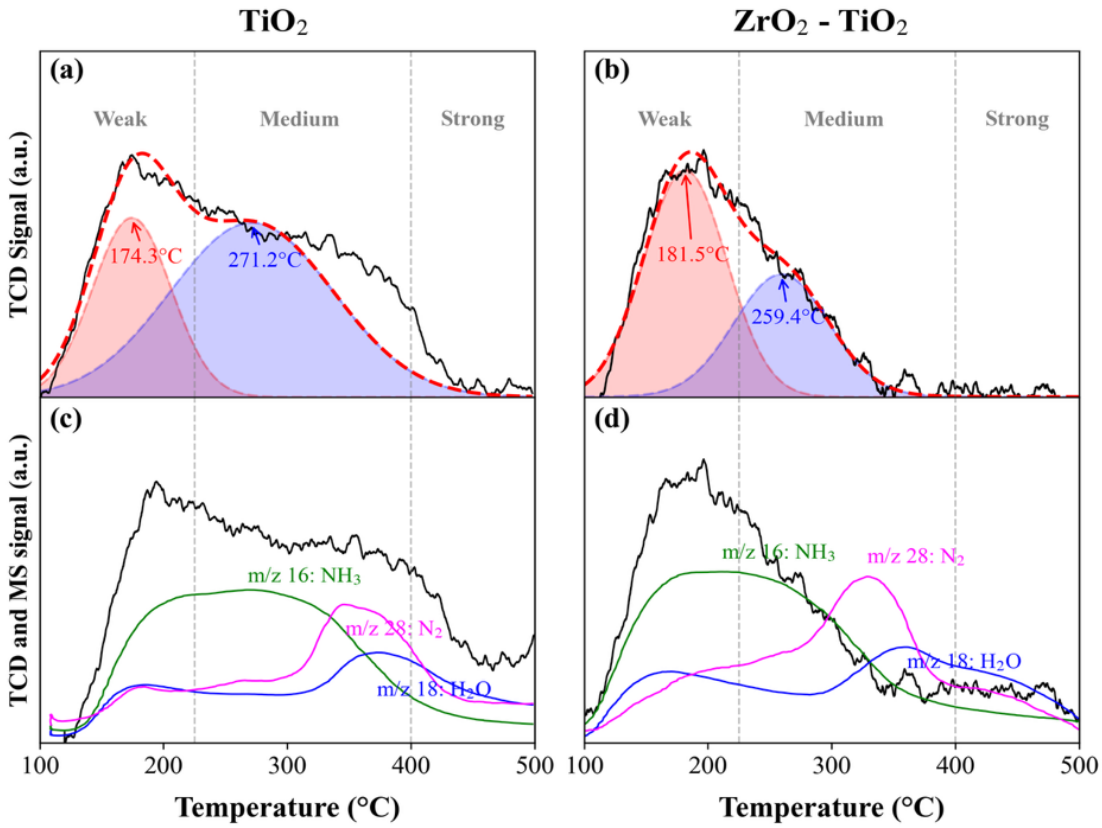

Figure A-3. 6. TPD – NH_3 results for TiO_2 (left column: (a) and (c)) and ZrO_2–TiO_2 (right column: (b) and (d)) catalysts. The first row shows the TCD signal as a function of temperature, while the second row combines the TCD signal with the mass spectrometric responses for NH_3, H_2O, and N_2. Vertical dashed lines indicate characteristic temperature regions corresponding to weak (T < 200°C), medium and strong (T > 200°C) acid sites.

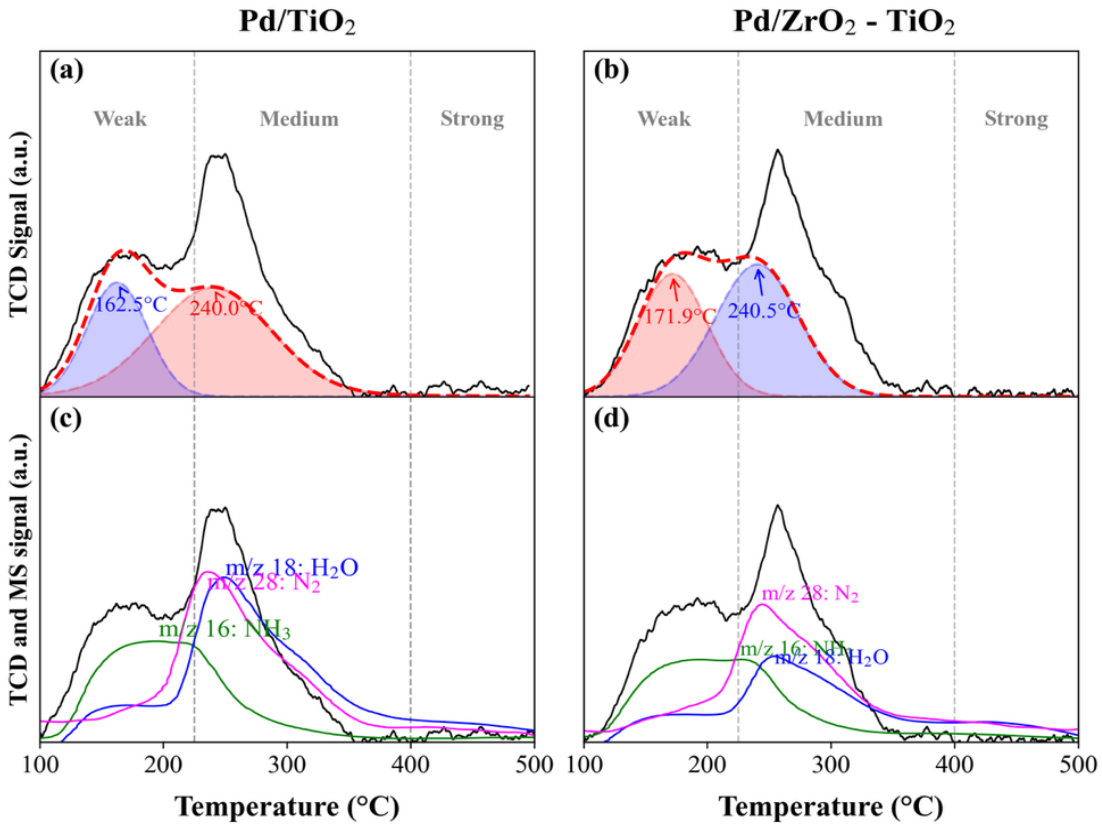

Figure A-3. 7. TPD – NH_3 results for Pd/TiO_2 (left column: (a) and (c)) and $Pd/ZrO_2–TiO_2$ (right column: (b) and (d)) catalysts. The first row shows the TCD signal as a function of temperature, while the second row combines the TCD signal with the mass spectrometric responses for NH_3, H_2O, and N_2. Vertical dashed lines indicate characteristic temperature regions corresponding to weak (T <200°C), medium and strong (T > 200°C) acid sites.

A-3.3. Pyrolysis of natural rubber without catalyst

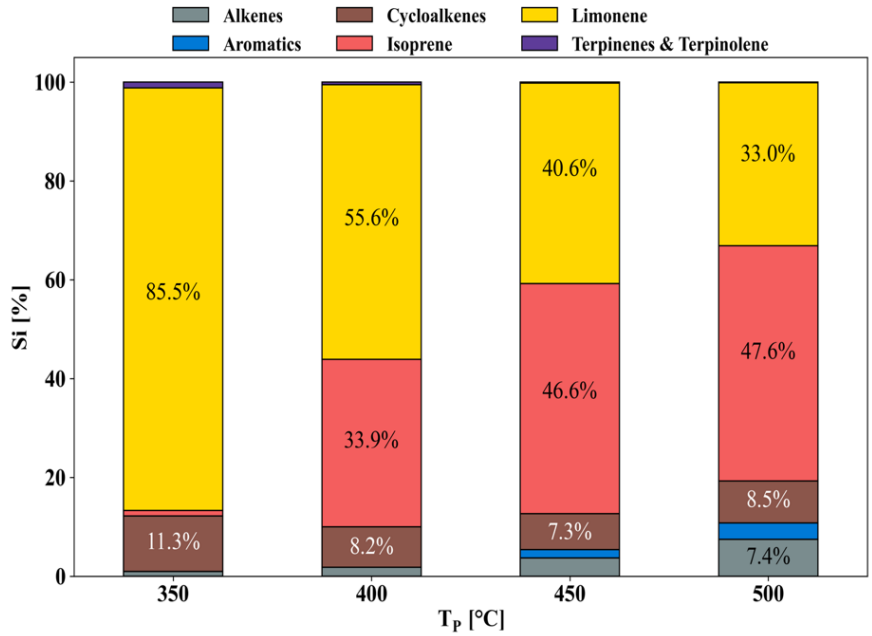

Figure A-3. 8. Distribution of vapor-phase products from the pyrolysis of NR at different temperatures (T_P). For these experiments, the temperature of the empty catalytic reactor (T_c) was kept at 300°C.

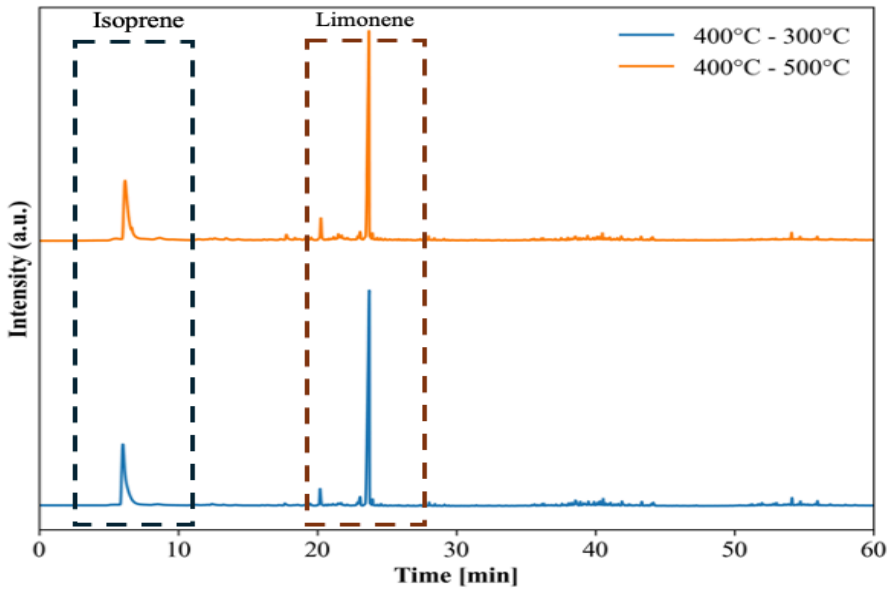

Figure A-3. 9. GC–MS chromatograms of pyrolysis vapors from NR at 400 °C, followed by a second inert reactor at 300 °C (blue) and 500 °C (orange).

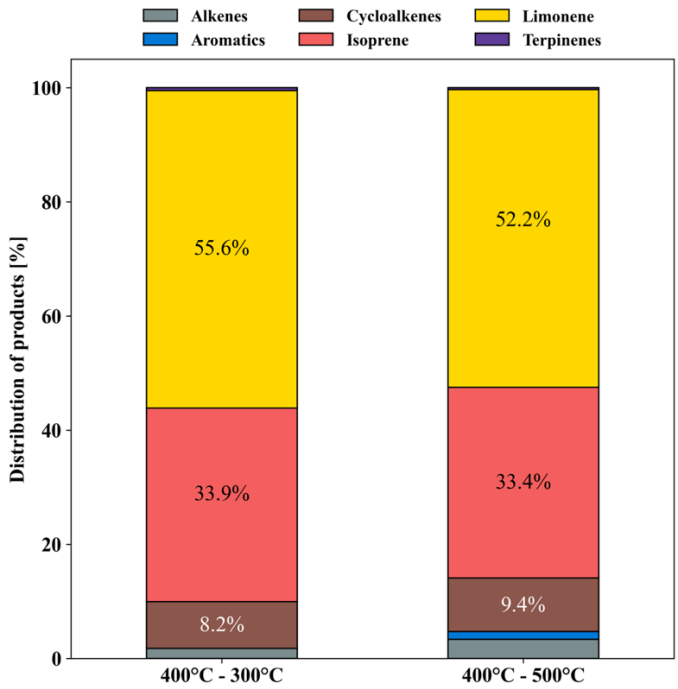

Figure A-3. 10. Distribution of products Distribution of vapor-phase products from the pyrolysis of natural rubber at TP = 400°C and temperature of the empty catalytic reactor (Tc) at 300°C and 500°C.

A-3.3. Catalytic pyrolysis

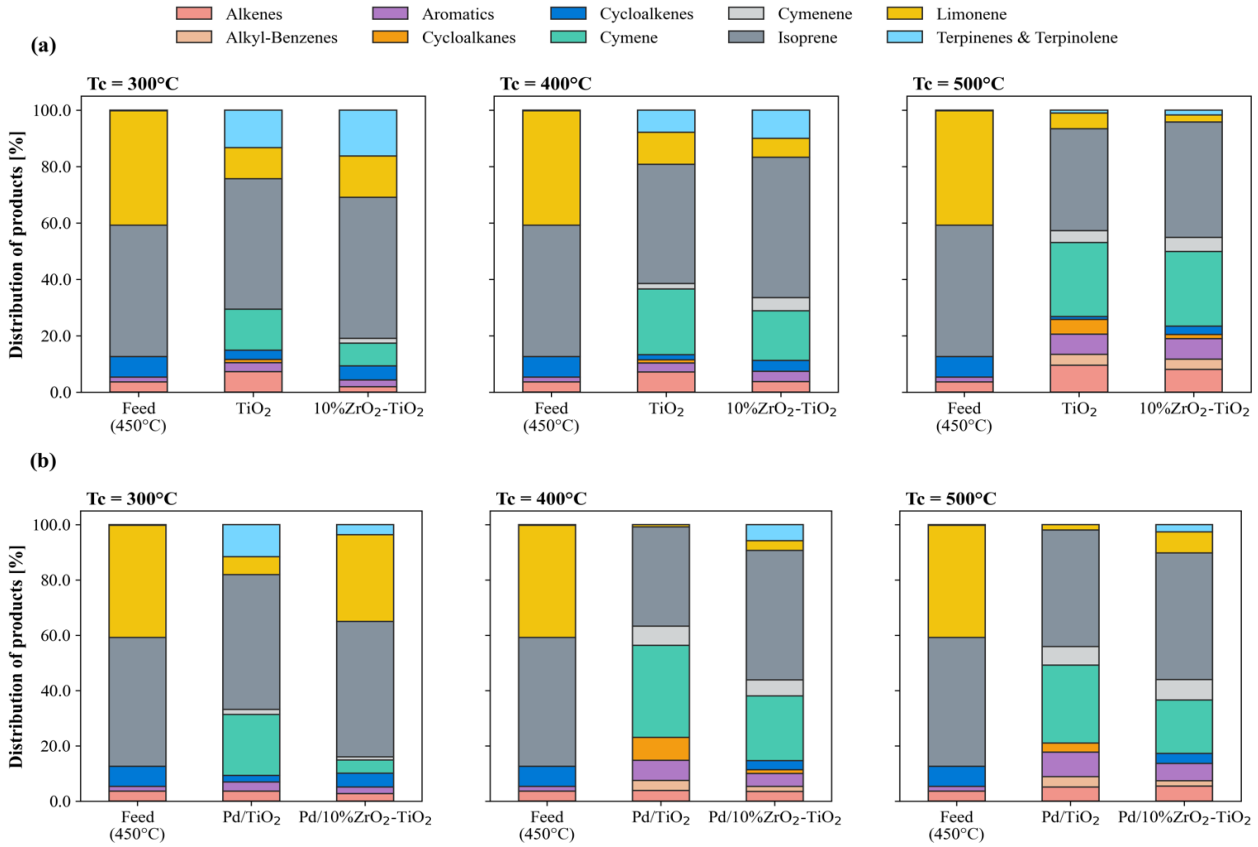

Figure A-3. 11. Vapor-phase products distribution from pyrolysis of Natural Rubber (T_p = 450°C) in tandem with a catalysts bed operated at 300, 400 and 500 ºC. (a) Effect of catalyst supports TiO_2 and ZrO_2-TiO_2. (b) Distribution of products for catalysts Pd/TiO_2 and Pd/10%ZrO_2-TiO_2 at different catalytic temperatures (T_C).

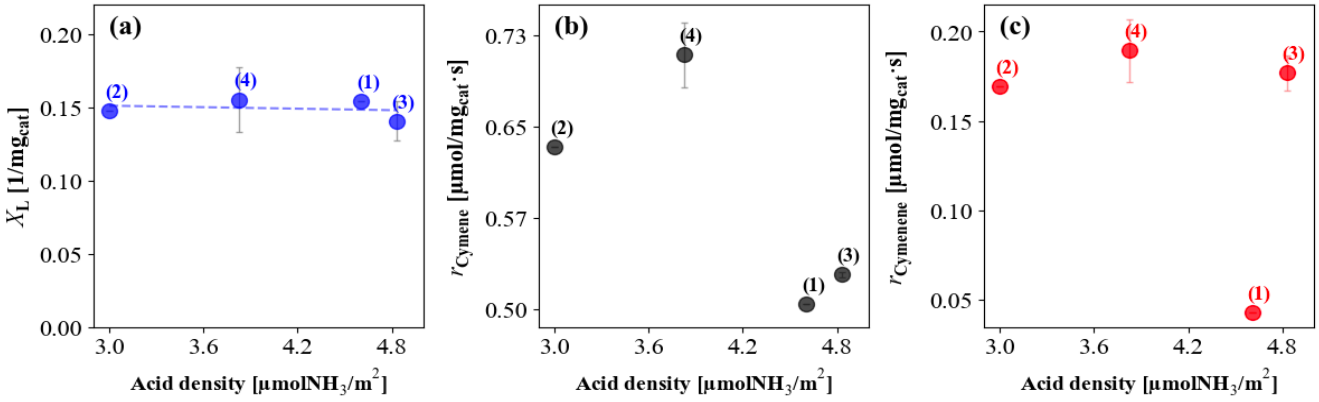

Figure A-3. 12. Effect of total acid site density on catalytic performance at 400 °C. (a) Limonene conversion normalized per gram of catalyst, (b) cymene formation rate, and (c) cymenene formation rate. Numbers indicate catalysts: (1) TiO_2, (2) ZrO_2–TiO_2, (3) Pd/TiO_2, and (4) Pd/ZrO_2–TiO_2. Error bars represent standard deviations from duplicate experiments.

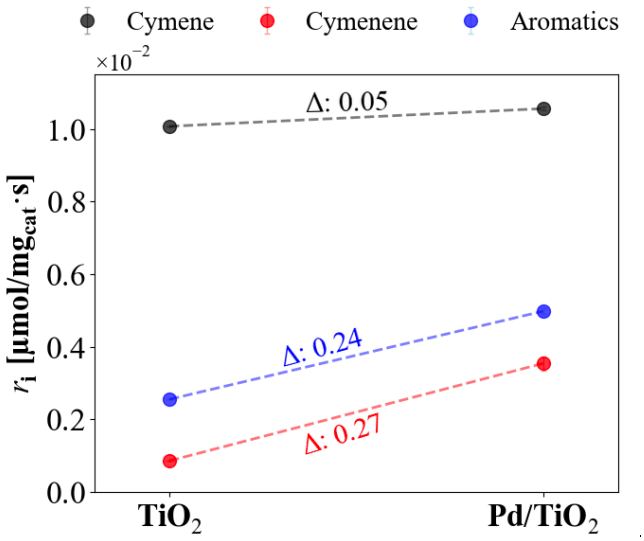

Figure A-3. 13. Reaction rates of cymene (black), cymenene (red), and aromatics (blue) over TiO_2 and Pd/TiO_2 catalysts on catalytic performance at 400°C.

A-3.3. Kinetic modeling

Table A-3. 2. The mechanism of reaction for alternative routes of limonene transformation. Route 2: direct dehydrogenation to p-cymenene. Route 3: side reactions leading to undesired by-products.

<table>
<tr><th colspan="4">Surface reaction pathways of pyrolytic limonene</th></tr>
<tr><th colspan="2">Route 2 – Direct dehydrogenation

$A \rightarrow C + 2H_2$</th><th colspan="2">Route 3 – Side reactions

$A \rightarrow 2I$
$A \rightarrow F$</th></tr>
<tr><th colspan="4">Mechanism of surface reactions</th></tr>
<tr><td rowspan="2">Dehydrogenation steps</td><td rowspan="2">$\mathbf{A^*} + (*) \overset{\mathbf{k_2}}{\rightarrow} \mathbf{CH_3^*} + \mathbf{H^*}$ (RDS)

$CH_3^* + (*) \rightarrow CH_2^* + H^*$

$CH_2^* + (*) \rightarrow CH^* + H^*$

$CH^* + (*) \rightarrow C^* + H^*$</td><td>Isoprene formation</td><td>$\mathbf{A^* + (*) \xrightarrow{k_{3,1}} I^* + I^*}$</td></tr>
<tr><td>Cycloalkenes formation</td><td>$\mathbf{A^* + (*) \xrightarrow{k_{3,2}} F^* + R_i^*}$</td></tr>
<tr><th colspan="4">Desorption of products</th></tr>
<tr><td>Cymenene

Hydrogen</td><td>$C^* \rightarrow C + (*)$

$2\,(\,2H^* \rightarrow H_2 + 2(*)\,)$</td><td>Isoprene

Cycloalkenes

Radicals</td><td>$2I^* \rightarrow 2I + 2(*)$

$F^* \rightarrow F + (*)$

$R_i^* \rightarrow R_i + (*)$</td></tr>
<tr><th colspan="4">Expression of rate reaction</th></tr>
<tr><td colspan="2">$r_2 = k_2 \cdot \theta_A \cdot \theta_*$</td><td colspan="2">$r_3 = k_3 \cdot \theta_A \cdot \theta_*$</td></tr>
</table>

Table A-3. 3. Temperature dependence of the ratio r_2/r_1 and the corresponding correction factor $\Phi(T)$ used in the kinetic analysis.

Temperature [°C]	r_2/r_1 [-]	$\Phi(T)$ [-]
300	0.294	1.294
400	0.275	1.275
500	0.578	1.578

Table A-3. 4. Summary of kinetic models tested. Dual-site and single-site Langmuir–Hinshelwood formulations were evaluated under different adsorption assumptions. The mean absolute percentage error (MAPE) at 300, 400, and 500 °C is reported together with the physicochemical consistency check.

RDS Route 3	**Model**	**Temperature [°C]**	**MAPE [%]**	**Physicochemical criterion**
Dual - site	**I** Only limonene adsorption	300	30.22	Checked
		400	10.32	
		500	10.31	
	II Limonene and by-products of pyrolysis adsorption	**300**	**10.28**	**Checked**
		400	**7.92**	
		500	**11.63**	
	III Limonene and Hydrogen adsorption	300	86.88	Checked
		400	4.29	
		500	20.83	
Single- site	**IV** Only limonene adsorption	300	29.56	Checked
		400	9.61	
		500	10.30	
	V Limonene and by-products of pyrolysis adsorption	300	10.37	X
		400	7.43	
		500	15.39	

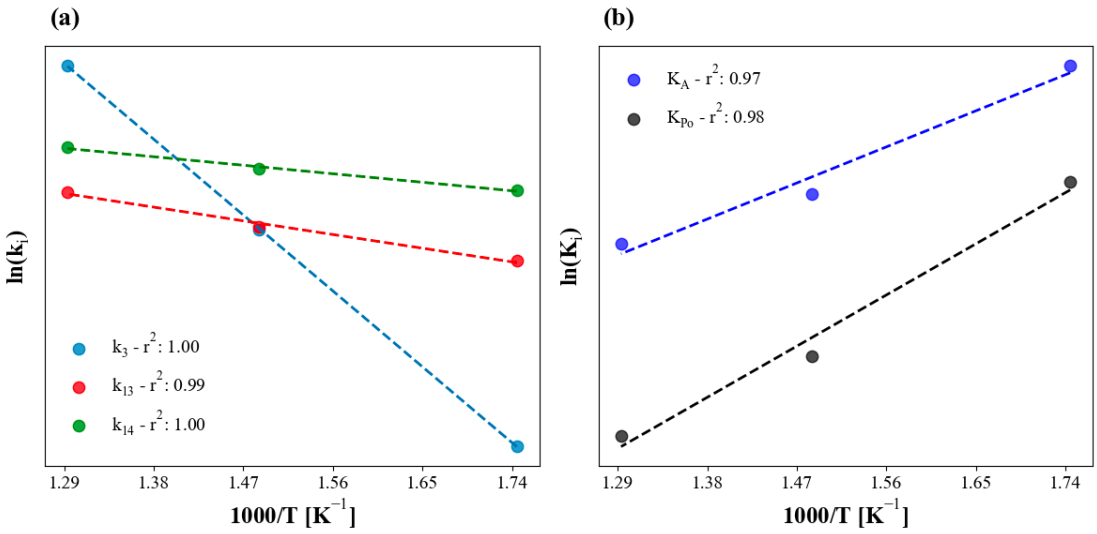

Figure A-3. 14. Arrhenius-type plots for the kinetic parameters used in the Langmuir–Hinshelwood model. (a) Temperature dependence of the rate constants for limonene isomerization (k_1), cymene formation (k_2), and cymenene formation (k_3). (b) Adsorption equilibrium constants for limonene (K_L) and pyrolysis by-products (K_{P_0}), showing opposite temperature dependence trends.

Derivation of system of differential equations for cymene (B) generation

If rate of consumption of limonene is:

$$(-r_A) = \frac{\Phi(T) \cdot \alpha \cdot F_A + \beta \cdot F_A}{\left(1 + K_A \cdot F_A + K_{P_0} \cdot F_{P_0}\right)^2}$$

where:

$\alpha = k_1 \cdot K_1 \cdot K_2 \cdot K_A$

$\beta = k_3 \cdot K_A$

$\Phi(T) = 1 + r_2/r_1$

The cymene (B) generation can be expressed:

$$r_B = r_{1,4} = k_{1,4} \cdot \theta_B$$

where θ_B can be expressed in function of limonene flow in vapor pyrolytic (F_A) assuming steady state approximation (SSA):

$$\frac{d\theta_B}{dt} = 0 = r_{1,1} - r_{1,3} - r_{1,4}$$

$$0 = r_{1,1} - k_{1,3} \cdot \theta_B \cdot \theta_* - k_{1,4} \cdot \theta_B$$

$$k_{1,3} \cdot \theta_B \cdot \theta_* + k_{1,4} \cdot \theta_B = r_{1,1}$$
$$\theta_B \cdot \left(k_{1,3} \cdot \theta_* + k_{1,4}\right) = r_{1,1}$$

$$\theta_B = \frac{r_{1,1}}{\left(k_{1,3} \cdot \theta_* + k_{1,4}\right)}$$

Substituting θ_B in r_B function:

$$r_B = k_{1,4} \cdot \frac{r_{1,1}}{\left(k_{1,3} \cdot \theta_* + k_{1,4}\right)}$$

Finally, substituting $r_{1,1} = r_1 = \alpha \cdot F_A \cdot \theta_*^2$:

$$r_B = k_{1,4} \cdot \frac{\alpha \cdot F_A \cdot \theta_*^2}{\left(k_{1,3} \cdot \theta_* + k_{1,4}\right)}$$

$$r_B = \frac{k_{1,4}}{\left(\frac{k_{1,3}}{\left(1 + K_A \cdot F_{A_0} \cdot (1 - X) + K_P \cdot F_{P_0}\right)} + k_{1,4}\right)} \cdot \frac{\alpha \cdot F_{A_0} \cdot (1 - X)}{\left(1 + K_A \cdot F_{A_0} \cdot (1 - X) + K_P \cdot F_{P_0}\right)^2}$$

Also, for cymenene (C), the rate generation is can expressed as:

$$r_C = r_2$$

where: $r_2 = r_1 \cdot (\Phi(T) - 1)$:

$$r_C = \alpha \cdot F_A \cdot \theta_*^2 \cdot (\Phi(T) - 1)$$

$$r_C = \frac{\alpha \cdot F_{A_0} \cdot (1 - \mathrm{X}) \cdot (\Phi(T) - 1)}{\left(1 + K_A \cdot F_{A_0} \cdot (1 - X) + K_P \cdot F_{P_0}\right)^2}$$

Moreover, for Hydrogen (H_2), the rate generation is can expressed as:

$$r_{H_2} = r_B + 2 \cdot r_C$$

$$r_{H_2} = \frac{k_{1,4}}{\left(\frac{k_{1,3}}{\left(1 + K_A \cdot F_{A_0} \cdot (1 - X) + K_P \cdot F_{P_0}\right)} + k_{1,4}\right)} \cdot \frac{\alpha \cdot F_{A_0} \cdot (1 - X)}{\left(1 + K_A \cdot F_{A_0} \cdot (1 - X) + K_P \cdot F_{P_0}\right)^2} + 2$$
$$\cdot \frac{\alpha \cdot F_{A_0} \cdot (1 - \mathrm{X}) \cdot (\Phi(T) - 1)}{\left(1 + K_A \cdot F_{A_0} \cdot (1 - X) + K_P \cdot F_{P_0}\right)^2}$$

The system of equations for limonene conversion, cymene (B), cymenene (C) and hydrogen (H_2) for PBR reactor:

$$\frac{dF_A}{dW} = r_A$$
$$\frac{dF_B}{dW} = r_B$$
$$\frac{dF_C}{dW} = r_C$$
$$\frac{dF_{H_2}}{dW} = r_{H2}$$

Considering than $F_A = F_{A_0} \cdot (1 - X)$, $dF_A = -F_{A_0} \cdot dX$:

$$\frac{dX}{dW} = \frac{\Phi(T) \cdot \alpha \cdot (1 - \mathrm{X}) + \beta \cdot (1 - \mathrm{X})}{\left(1 + K_A \cdot F_A + K_{P_0} \cdot F_{P_0}\right)^2}$$

Finally, expanding all equations:

$$\frac{dX}{dW} = \frac{\Phi(T) \cdot \alpha \cdot (1 - \mathrm{X}) + \beta \cdot (1 - \mathrm{X})}{\left(1 + K_A \cdot F_A + K_{P_0} \cdot F_{P_0}\right)^2}$$
$$\frac{dF_B}{dW} = \frac{k_{1,4}}{\left(\frac{k_{1,3}}{\left(1 + K_A \cdot F_{A_0} \cdot (1 - X) + K_P \cdot F_{P_0}\right)} + k_{1,4}\right)} \cdot \frac{\alpha \cdot F_{A_0} \cdot (1 - X)}{\left(1 + K_A \cdot F_{A_0} \cdot (1 - X) + K_P \cdot F_{P_0}\right)^2}$$

$$\frac{dF_C}{dW} = \frac{\alpha \cdot F_{A_0} \cdot (1 - \mathrm{X}) \cdot (\Phi(T) - 1)}{\left(1 + K_A \cdot F_{A_0} \cdot (1 - X) + K_P \cdot F_{P_0}\right)^2}$$

$$\frac{dF_{H_2}}{dW} = \frac{k_{1,4}}{\left(\frac{k_{1,3}}{\left(1 + K_A \cdot F_{A_0} \cdot (1 - X) + K_P \cdot F_{P_0}\right)} + k_{1,4}\right)} \cdot \frac{\alpha \cdot F_{A_0} \cdot (1 - X)}{\left(1 + K_A \cdot F_{A_0} \cdot (1 - X) + K_P \cdot F_{P_0}\right)^2} + 2$$
$$\cdot \frac{\alpha \cdot F_{A_0} \cdot (1 - \mathrm{X}) \cdot (\Phi(T) - 1)}{\left(1 + K_A \cdot F_{A_0} \cdot (1 - X) + K_P \cdot F_{P_0}\right)^2}$$